Modeling and simulation of the motion of deformable interfaces in a confined geometry : application to the study of the flow of red blood cells in microcirculation

Othmane Aouane

To cite this version:

Othmane Aouane. Modeling and simulation of the motion of deformable interfaces in a confined geometry : application to the study of the flow of red blood cells in microcirculation. Biological Physics [physics.bio-ph]. Université Grenoble Alpes; Universität des Saarlandes, 2015. English. NNT : 2015GREAY096 . tel-01686225

HAL Id: tel-01686225
https://theses.hal.science/tel-01686225

Submitted on 17 Jan 2018

HAL is a multi-disciplinary open access archive for the deposit and dissemination of scientific research documents, whether they are published or not. The documents may come from teaching and research institutions in France or abroad, or from public or private research centers.

L'archive ouverte pluridisciplinaire **HAL**, est destinée au dépôt et à la diffusion de documents scientifiques de niveau recherche, publiés ou non, émanant des établissements d'enseignement et de recherche français ou étrangers, des laboratoires publics ou privés.

UNIVERSITÄT DES SAARLANDES

UNIVERSITÉ GRENOBLE ALPES

THÈSE

Pour obtenir le grade de

DOCTEUR DE L'UNIVERSITÉ GRENOBLE ALPES

préparée dans le cadre d'une cotutelle entre l'*Université Grenoble Alpes* et *Universität* des *Saarlandes*

Spécialité : **Physique pour les sciences du vivant**

Arrêté ministériel : le 6 janvier 2005 - 7 août 2006

Présentée par

Othmane Aouane

Thèse dirigée par **Chaouqi Misbah** et **Christian Wagner**

préparée au sein des **Laboratoires : Interdisciplinaire de Physique (LIPhy) à Grenoble et Experimentalphysik (AG Wagner) à Saarbrücken**

dans **les Écoles Doctorales de : Physique à Grenoble et Naturwissenschaftlich-Technische Fakultät II -Physik und Mechatronik- à Saarbrücken**

Modélisation et simulation du mouvement d'intérfaces déformables dans une géométrie confinée

Thèse soutenue publiquement le **18 Septembre 2015**,
devant le jury composé de :

M. Rolf Pelster
Professeur, Universität des Saarlandes, Président
M. Chaouqi Misbah
Directeur de recherche CNRS, Université Grenoble Alpes, Directeur de thèse
M. Christian Wagner
Professeur, Universität des Saarlandes, Directeur de thèse
M. Takuji Ishikawa
Professeur, Tohoku University, Rapporteur
M. Marc Léonetti
Chargé de Recherche CNRS, IRPHE, Rapporteur
M. Philippe Peyla
Professeur, Université Grenoble Alpes, Examinateur
Mme. Tanja Schilling
Professeur, Université du Luxembourg, Examinateur
M. Abdelillah Benyoussef
Professeur, Université Mohammed V-Agdal, Invité
M. Andreas Tschöppe
Chercheur, Universität des Saarlandes, Invité

Modeling and simulation of the motion of deformable interfaces in a confined geometry: application to the study of the flow of red blood cells in microcirculation

Dissertation
im Rahmen eines Cotutelle-Verfahrens zur Erlangung des
Grades des Doktors der Naturwissenschaften
der Naturwissenschaftlich-Technischen Fakultät II
-Physik und Mechatronik-
der Universität des Saarlandes
und des Docteur de l'Université de Grenoble-Alpes

Thèse
dans le cadre d'une cotutelle pour obtenir le grade de
Docteur de l'Université de Grenoble-Alpes
Spécialité: Physique pour les sciences du vivant
et de Doktor der Naturwissenschaften der Universität des
Saarlandes

von/presentée par
Othmane AOUANE

Saarbrücken
2015

Diese Arbeit wurde von der Deutsch-Französischen Hochschule (DFH) finanziell gefördert.

Cette thèse était subventionnée par l'Université franco-allemende (UFA).

Tag des Kolloquiums: 18.09.2015

Eidesstattliche Versicherung

Hiermit versichere ich an Eides statt, dass ich die vorliegende Arbeit selbstständig und ohne Benutzung anderer als der angegebenen Hilfsmittel angefertigt habe. Die aus anderen Quellen oder indirekt übernommenen Daten und Konzepte sind unter Angabe der Quelle gekennzeichnet. Die Arbeit wurde bisher weder im In- noch im Ausland in gleicher oder ähnlicher Form in einem Verfahren zur Erlangung eines akademischen Grades vorgelegt.

Par la présente, je certifie que j'ai rédigé cette thèse indépendemment et seulement avec les sources mentionnées. Ces travaux de thèse n'ont jamais été utilisés sous une forme identique ou similaire, dans ce pays ou dans un pays étranger, pour l'obtention d'un diplôme universitaire.

Saarbrücken, 06.05.2015

Othmane AOUANE

It is only natural, of course, that each man should think his own opinions best: the crow loves his fledgling, and the ape his cub.

– Thomas More, Utopia.

Chacun se complait à ses propres idées, c'est la nature qui en a ainsi décidé. Le corbeau trouve ses petits charmants et la vie du jeune singe enchante ses parents.

– Thomas More, Utopia.

Und in der That ist es nur natürlich, daß die Menschen in die Einfälle ihres eigenen Geistes verliebt sind. Den Raben und den Affen dünken ihre Jungen auch die schönsten Geschöpfe.

– Thomas Morus, Utopia.

Modeling and simulation of the motion of deformable interfaces in a confined geometry: application to the study of the flow of red blood cells in microcirculation

Abstract: Vesicles are extensively used as a model for understanding dynamics and deformation of red blood cells at the individual level but also regarding collective phenomena and rheology. Vesicles' membranes withstand to bending but do not have a shear resistance, unlike red blood cells, but they still share several dynamical properties with red blood cells, like tank-treading and tumbling under linear shear flow, or parachute and slipper shapes under Poiseuille flow. The red blood cells are known to form train of cells in the microcirculation attributed to attractive hydrodynamic interactions. We investigate numerically several kind of problems such as: (i) the dynamics of isolated cells; (ii) the hydrodynamic coupling between the red blood cells (by using vesicles as a model) subject to a Poiseuille flow under different confinements; (iii) the aggregation of red blood cells and formation of rouleaux; and (iv) the contribution of macromolecules in the formation of clusters under flow condition. The obtained results give a new insight into the physics of deformable objects under confinement that are transposable to the flow of red blood cells in the microcirculation.

Keywords: Vesicles, red blood cells, boundary integral method, poiseuille flow, chaotic dynamics, aggregation, cluster formation, hydrodynamic interactions, basin of attraction, macromolecules-induced interactions.

Modeling and simulation of the motion of deformable interfaces in a confined geometry: application to the study of the flow of red blood cells in microcirculation

Abstract: Les vésicules sont utilisées d'une manière extensive comme modèle pour comprendre les dynamiques et les déformations des globules rouges au niveau individuel, mais aussi concernant les phénomènes collectives et la rhéologie. La membrane de la vésicule résiste à la flexion mais pas au cisaillement, contrairement aux globules rouges, néanmoins elles partagent plusieurs propriétés dynamiques avec les globules rouges, comme le tank-treading (mouvement en chenille de char) et le tumbling (mouvement de bascule) sous écoulement de cisaillement, ou les formes parachutes et slippers (pantoufles) sous un écoulement de Poiseuille. Les globules rouges sont connus pour former des trains de cellules (clusters) dans la microcirculation attribués à la nature attractive des interactions hydrodynamiques. Nous avons étudié numériquement plusieurs types de problème comme:(i) les dynamiques de cellules isolées, (ii) le couplage hydrodynamique entre globules rouges (en utilisant les vésicules comme modèle) soumis à un écoulement de Poiseuille sous différent confinements; (iii) l'agrégation des globules rouges et la formation de rouleaux; et (iv) le rôle des macromolecules dans la formation de clusters sous écoulement. les résultats obtenus apportent un nouveau regard à la physique des objets déformables et sont transposables au cas de l'écoulement des globules rouges dans la microcirculation.

Mots-clefs: Vésicules, globules rouges, méthode des intégrales de frontières, écoulement de poiseuille, chaos, agrégation, formation de cluster, interactions hydrodynamiques, bassin d'attraction, interactions dûe aux macromolécules.

Modeling and simulation of the motion of deformable interfaces in a confined geometry: application to the study of the flow of red blood cells in microcirculation

Kurzzusammenfassung: Vesikel werden in der aktuellen Forschung extensiv als Modelsystem genutzt um die Dynamik und die Deformation von roten Blutzellen (RBCs) zu verstehen. Dies sowohl auf dem individuellen Level wie auch für kollektive Phänomene und die Rheologie. Die Membran von Vesikel ist nicht dehnbar jedoch verformbar und eine Scherung erfolgt widerstandslos. Rote Blutzellen haben vergleichbare Eigenschaften, auch wenn eine Scherung nicht widerstandslos erfolgt. So wird unter einem linearen Scherfluss das tank-treading (vergleichbar mit der Bewegung einer Panzerkette) oder eine Taumelbewegung beobachtet. Im Poiseuille-Fluss werden hingegen parachute (fallschirmförmig) oder slipper (schuhförmig) Konfigurationen angenommen. Es ist bekannt, dass rote Blutzellen in der Mikrozirkulation zu Aneinanderreihungen neigen. Dies geschieht aufgrund der anziehenden hydrodynamischen Wechselwirkung. Es wurden verschiedene Problemstellungen untersucht: (i) die Dynamik einzelner Zellen, (ii) die hydrodynamische Kopplung zwischen roten Blutzellen (als Vesikel im Modellsystem) in einem Poiseuille-Fluss bei verschiedenen geometrischen Einschränkungen, (iii) die Aggregation und die Bildung von Rollen bei roten Blutzellen und (iv) der Beitrag von Makromolekülen an der Clusterbildung unter Flussbedingungen. Die dargestellten Untersuchungen geben neuartige Einblicke in die Physik von verformbaren Objekten in eingeschränkten Geometrien welche bedeutend sind für das Verständnis der Bewegung von roten Blutzellen in der Mikrozirkulation.
Schlüsselwörter: Vesikel, rote Blutzellen, Randintegralmethode, Poiseuille-Fluss, chaotische Dynamik, Aggregation, Clusterbildung, hydrodynamische Wechselwirkung, Hauptattraktor, durch Makromoleküle hervorgerufene Wechselwirkungen.

Acknowledgements

This work was supervised by Dr. Chaouqi Misbah from Laboratoire Interdisciplinaire de Physique (LIPhy), and Prof. Dr. Christian Wagner from Universität des Saarlandes, and supported by the German Graduate School (GRK 1276), German Research Fundation (SFB 1027), and the German-French University (DFH/UFA).

Mes remerciements vont tout d'abord à mes deux directeurs de thèse pour leurs conseils avisés et leur soutien durant toute la durée de cette thèse. Merci d'avoir consacrer du temps à écouter et guider le jeune bioinformaticien/physicien que j'étais vers un domaine où mathématique, physique et biologie se complémentent (du moins en théorie) pour tenter de percer les mystères de la vie à l'échelle microscopique.
C'est grâce à Chaouqi Misbah et au Prof. Abdelillah Benyoussef de la faculté des Sciences de Rabat que j'ai fini par découvrir la biophysique et plus particulièrement la modélisation et simulation des vésicules pendant mon stage de Master 2 à Grenoble. Ceci m'a permis par la suite de rencontrer Christian Wagner et d'avoir la chance d'être entouré par une équipe d'expérimentateurs à Saarbrücken. Ce fût un environement très stimulant et enrichissant qui m'a conduit vers une meilleure compréhension des problématiques à modéliser.

Mes remerciements vont également à Monsieur Rolf Pelster qui m'a fait l'honneur de présider le Jury, à Madame Tanja Schilling et Messieurs Andreas Tschöpe, Philippe Peyla, Abdelillah Benyoussef, Marc Léonetti, Christian Wagner et Chaouqi Misbah pour leur participation au Jury et la discussion stimulante qui a fait suite à la soutenance. J'adresse toute ma gratitude aux rapporteurs Messieurs Takuji Ishikawa, Marc Léonetti et Christian Wagner qui à travers leurs remarques et suggestions ont participé à améliorer la qualité de ce travail qui à mes yeux et sous sa version actuelle reste encore inachevé (faute de temps).

Je remercie énormément mes collègues théoriciens et amis du LIPhy: Alexander Farutin, Giovanni Ghigliotti, Hassib Selmi et Marine Thiébaud pour leurs contributions et conseils tout au long de cette thèse.

Je remercie particulièrement Karin Kretsch, Elke Huschens, Viviana Clavería, Jorge Fiscina, Zakaria Boujja, Thomas John, et Philippe Bohr pour leur aide dans l'organisation de la soutenance.

Un grand merci à Andreas Christ et Emmanuel Terriac pour leurs suggéstions, conseils et encouragements avant la soutenance.

Je remercie beaucoup Lionel Bureau –mon tuteur de thèse –pour sa disponibilité, son soutien et ses conseils durant les moments difficiles de la thèse.

Je remercie tous mes autres collègues et amis du LIPhy (Luca L., Sofia, Matthieu, Vassenti, Johannes, Davide, Nathalia, Thomas S., Brenna, Vincent, Luca M., Elisabeth, Alexandre N., Hao, Zaiyi, Chen, Thomas P., Gwennou, Claude, Salima, Mourad, Philippe P., Alexander F., Marine, ...), et ceux d'AG-Wagner (Daiki, Matthias, Viviana, Daniel, Javad, Levke, Sebastian, Jorge, Philippe, Andreas G., Christian R., Thomas J. et Andreas C.), d'AG-Kruse (Denis et Dominic) et AG-Lautenschläger (Manu, Luisa et Franziscka) pour les bons moments passés ensembles au et en dehors du travail.

Merci à tous mes amis des quatres coins du monde (Daiki, Matthieu, Luca, Vivania, Daniel, Matthias, Andreas, Manu, Christian, Alejandro, Karen, Darya, Uma, Isabella, Anastasia, Yarouslava, Azzedine, Ashyrmyrat, Yazguli, Gonzalo, Preeti, Siddhartha, Alessandra, Alexander, Kapil, Lumineta, ...) rencontrés un peu par hasard entre Grenoble et Saarbrücken et qui m'ont fait découvrir un avant-goût des richesses que recèle ce vaste monde.

Merci à Jessie Sitbon et Elke Huschens pour leur bonne humeur, disponibilité et leur extraordinaire capacité à simplifier les tâches administratives.

Et pour finir, je remercie du fond du coeur toute ma famille pour son indéfectible soutien moral.

Je dédie cette thèse à la mémoire de ma grand-mère Menana.

Contents

CHAPTER 1

General Introduction

Contents

1.1 Scope of the Thesis

It is known since long that understanding the underlying mechanisms of red blood cells aggregation and blood flow may be a keystone explaining the etiology of certain pathological situations. Some of these diseases are closely related to the functioning of red blood cells. It is important to recall the main function of red cells, oxygen transport from the lungs to the rest of the body. Organs like the heart, the kidney and the brain have a high demand on oxygen. Oxygen is released by the red cells in the microcirculation, and more precisely in small and tiny vessels called the capillaries. The capillaries often have a diameter smaller than the one of the red blood cells themselves. Therefor the red blood cells are subject to severe deformations during their flow in these small vessels. In the microcirculation, it is often observed that the red cells flow in single or multiple files forming small trains of cells called clusters. The arrangement and organization of the red cells depend on the diameter of the vessel and the concentration of red cells (hematocrit). Each red blood cell interacts hydrodynamically with the other cells, and when the cells are in a close range from one another depletion and/or bridging interactions take place between the surrounding plasma proteins and the red cells leading to more persistent clusters. At physiological levels of the different plasma proteins, and for healthy red cells, clustering is a reversible process. However that might lead to a partial or total occlusion of the small vessels (ischemia). The tissues deprivation from oxygen might induce a severe pain (due to the lack of oxygen) and may lead to irreversible damages in these regions. When it occurs in the brain, it might cause a stroke (cerebrovascular accident), whereas in the heart, it might lead to congestive heart failures as a consequence of an overpressure due to the augmentation of blood volume and an incapacity to pump it through the obstructed (or narrowed in case of partial occlusions) capillaries. Surprisingly, the physics of the microcirculation is still unclear. This might be explained by the complexity of the interaction between different sciences leading to the understanding of the necessary minimal ingredients to build a starting model that can be used to describe the non-trivial coupling between the red cells and the geometry of the vessels from one side, and the interaction with the plasma proteins from the other side. In order to distinguish the contribution of the hydrodynamic and depletion-bridging interactions on the formation of clusters, we have investigated in this thesis problems related to: i)- aggregation in a static fluid due to depletion-bridging, ii)- flow of single cells, iii)- hydrodynamic interactions between a pair of cells and effect of the confinement, iv)- role of the depletion-bridging interactions on the formation of clusters of red cells in microcirculation. Although the main focus of this thesis is to investigate the flow of cells in the microcirculation, many relevant physical questions to the understanding of dynamics of flowing soft objects in a confined geometry will be tackled during the different chapters.

1.2 Generalities about Blood and its components

During the blood flow in the circulatory system, the oxygenated blood is pumped from the heart into the arteries, which are tubes with a large diameters. It goes then into smaller vessels, the arterioles, before entering into the capillary bed, where oxygen and nutrients are delivered to tissues and carbon dioxide and wastes are expulsed from tissues to the blood. The deoxygenated blood is carried then into small venules; and then into larger vessels; the veins, back toward the heart. This is an extremely complex and vital process in which, every parameter must be regulated and adjusted carefully in order to deliver, in the way that fit the different conditions, the blood in the different parts of the body. One can imagine what may happen if the flow velocity of the blood in capillaries was comparable to the one in the large-diameter vessels such as arteries and veins. In this case, the diffusion of nutrients and oxygen to the tissues, the expulsion of wastes, and the heat regulation process will not take place properly due to the lack of time. The evolution finds a way to overcome this problem, by dividing the smallest vessels (the capillaries) where the diffusion process occurs in a dense network of slender capillaries (called capillary bed). By dividing up the blood flow, the same volume of blood coming from the large vessels can be handled by the capillary bed, but at slower velocity; slow enough to allow the exchange of nutrients and wastes and fast enough to avoid any kind of blood sludging. In analogy to a parallel electrical circuit, this disposition of the capillaries assures the blood circulation even if one capillary or more is occluded for specific reasons.

Recall that blood is formed by 45% of cells distributed as follow: 98% of these are red blood cells, 1% are a mixture of platelets and white blood cells. These

Figure 1.1: Left: Blood components after centrifugation. Right: Micrograph depicting human blood cells. Red blood cells (in red), 3 T-cells (in orange), and activated platelets (in green). The T-cells are one of the four types of lymphocytes (natural killer cells, B-cells, T-cells, and suppressor T-cells). In their turn, the lymphocytes are one of the three types of white cells (granulocytes, lymphocytes, and monocytes). Courtesy of "http://visualsunlimited.photoshelter.com ".

cellular components are suspended in the plasma, the liquid counterpart of the blood which is mainly made up of water (93%). One can be tempted to describe the behavior of blood (rheological properties) by focusing on the flow of red blood cells in water. This in fact can be the minimum ingredients needed to build a toy model. Under these conditions, we end up with a system of deformable objects driven by an external flow in microchannels, and interacting hydrodynamically. We will focus then on describing the plasma and the red blood cells in the following subsections, and give a small overview on platelets and white cells.

1.2.1 Sloppy definition of red blood cells aggregation

In the healthy adult human, the red cells have a tendency to aggregate and form, under certain conditions, large aggregates called rouleaux. This phenomenon is a consequence of the presence of certain macromolecules in the plasma such as fibrinogen (a plasma protein known to induce aggregation). According to the literature, the aggregates are supposed to disaggregate under the effect of shear forces. Currently two models are widely used to explain the mechanism behind RBCs aggregation: bridging and depletion. In the bridging model, the macromolecules are believed to adsorb on to the surface of the RBC and make bonds with a close enough RBC in a range relative to the macromolecule length. The depletion model states that the exclusion of macromolecules from the depleted area between the adjacent cells will lead to an osmotic gradient and therefor to a depletion interaction. In both cases the formation of aggregates happens only if the disaggregation forces are lower than the aggregation forces. RBCs aggregation is a reversible process, and should not be confused with clotting. Clotting occurs during a normal blood coagulation, where the fibrinogen is converted to insoluble strands called fibrin as a result of a complex cascade of chemical reactions. Platelets and cross-linked fibrin strands form a blood clot (thrombus) and cover the damaged blood vessel wall, stopping by the same occasion the bleeding and making possible the beginning of repair of the injured vessel.

1.2.2 Blood plasma: composition and role on aggregation of red blood cells

The plasma is considered to be a Newtonian fluid, even though it was proven recently by experiments [Brust 2013b] that plasma presents a non-Newtonian behavior. Indeed, they have reported that the flow resistance of the plasma is more pronounced than that of water. Therefor, viscoelastic properties of the plasma should not be ignored in future models aiming the study of blood flow. The plasma contains a number of solutes: different proteins that form 7% by weight, ions (*e.g.* Na^+, K^+, Cl^-, and $HCO_3{}^-$) and metabolites (*e.g.* carbohydrates, urea, amino acids, hormones, vitamins, fats) representing 1-2% of the plasma weight. These macromolecules are suspended in a water solution. We can classify the proteins by their role on the aggregation of the red blood cells. The first protein of interest is the fibrinogen. It forms 7% of the total amount of plasma proteins, has a molecular weight of 340 kDa, a fully extended length of about 475 Å, and is charged negatively. Its role as an agent inducing aggregation of red blood cells is well known and accepted in the community. However the role of other proteins is questionable. An example is the immunoglobulin G (IgG) which forms 22% of the total plasma protein, has a molecular weight of 150 kDa and a maximum length in a fully extended state of about 200 Å. Among studies supporting the positive role of IgG on aggregation we cite [Maeda 1986b], whereas other studies such as [Madl 1993] reported no effect at all on aggregation. In fact it was not possible to get more than the abstract of Ref.[Madl 1993], thus the protocol used by these authors remains unknown. Although these results were also reported in [Baskurt 2011, p. 12]. Indeed the preparation process and the protocols may change the effect on aggregation as highlighted in [Maeda 1986a]. A second important plasma protein is the albumin which is often used to avoid adhesion of red cells to the walls. It is a relatively small macromolecule in comparison to fibrinogen or to IgG. It has a molecular weight of 66 kDa, constitutes 55% of the plasma total proteins, and is the most negatively charged one[Maeda 1986b]. Its fully extended length is about 150 Å. The role of albumin in the presence of either IgG or fibrinogen has been studied in [Maeda 1986b]. The authors have reported that albumin inhibits the IgG-induced red cells aggregation, whereas it enhances the fibrinogen-induced red cells aggregation. Moreover, albumin alone can not induce aggregation of red cells. To elucidate these non-trivial interactions, the authors have added poly(glutamic acid) (PG) of 20 kDa. In the IgG + albumin solution, the addition of PG20 drastically inhibited the IgG-induced aggregation. Recall that PG20 alone (like the albumin) does not induce any aggregation of red cells, whereas for the fibrinogen + albumin solution, no effect has been observed on the aggregation. The authors have discussed the probable difference in the mechanism of interaction in the presence of albumin of IgG and fibrinogen with the surface of the red cell. This underlines the probable role of the specific and non-specific bending of the different macromolecules on the surface of the red cells, the affinity (strength of the chemical bonds), competition on the same bending sites that may ensue if two or more macromolecules share the same bending sites, their concentrations, their charge and eventually its strength, their length and shape, and so on. The non-trivial and unclear origin of these interactions increases drastically the level of complexity of our problem, and in the meanwhile explains the discrepancy that can be found in the literature of red blood cells aggregation. Besides, the level of these plasma proteins is not constant and may vary in case of a pregnancy or under the effect of some diseases. The normal level of fibrinogen in the plasma ranges between $1.8 - 4$ mg/mL [Comeglio 1996, Baskurt 2011]. Recall that fibrinogen is synthesized mainly in the liver[1] and is a precursor of fibrin, a protein that plays an important role in blood clotting. An increase of the level of fibrinogen was observed on patients after stroke[2], after myocardial infraction[3] [Ernst 1993, Di Napoli 2001], and for diabetics [Kannel 1990, Lee 1993]. It is known that the level of fibrinogen enhances the aggregation of RBCs, leading to bigger and stronger rouleaux. The interaction energy between the cells in a rouleaux increase linearly with the concentration of fibrinogen [Brust 2014], leading to rouleaux that can not be easily broke up when entering to the microcirculation. This situation might cause a partial or a complete occlusion of small vessels (ischemia). Aggregation of red cells is not reduced to the interplay between plasma proteins and the surface of red cells. The other factors will be discussed in the appropriate sections, and a general overview of the mechanism of rouleaux formation will be discussed in an other chapter.

1.2.3 Red blood cells: discovery and properties

1.2.3.1 Historical background

The story of the red blood cells (RBCs) began in the middle of the 17th century in Amsterdam, when Jan Swammerdam, a Dutch biologist and microscopist, was the first to observe and describe a human RBC in 1658. Few years later, he renounced to his work and devoted his life to spiritual matter under the influence of the French-Flemish mystic, Antoinette Bourignon de la Porte. He died few years later of Malaria, a disease resulting from the infection of the red blood cells by parasites belonging to the genus Plasmodium. After his death, his observations

---

[1] At this level I ignore completely how the level of fibrinogen is regulated in the body.

[2] Brain attack, resulting from a permanently or momentarily decrease of the cerebral blood flow leading to a brain ischemia (insufficient delivery of oxygen and glucose to the brain).

[3] Deficiency of oxygen supply to the myocardium due to a complete blockage or a partial decrease of blood flow in coronary arteries.

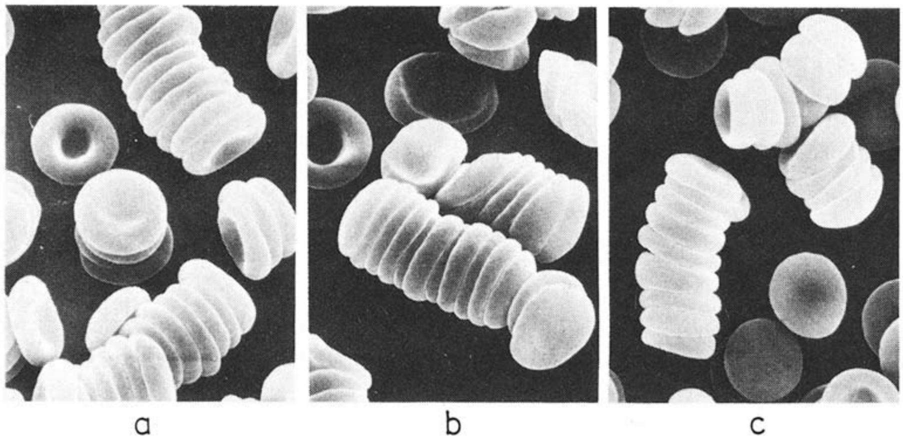

Figure 1.2: Formation and morphology of aggregates (rouleaux) of red blood cells in different solutions (with the same pH 7.4). a) 70% of autologous plasma and 30% of isotonic phosphate-buffered solution (PBS); b) Dextran 70 in PBS + 0.5 g/dL albumin; c) poly(glutamic acid) 50 in PBS + 0.5 g/dL albumin. Courtesy of [Maeda 1985].

were publicly disseminated. His work was partially resumed by Antonie Philips van Leeuwenhoek, another talented Dutch microscopist, who started his career as a draper in Delft, before opening his own shop in 1654, four years before the first observation of the red cell by Swammerdam. He then started to develop a real interest in lens-making and microscopy. He used his improved handcrafted microscopes to record observations on microorganisms like spermatozoa, bacteria, and single-celled organisms. He did a detailed description of the features of human RBCs in 1675. He had a regular correspondence with the English Royal Society, sharing his discoveries and detailed observations. He received the visit of different European Kings and Queens of that times amused and fascinated by his discoveries and observations, citing among others the Queen Catherine of England (the wife of the King Charles II) as depicted in Fig. 1.3. The Royal Society published later his remarkable work that covered a large aspect of microscopic phenomena. Nowadays, van Leeuwenhoek is considered as the father of the microscopy although he was not the discoverer of the microscope [4], and the father of the microbiology. The platelets and white cells were discovered around two centuries after the RBCs. Alfred Donné (1801-1878) a French public health physician discovered the platelets in 1842. The discovery of white cells was reported simultaneously in 1843 by Gabriel Andral (1797-1876) a French professor of medicine, and William Addison (1802-1881) an English country practitioner.

---

[4] The microscope was invented earlier in Holland around 1590 by Zacharias Jannsen (the name of the first inventor is still subject to controversy).

Figure 1.3: van Leeuwenhoek, considered as the father of microscopy and the discoverer of human red blood cells, exhibiting his microscopes to Queen Catherine of England. Courtesy from [Surgenor 1974]. Original painting by Pierre Brissaud.

1.2.3.2 Physical properties

RBCs adopt a biconcave shape when they are not subject to external stresses. Their diameters range between $6 - 8$ µm. With a lifespan of about 120 days, RBCs travel the equivalent of a distance of 400 km (roughly the distance between Paris and Saarbrücken), and pass through the heart 170000 times. During this time, the RBCs must carry the oxygen to the living tissues and take away the carbon dioxide. The gas exchange occurs in the capillaries, small vessels with a mean diameter of 7 µm, where the RBCs have to deform and squeeze into to guarantee the oxygenation of the body and therefor the life of the different cells and tissues (see Fig. 1.5). The brain requires around $15 - 20$ % of the oxygen in the blood to perform its usual tasks. Moreover, the reactions occurring during the gas exchanges between the tissues and the red blood cells play a key role in the regulation of the pH of the blood. The equation behind the carbon dioxide transport reads as

$$H_2O + CO_2 \xrightleftharpoons[\text{lungs}]{\text{tissues}} \underset{\text{Carbonic acid}}{H_2CO_3} \xrightleftharpoons[\text{lungs}]{\text{tissues}} H^+ + {HCO_3}^-$$

This reaction takes place not only inside the RBCs but also in the plasma. 7% of the carbon dioxide will be dissolved in the plasma, whereas 70% will be dissolved inside the RBCs[5]. The protons H^+ are dissociated from the carbonic acid and dif-

---

[5] The remaining 23% will bind to the hemoglobin, forming carbaminohemoglobin

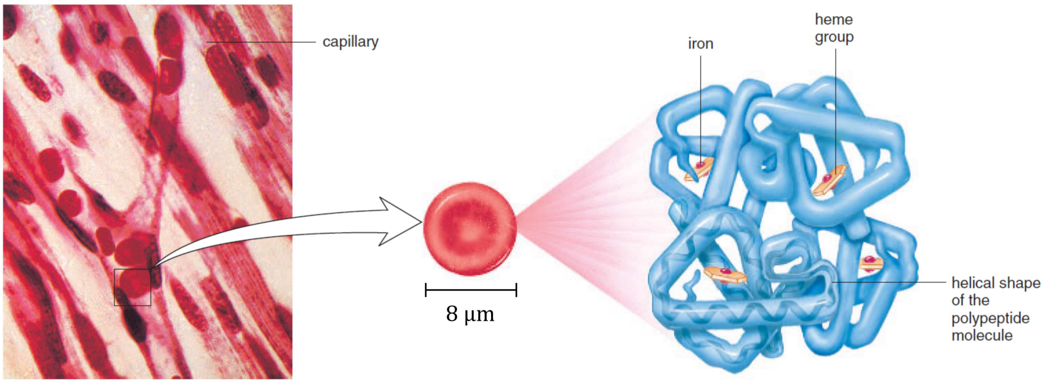

a. Blood capillary b. Red blood cell c. Hemoglobin molecule

Figure 1.4: a) RBCs flowing in capillaries and subject to deformations when passing through. b) The stress free biconcave disk shape of a single RBC. c) Each RBC contains around 200 million molecules of hemoglobin, responsible of transporting oxygen from the lungs to the tissues and carrying out a part of the carbon dioxide from the tissues to the lungs. Modified from [Mader 2001].

Figure 1.5: Left: An individual red blood cell entering in a capillary. The ratio between the diameter of the RBC and the one of the capillary is around unity. Credits: Science Photo Library. Right: Colored scanning electron micrograph showing red and white blood cells inside a small blood vessel after freeze fracturing. This technique consists on freezing quickly the sample by using liquid nitrogen. The inner structure of the vessel is revealed after fracturing with a microtome, which is a knife-like instrument for cutting thin tissue slices. From the vessel's size, it looks like a tiny vein or a venule. Credits: Steve Gschmeissner, Bedfordshire.

fuse out to the plasma together with the bicarbonate ions ($HCO_3{}^-$). The pH will be lowered due to the protons H^+. The opposite reaction occurs in the lungs, where the pH level will increase. These reactions are very important to the homeostasis (equilibrium and functioning) of the body. The time needed to the hydration of the carbon dioxide is quite slow. However, and here we can feel the beauty and efficiency of nature, the RBCs contain an enzyme the Carbonic anhydrase, that plays the role of a catalyst (accelerator) of the reaction in both directions, at least 250

times faster than in the plasma.
RBCs have no nucleus, thus they can not divide and reproduce like the other cells. The production of the RBCs occurs in the bone marrow and is controlled and regulated by the kidney via the secretion of the erythropoietin, a small protein of 34 kDa which plays the role of a hormone and helps to maintain a relatively constant level of oxygen in the body. The red color of the RBCs comes from the hemoglobin, an iron-containing protein to which the oxygen can bind. One molecule of hemoglobin consists of 4 subunits called globins (4 polypeptide chains). Each subunit contains a heme group (iron-carrying part), where a molecule of oxygen can bind. A vessel containing oxygenated RBCs (activated form of the hemoglobin also called oxyhemoglobin) has a bright red color (*e.g.* in the arteries), whereas the color becomes bluish-red after the release of the oxygen by the RBCs (*e.g.* in the veins). The fresh inhaled oxygen diffuses into the blood and then into the red cells following a down gradient (alveolar air is richer in oxygen than the blood entering in the lungs capillaries therefor a diffusion of O_2 toward the poorest region will occur). Inside the RBCs, the oxygen will bind to the hemoglobin which can carry up to 4 molecules of O_2 following the reaction:

$$\mathrm{Hb} + \mathrm{O}_2 \longrightarrow \mathrm{HbO}_2$$

where Hb stands for deoxyhemoglobin and HbO_2 for oxyhemoglobin. The inverse reaction will occur when the oxygen will be delivered in the tissues.

The anatomy of a RBC reveals a bilayer membrane containing 60% of proteins and 40% of lipids, linked in its inner part to a cytoskeleton composed from a dense network of spectrin, actin and other proteins that stabilize the structure of the network. The outer part of the bilayer membrane is covered by a coat of glycoproteins called the glycocalyx, where the membrane receptors and ion pumps (transporters[6] and channels[7]) are located. The glycocalyx is very important for the mechanotransduction (signalization processes where a mechanical signal or force is transformed into a cellular biomolecular response) of the RBCs. The spectrin protein is coupled to the membrane (to the transmembrane proteins Band III) via the ankyrin proteins. The Band III is where the diffusion of the chloride and specially the bicarbonate ions across the membrane occurs. Recall that bicarbonate ions are residues from the respiration process occurring inside the RBCs. Whereas the actin protein is linked to the glycophorin via the protein Band 4.1. The glycophorin is a glycoprotein (sugar + protein) with a high content of sialic acid residues. Recall that the sialic acid gives to the RBC membrane its highly negative charge. The cytoskeleton is believed[8] to give to the cell its biconcave shape. The mechanical properties of the cytoskeleton and the bilayer membrane will be discussed in the chapter 3. The RBC encloses a liquid, the cytoplasm, which has

---

[6] Transporters are pump that requires energy to move molecules across the membrane.

[7] Channels are selective pumps that allow only a certain type of molecules to pass across the membrane.

[8] We will show on chapter 3 that a closed bilayer membrane without a cytoskeleton can also adopt the biconcave shape at equilibrium.

a viscosity lying between $5-7$ cP (for a young rbc), whereas the viscosity of the plasma is roughly the same as water 1 cP. The value of the cytoplasmic viscosity is dictated by the mean corpuscular hemoglobin concentration (MCHC). Giving a fixed value to the cytoplasmic viscosity of the RBC is misleading in the sens that the volume of the RBC decreases with time whereas the amount of hemoglobin remains constant. To illustrate this fact by an example, the cytoplasmic viscosity of a RBC is approximatively 7 cP at a MCHC of 32 g/dL[Chien 1987, Guido 2009]. This value is known to be the typical one for a young red blood cell just released to the circulation from the bone marrow. At a MCHC of 40 g/dL, the cytoplasmic viscosity is nearly quadrupled [Chien 1987]. Besides it has been reported in [Cokelet 1968] that the value of the cytoplasmic viscosity increases in a non-linear manner with the MCHC. How can one model then cells that can loose gradually with time their volume and surface, whereas their inner viscosity will increase in a non-linear fashion? Unfortunately, we are not going to answer completely to this question, but elements of answers regarding how the cytoplasmic viscosity may affect the shape of the RBC will be discussed in the chapter 4. The changes in the inner viscosity, surface, and volume with age will affect the deformability of the RBC and alter its ability to pass through narrow capillaries, which explain the short lifespan of the RBCs, and the reason why a RBC does not have a nucleus. Some interesting facts about the life of healthy human RBCs are summarized in table1.1.

The membrane of the RBC is a two dimensional viscoelastic fluid with a surface viscosity ranging from $0.47-1$ μNs/m[Guido 2009]. The applied forces are distributed on the side of a surface element due to the fixed thickness, resulting to the dimension force per unit of length instead of the more intuitive force per unit of area (notion of stress). Indeed the membrane can not change its thickness due to an in-plane stress. The membrane surface viscosity of the RBC is three orders of magnitude greater than the viscosity of the lipid components of the membrane[Evans 1976]. This suggests a small or neglectable contribution of the lipids to the viscoelasticity of the membrane. Therefor a part of the mechanism

Life data of human RBCs	
Production rate	$2.4\cdot10^{6}$ per s
Daily loss	$2.1\cdot10^{11}$ per s
Total number of RBCs	$2.5\cdot10^{13}$ per s
Distance traveled during the 120 day lifespan	400 km
Cell weight	$3\cdot10^{-11}$ g
Cell surface	140 μm^2
Cell volume	110 μm^3

Table 1.1: Generalities about RBCs. Data reproduced from [Lipowsky 1995, p. 10].

is not taken into account when vesicles (closed bilayer membranes) are used to model RBCs. However the notion of membrane surface viscosity as well as shear resistance (property akin to the cytoskeleton of the rbc) are meaningless in two dimensions where the membrane is represented by an one dimensional contour.

The biconcave discoid shape of the RBC is common to most mammals with only one exception: the camelids (such as llama, alpacas, vicuñas, and dromedary) who have flattened ellipsoid RBC without biconcavity or biconvexity [Reynafarje 1975, Yagil 1974]. The average diameter of the mammalians RBC ranges from 2.1 to 11.4 µm with no correlations between the size of the animal and the size of the RBC. Indeed, the average diameters of RBCs of humans, sheep, and rat are namely 8 µm, 4.4 µm, and 7.5 µm. However the mammalian capillaries seem to have a relatively constant mean diameter[9] of 4 µm. A comparative study of the deformability of different mammalian RBCs reveals that the deformability is significantly correlated to cell size: the larger the cell, the more deformable it should be, yet this generalization fail in the case of the elliptical RBCs of the llama and the dromedary where no deformation was observed [Smith 1979]. Experiments on the transit times (TT) required by RBCs from different mammals to pass through narrow capillaries of 5 µm diameter tend to contradict the previous affirmations on the relation between deformability and cell size [Baskurt 1996]. Table 1.2 shows the obvious relation between deformability measured via the TT, the dimension of the RBC, and the mean corpuscular volume (MCV).

The dimension of the RBCs of the rat and the human is relatively the same, but the MCV of the human RBC is roughly the double of the one of the rat. Meanwhile the TT to pass through the channel is significantly slower for the human RBCs in comparison to rat RBCs. This is reflected by the MCV rather than by the diameter. Yet, the passage time is also affected by the ratio of cell size/capillary size, since species with RBCs of small diameter are subject to less deformation which explains the differences in the TT between sheep RBCs and human RBCs in the 5 µm channels. Coming back to the shape of the mammalian RBCs, a comparison between the camelids family and the other mammalians families is given

	Sheep	Mouse	Rat	Human
Shapes	BDS	BDS	BDS	BDS
Diameters (µm)	4.4	6.8	7.5	8
MCV (fL)	29	41.5	51.6	89.2
Average transit times (ms)	1.44	1.61	1.94	3.02

Table 1.2: Comparative data of mammalians RBCs passing through capillaries of 5 µm diameter. MCV and BDS stand namely for mean corpuscular volume and biconcave discoid shape. References for the average transit times and MCV from [Baskurt 1996]; and for the diameters and shapes from [Smith 1979].

---

[9] data about cells and capillary diameters are from [Smith 1979]

in Table1.3. In contrary to human RBCs, camelids (llama and dromedary) RBCs show almost no aggregation [Baskurt 2007, p 275-276] even though the concentration of fibrinogen, one of the inducing agent of aggregation, is roughly the same between the three mammals. In contrast to mammalians, other species (amphibians, fish, reptiles, and birds) possess a nucleated RBC, typically flattened ellipsoids like the mammalian family of the camelids but with a biconvexity produced by bulging in the region of their nucleus (see Fig 1.6). Like for anucleated ellipsoid mammalian RBCs (*i.e.* camelids), no aggregation was observed for nonmammalian ellipsoid nucleated RBCs [Baskurt 2011, p 269]. Therefor the biconcave discoid shape is a prerequisite for RBCs aggregation. Nevertheless, not all biconcave disk-shaped mammalian RBCs can aggregate (*e.g.* sheep, cow, and mouse) [Baskurt 2011, p 278]. We can be tempted at this level to build assumptions based on the MCV and the biconcave discoid shape to explain the aggregability of RBCs. Aggregability of RBCs from different mammalian species is presented in Table 1.4 with the corresponding values of MCV, cell size and plasma fibrinogen levels. Even though all these species possess a biconcave discoid RBCs, it seems that no possible correlation between MCV or any other parameter with aggregability can be made. Thus either is a combination of different parameters that defines RBCs aggregability, either we should look in an other direction.

	Llama	Dromedary	Human
Shape	oval	oval	BDS
MCV (fL)	$24-28$	$28.5-33$	$89-90$
Dimensions (µm)	7.4×3.3	7.7×4.2	8
Thickness (µm)	1.1	unavailable data	2.4
Fibrinogen (mg/mL)	$1.77-3.77$	$2.63-3.57$	$1.8-4$
Lifespan (days)	60	unavailable data	120

Table 1.3: Comparative data of camelids (llama and dromedary) and humans RBCs. MCV stands for mean corpuscular volume. References for Llama [Reynafarje 1975, Khodadad 1983, Welles 1997]; for dromedary [Banerjee 1962, Yagil 1974, Baghshani 2010]; and for humans [Comeglio 1996, Baskurt 1996, Baskurt 2011].

Let us stick to the mammalian species and try to compare the mechanical properties akin to the composition of the RBC membrane of llamas and humans without taking into account the oval shape of the llama's RBCs. The first observation is that the level of sialic acid is more important in the llamas RBCs. We recall that the negative charge of the RBC depends on the amount of sialic acids, and that aggregation was studied in presence of fibrinogen which is a negatively charged protein that induce aggregation regardless from the presence of other plasma proteins. The concentration of the transmembrane protein Band III is three times higher in the llamas RBCs than in the humans RBCs [Khodadad 1983]. Recall that the spectrin

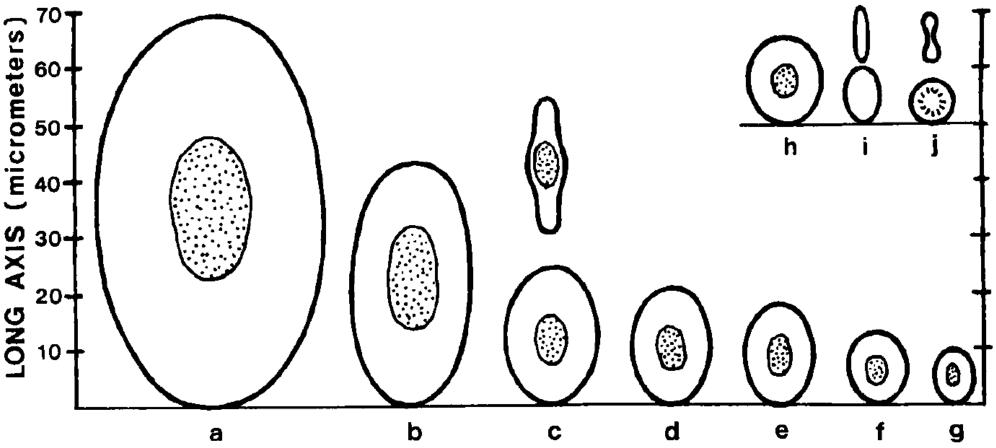

Figure 1.6: Size and morphology of vertebrate RBCs. Cells a-g, nonmammals; cells h-j, mammals. (a) Amphiuma tridactylum (giant salamander); (b) Notophthalmus viridescens (Eastern newt or salamander); (c) Rana pipiens (leopard frog; face and edge view); (d) Mustelus canis (smooth dogfish); (e) Anolis carolinensis (anole, a lizard); (f) Carassius auratus (goldfish); (g) Gallus domesticus (chicken); (h) Monodelphis domestica (gray short-tailed opossum; primitive erythrocyte of neonate); (i) Camelus dromedarius (camel, adult; face and edge view); (j) Homo sapiens (human, adult; face and edge view). Reproduced from [Jeon 1992, p. 39].

	Diameters (μm)	MCV (fL)	Hematocrit (%)	Fibrinogen (mg/mL)	Aggregability
Sheep	4.4	34	33	2.82	N
Mouse	6.8	45	40	2.83	N
Cow	5.8	52	30	3.09	N
Rat	7.5	47	43	2.33	L
Dog	7.6	61	45	1.82	M
Human	8	90	45	2.9	M
Cat	6.01	40	40	1.86	I

Table 1.4: Comparative data of mammalians biconcave discoid RBCs, fibrinogen concentrations, and aggregability. I, M, L and N stands namely for intensive, moderate, low, and no aggregation. References for the average MCV, hematocrit, fibrinogen concentration, and aggregability are from [Windberger 2003, Baskurt 2011]; and for the diameters from [Smith 1979, Lipowsky 1980].

network is linked to the Band III via the ankyrin protein. Therefor it is more likely that the more Band III, the strongest the bonds are which lead to more resistance to deformation. Indeed, both the dromedary and the llama have a higher protein-to-lipid ratio in the membrane and an unusual osmotic resistance. Their membrane is more rigid than those of other mammals (humans included) [Smith 1979]. This property is common in other nonmammalian species with an elliptical RBCs. The membrane rigidity of nucleated RBCs from amphibians (frogs, turtles, iguanas, and amphiuma), reptiles (snakes), birds (turkeys), fish (toadfish, rainbow trouts), and anucleated RBCs from mammals (humans, and opossum) was measured using micropipette experiments; which describe the membrane's resistance to shear deformation at constant area. The outcomes were that the membrane rigidity of nucleated RBCs is higher than for anucleated RBCs [Waugh 1976, Nash 1993]. It is important nevertheless to highlight the difference in the membrane composition between nucleated elliptical RBCs and the anucleated ones from the camelids. Without lost of generalities, the origin of the membrane rigidity is not the same. But regardless this fact, no aggregation is observed for the camelids family and the nonmammalian species. It is tempting therefor to draw the assumption that the aggregability is depending from the level of sialic acid, the membrane rigidity and to a certain extend the biconcave discoid shape. This last point might be subject to debate, because in the microcirculation, the biconcave RBCs change their shape and are still able to aggregate under certain conditions (see chapter 6). But since the interplay between the cell parameters, the membrane composition, and the plasma proteins remain unclear for a given specie, it is more likely impossible to decouple this variables by comparative studies between different species.

1.2.4 A short note about blood rheology in microcirculation

In this subsection, we will talk briefly about two important phenomena regarding the flow of a suspension of RBCs in vessels or tubes of a diameter smaller than 300 μm. The first one is the Fåhraeus effect [Fåhraeus 1929] and states that the concentration of RBCs in the larger feeding vessel is higher than the one of the subsequent small vessels. This is the consequence of two important characteristics of the flow in the microcirculation: i) the lateral migration of the RBCs toward the centerline of the Poiseuille flow; and ii) the difference of velocities of the different layers of the plasma due to the parabolic profile of the Poiseuille flow lead to a slow-moving plasma layer near the walls in opposition to the layers near the centerline of the flow. Concisely the hematocrit in the human capillaries is known to be lower than 20%, whereas the average hematocrit in the large vessels is around 45%. The hematocrit means the concentration of the red blood cells over the total volume of the circulating blood in the tube. A set of data for the hematocrit average in different vessels for golden hamsters is given in table1.5.

The inverse effect is observed for white cells and platelets meaning the concentration of the cells increase with the decrease of the diameter of the tube and is known as the inverse Fåhraeus effect [Goldsmith 1999].

The second effect is a consequence of the first one, and describes the decrease of the relative viscosity with vessel diameter. Indeed the thickness of the slow-moving peripheral layers of plasma will decrease the energy dissipation near the walls during the flow and contribute to the reduction of the relative viscosity. This is known as the Fåhraeus-Lindqvist effect [Fåhræus 1931]. More details about Fåhraeus and

Measured hematocrit average	
Small arteries of ID=100 − 200 µm	49.4 ± 1.1 %
Arterioles of ID=14.2 ± 1.2 µm	13.9 ± 1.2 %
Capillaries of ID=5.1 ± 0.1 µm	10.4 ± 2.0 %

Table 1.5: Measured hematocrit average in different vessels of the golden hamster [Klitzman 1979]. ID refers to internal diameter of the vessel.

Fåhraeus-Lindqvist effects can be found in this review paper [Goldsmith 1989], and a very good general introduction to the principles of rheology and the biophysical behavior of RBCs in suspensions are given in Ref. [Surgenor 1975, p. 1031]. It has been shown recently that the organization of the cells is going to affect the normalized effective viscosity, a rheological quantity of interest to understand the properties of blood flow; a relation between the confinement, the hematocrit and the viscosity has been proposed in [Thiébaud 2014]. As a consequence, the spatial organization of the cells may be an additional cause leading to the Fåhraeus-Lindqvist effect.

CHAPTER 2

State of Art

The main results of the previous PhD theses in our group and external contributions will be summarized in this chapter. This will help to show the link between the actual work, and what was done before. A proper literature survey will be given in the beginning of each chapter before expanding the results obtained in this thesis.

Overview on the previous PhD's theses:

I. Cantat's PhD ([Cantat 1999a]): A theoretical model based on vesicles to investigate cell migration was proposed, followed by a numerical study. Two cases were considered: i) haptotaxis which means a migration driven by an adhesion gradient [Cantat 1999b, Cantat 2000, Cantat 2003]; and ii) migration of a vesicle near a wall due to a shear flow [Cantat 1999c]. The theoretical framework that will be used later on in this thesis was crafted partially here, and used also as a basis in [Kaoui 2009a, Ghigliotti 2010a].

B. Kaoui's PhD ([Kaoui 2009a]): A vesicle subject to a shear flow exhibits three dynamics: tank-treading, vacillating-breathing or swinging, and tumbling. When tank-treading, the cell adopts a steady state inclination angle with respect to the flow direction, whereas each node of the membrane will translocate all the way around the cell. During the tumbling, the inclination angle with respect to the flow direction describes periodic rotation cycles over time (wheel-like motion). In the vacillating-breathing dynamic, the inclination angle with respect to the flow direction oscillates periodically (without making full rotations) and the membrane undergoes large deformations. The effect of the viscosity contrast (ratio between inner and outer viscosities of the two fluids) and the capillary number (dimensionless parameter describing the strength of the flow over the membrane rigidity) was investigated using dynamical equations (small deformation theory) describing the evolution of the orientation angle of the vesicle and the deformations of the membrane. The results were summarized in a phase diagram, with a special attention given to the study of the vacillating-breathing regime, the less known of the these three dynamics [Kaoui 2009c]. The effect of confinement on the tank-treading regime was studied using a Lattice Boltzmann method[Kaoui 2011a]. The lateral migration of a single vesicle under a shear flow and a Poiseuille flow was also investigated. Under a shear flow, a vesicle placed in an unbounded geometry does not exhibit a lateral migration, whereas in a semi-bounded geometry, a vesicle located near a wall will migrate away from it. This migration is attributed to a breaking of the symmetry in the perpendicular axis to the flow direction and to the characteristic upstream-downstream symmetry of the shear flow. Recalling that a Poiseuille flow is a local shear flow, and that it has a non uniform shear rate globally (the value of shear rate depends of the position following the perpendicular axis to the flow direction). In this case, the vesicle is subject to different shear stresses depending on its lateral position. In both unconfined and semi-bounded geometries, a lateral migration toward the center of the flow was observed. A law to describe this migration was derived as a function of the intrinsic properties of the vesicle and the flow parameters [Kaoui 2008, Coupier 2008], and the minimum ingredients to observe an asymmetric shape (slipper-like) was discussed [Kaoui 2009b].

G. Ghigliotti's PhD ([Ghigliotti 2010a]): The rheological properties of a dilute suspension were studied in a unbounded shear flow [Ghigliotti 2010b]. These properties were deduced from the dynamics of an isolated vesicle (assumption valid for a very dilute suspension). The tumbling motion was investigated in the case of very deflated vesicles [Ghigliotti 2009]. It was shown that this dynamic might occur also when the viscosity ratio was equal to unity, a result that was not expected from former studies on quasi-spherical vesicles (*e.g.* [Kaoui 2009a]). The migration of a vesicle in a Taylor-Couette geometry (two coaxial cylinders) was studied. Both cases unbounded and bounded flows were considered. The unbounded case allows to exclude the effect of the walls on the migration and focuses only on the flow parameters and the intrinsic properties of the vesicle. It was observed that the tank-treading vesicles migrated inwards, whereas the tumbling vesicles did not. This study revealed that the migration velocity is related the first normal stress difference. Indeed, for a positive normal stresses, the vesicle migrate inwards (case of a tank-treading vesicle). Whereas for tumbling vesicles where no migration was observed, the normal stresses equals zero. The effect of the walls was considered in the case of a single vesicle with a viscosity ratio set to unity and for different reduced area[1]. It was observed that regarding of the initial position or the reduced area, the vesicle has a tendency to migrate toward the same position located between the inner cylinder and the centerline of the flow. Thus the force driving the inward migration rescales with the reduced area. Then the system was extended to investigate the behavior of a set of quasi-spherical vesicles (4 and 7 vesicles). The main result was the observation of a self-organization where the vesicles keep the same interdistance at steady state [Ghigliotti 2011]. The last project studied in this thesis was about the formation of trains of cells (clusters) in an unbounded Poiseuille flow [Tomaiuolo 2012]. The main outcome was that a cluster has a maximum length above which it become instable and the first cells start to detach[Ghigliotti 2012].

N. Tahiri's PhD ([Tahiri 2013a]): In this thesis, the numerical work done in an unconfined Poiseuille flow for the case of a single vesicle [Kaoui 2009a] was extended by adding to bounding quasi-rigid walls. A systematic study of the effect of the capillary number, viscosity ratio and confinement on the shape of the single vesi-

---

[1] area of the cell over the area of a disk having the same perimeter as the cell

cle was performed. The results was summarized in phase diagrams [Kaoui 2011b, Tahiri 2013b].

P. Steffen's PhD [Steffen 2012]: Besides the experimental study of some aspects of the mechanism of thrombus formation and the role of red blood cells in it [Nguyen 2011, Steffen 2011, Kaestner 2012], a quantification of the adhesion energy between two red blood cells suspending in a medium containing dextran was performed for the first time using single cell force spectroscopy technique [Steffen 2013]. This last project was done in collaboration with the Laboratoire Interdisciplinaire de Physique in Grenoble (France).

L. Lanotte's PhD [Lanotte 2013]: The flow of RBCs in microchannels was studied experimentally. Both hydrodynamic interactions and interaction between the wall's glycocalyx and the RBCs have been investigated. The outcomes of this work can be summarized as follows: i) the hydrodynamic interactions can be considered as the minimal ingredient leading to the formation of clusters. ii) the polydispersity of the RBCs within the physiological range does not affect the stability of the clusters [Tomaiuolo 2012]. iii) the presence of the wall's glycocalyx (via polymer brushes fixed on the glass capillaries) above a specific brush thickness leads to a significant decrease of the RBCs velocity. This phenomenon is not observed below this specific brush thickness, and may be explained by a change of shape of the RBCs to conserve the same velocity as in the absence of the glycocalyx on the walls [Lanotte 2014].

M. Brust's PhD [Brust 2013a]: An experimental work was carried out on the rheological properties of red blood cells, and the previous work of P. Steffen on the adhesion energy between two red blood cells was extended for the case of fibrinogen. Two main topics were investigated: i) the rheological properties of the plasma; and ii) the aggregation of red blood cells and cluster formation in microcirculation in presence and in absence of macromolecules inducing aggregation (*e.g.* dextran or fibrinogen). The main findings are: i) the plasma has a viscoelastic behavior [Brust 2013b]; ii) the clusters formed due to macromolecules persists in the microcirculation even at high shear rates (physiological levels) [Brust 2014]. Both results were unexpected, particularly if we refer to the literature.

External contributions and collaborations:

Prof. Dr. H. Selmi: An applied mathematician at the École Polytechnique de Tunise (Tunisia) who contributed to implement the quasi-rigid walls used in [Tahiri 2013a]. He also implemented a fast multipole method to speed up the calculation of the matrix-vector products, helping to reduce the computational cost from $\mathcal{O}(N^2)$ to $\mathcal{O}(N)$ [Selmi 2011]. He also collaborates in the present work.

Dr. M. Thiébaud: A former Post-doc in the group of C. Misbah in LIPHy who contributed actively to the actual work, and rederived the two dimensional wall green's functions [Thiébaud 2013].

Prof. Dr. T. Biben: Professor in the Institut Lumière Matière at Lyon (France) who wrote the original code that was modified in the present work, as well as the three dimensional code that I used during my master thesis to study the tank-treading of quasi-spherical vesicles [Farutin 2012].

Contributions of the present work:

Numerical results about clusterization in a unbounded geometry [Ghigliotti 2012] and preliminary experimental results on the hydrodynamic and macromolecules induced clusters have motivated the actual work. We therefor developed the necessary tools to study cluster formation in microchannels in the presence of macromolecules at different concentrations. The findings were in good agreements with the experimental results and lead to a join publication [Brust 2014]. However two important things draw our attention: i) our numerical findings were not in agreement with the unbounded results from [Ghigliotti 2012]; ii) even though the agreement was good with the experiments, we were not yet able to distinguish the exact contribution of hydrodynamic and macromolecule induced interactions. Indeed the non-trivial coupling between the hydrodynamic interactions between the cells and the depletion-bridging effect induced by the surrounding macromolecules from one hand, and the contribution of the rigid walls of a microchannel on the total hydrodynamic interactions from the other hand is a challenging problem that needs to be split up. Thus, we decided to start by studying the effect of rigid walls on the flow of an isolated vesicle. Then we studied the aggregation between cells in a static fluid. The next step was to study the pair formation induced only by hydrodynamic interactions and the effect of the confinement on it. Each one of this studies lead to surprising and unexpected results that shed light on the complexity behind the interplay between the flow parameters, the intrinsic properties of the vesicle membrane and the confinement.

First contribution:

The dynamics of an isolated vesicle in a confined Poiseuille flow were investigated. In addition to the classical parachute-like and slipper-like shapes, complex dynamics were observed. A Chaotic motion of the vesicle occurs through a cascade of multiple periodic oscillations. The effect of the capillary number and the confinement was summarized in a phase diagram. In addition the shape transition from parachute-like to slipper-like shape in microcirculation was correlated to one of the intrinsic property of the rbc namely the cytoplasmic viscosity. These findings are discussed in chapter 4 and published in [Aouane 2014].

Second contribution:

This part was motivated by the discrepancy between the results of the confined and the unconfined Poiseuille flow on cluster formation. The effect of the geometry on the hydrodynamic interaction and the mechanism of pairing was investigated. the critical confinement leading to the same results as the unbounded case was found. A change of sign of the hydrodynamic interaction leading to repulsion between the vesicles was observed under certain conditions. The results were summarized in a phase diagram and are discussed in chapter 5.

Third contribution:

The flow of trains of red blood cells (modeled as vesicles) in confined geometries (microchannels) and the effect of the concentration of the macromolecules were studied. A model to describe the interaction induced by the macromolecules was proposed. The model is used to study aggregation of red blood cells in a static fluid, then to investigate the effect of macromolecules on RBCs cluster formation in the microcirculation. The outcomes are detailed in chapter 6 and published in [Brust 2014].

CHAPTER 3

Theoretical Framework

Contents

The actual mathematical formulation of the fluid motion goes back to almost two hundred years thanks to the work of the swiss mathematician and physicist Leonhard Euler (1707-1783), the French engineer and physicist Louis Claude Navier (1785-1836) and the Irish mathematician and physicist Georges Gabriel Stokes (1819-1903). Euler contributes to the description of the motion of an inviscid fluid based on the conservation laws of classical physics. Navier and later Stokes introduced the viscous transport into Euler equations by relating the stress tensor to the fluid motion, resulting to a more general set of equations, the so-called Navier-Stokes equations. This equations constitute the basis of the computational fluid dynamic (CFD) field. The scope of this chapter is to build a model to study the motion of a deformable object in a fluid based on the boundary integral method for Stokes equations. For a general introduction to fluid mechanics, the reader may refer to [Aris 1989, Batchelor 2000, Morrison 2001].

3.1 Stokes Flows

For an incompressible fluid —the density ρ does not change in space or time —the continuity equation becomes

$$\nabla \cdot \mathbf{u} = 0 \tag{3.1}$$

and the so-called equation of motion for incompressible Newtonian fluids is given by

$$\rho \frac{D\mathbf{u}}{Dt} = -\nabla p + \mu \nabla^2 \mathbf{u} + \rho \mathbf{f}_b \tag{3.2}$$

which can also be written in a more explicit form

$$\rho(\frac{\partial u_i}{\partial t} + \sum_{j=1}^{N} u_j \frac{\partial u_i}{\partial x_j}) = -\frac{\partial p}{\partial x_i} + \mu \sum_{j=1}^{N} (\frac{\partial^2 u_j}{\partial x_j^2} + \frac{\partial^2 u_j}{\partial x_i \partial x_j}) + \rho f_{b_i}, \quad 1 \leq i \leq N \tag{3.3}$$

where N is the dimension of the problem. Starting from the equations of mass conservation and linear momentum conservation, thanks to the Newtonian constitutive equation, and using the assumption of incompressibility, we have reconstructed the so-called Navier-Stokes equations for incompressible Newtonian fluids (3.1) and (3.2).

A more convenient way to write the Navier-Stokes equations is by introducing a dimensionless parameter, the Reynolds number ($\mathscr{R}_e$), that describes the predominance between the inertial forces and the viscous forces. For this purpose, let U be the characteristic velocity of the flow, L the characteristic length, and T the characteristic time of the flow. In absence of external forcing of the flow (i.e. by imposing an oscillatory flow), the characteristic time of the flow is usually associated to the convective time of the flow $T = L/U$. For creeping motion, it is more intuitive to use the diffusion time $T = \rho L^2/\mu$ as the characteristic time for the flow to underline the predominance of the viscous forces. Note that the Reynolds number can also be defined as the ratio between the diffusion time $\rho L^2/\mu$ and the convective time L/U of the flow. Then, by introducing the following dimensionless variables

$$x^* = x/L, \quad \mathbf{u}^* = \mathbf{u}/U, \quad t^* = t/T, \quad p^* = \frac{pL}{\mu U}, \quad f_{b_i}^* = \frac{f_{b_i}}{|\mathbf{f_b}|}$$

we write 3.3 in a dimensionless form

$$\frac{\partial u_i{}^*}{\partial t^*} + \mathscr{R}_e \sum_{j=1}^{N} u_j^* \frac{\partial u_i^*}{\partial x_j^*} = -\frac{\partial p^*}{\partial x_i^*} + \sum_{j=1}^{N} (\frac{\partial^2 u_j^*}{\partial x_j^{*2}} + \frac{\partial^2 u_j^*}{\partial x_i^* \partial x_j^*}) + \frac{\mathscr{R}_e}{\mathscr{F}_r} f_{b_i}^*, \quad 1 \leq i \leq N \tag{3.4}$$

Two dimensionless quantities appear in the above equation namely the Reynolds number ($\mathscr{R}_e = \frac{\rho L U}{\mu}$), and the Froude number ($\mathscr{F}_r = \frac{U^2}{L|\mathbf{f_b}|}$) which describes the magnitude of inertial convective forces relative to body forces.

If the rate of change of momentum of a volume V of fluid is small compared to the sum of all forces acting on this volume of fluid, the motion of the flow is governed by the balance between the surface force (molecular forces) and the volume force (body forces). Thus, the nonlinear convective term in the LHS of the equation of motion vanishes, leading to the linearized Navier-Stokes equations or Stokes equations. These equations reflect the creeping motion, when the viscous forces dominate the inertial forces, underlying a low Reynolds number. The time-independent (steady motion) Stokes equations for an incompressible Newtonian fluid take the form

$$\nabla \cdot \sigma = -\nabla p + \eta_o \nabla^2 \mathbf{u} = -\rho \mathbf{f}_b \tag{3.5}$$

$$\nabla \cdot \mathbf{u} = 0 \tag{3.6}$$

The solution of Stokes equations can be written in the form of an integral equation and then solved numerically.

3.2 Boundary integral equation for Stokes flow

Several textbooks dedicated to the boundary integral technique and its applications to study microhydrodynamics in viscous flows exist. Books like [Ladyzhenskaya 1969, Kim 2013, Pozrikidis 1992, Barthès-Biesel 2012] give a full overview of the mathematical basis of this technique and discuss the numerical applications. Pseudocodes to compute different kind of flows can also be found in [Pozrikidis 2002, Kim 2013]. In the following section, we summarize the main steps to build an integral equation for Stokes equations.

3.2.1 Lorentz reciprocal theorem

Let us suppose that the velocity fields $\mathbf{u}$ and $\mathbf{u}'$ both satisfy the Stokes equations. We denote their associated stress fields as σ and σ' respectively. Assuming that the two fluids have the same viscosity, the Lorentz reciprocal theorem states that

$$\nabla \cdot (\mathbf{u} \cdot \sigma' - \mathbf{u}' \cdot \sigma) = 0 \tag{3.7}$$

Now by integrating over a closed region of volume V bounded by a surface A, and using the divergence theorem, the Lorentz identity takes the form

$$\oint_A \mathbf{u} \cdot (\sigma' \cdot \mathbf{n}) dA = \oint_A \mathbf{u}' \cdot (\sigma \cdot \mathbf{n}) dA \tag{3.8}$$

where $\mathbf{n}$ is the normal unit vector pointing outside V. Note that $\mathbf{u}$ and $\mathbf{u}'$ are assumed to be regular (i.e. there is no singularity in the domain V). The proof of the Lorentz identity can be obtained by evaluating the expression:

$$u'_i \frac{\partial \sigma_{ij}}{\partial x_j} - u_i \frac{\partial \sigma'_{ij}}{\partial x_j}$$

The sequence of steps are:

$$u'_i \frac{\partial \sigma_{ij}}{\partial x_j} = \frac{\partial}{\partial x_j}(u'_i \sigma_{ij}) - [p\delta_{ij} + \mu(\frac{\partial u_i}{\partial x_j} + \frac{\partial u_j}{\partial x_i})]\frac{\partial u'_i}{\partial x_j} \tag{3.9}$$

$$= \frac{\partial}{\partial x_j}(u'_i \sigma_{ij}) - \mu(\frac{\partial u_i}{\partial x_j} + \frac{\partial u_j}{\partial x_i})\frac{\partial v'_i}{\partial x_j} \tag{3.10}$$

Thanks to the continuity equation, $p\delta_{ij}\frac{\partial u'_i}{\partial x_j} = 0$, leading to the equation 3.10. Repeating now the same steps and interchanging the role of primed and unprimed variables, we show that

$$u_i \frac{\partial \sigma'_{ij}}{\partial x_j} = \frac{\partial}{\partial x_j}(u_i \sigma'_{ij}) - \mu(\frac{\partial u'_i}{\partial x_j} + \frac{\partial u'_j}{\partial x_i})\frac{\partial u_i}{\partial x_j} \tag{3.11}$$

By subtracting 3.11 from 3.10, we obtain the general form of the reciprocal theorem for two Newtonian fluids with the same viscosity

$$\frac{\partial}{\partial x_j}[(u'_i \sigma_{ij}) - (u_i \sigma'_{ij})] = u'_i \frac{\partial \sigma_{ij}}{\partial x_j} - u_i \frac{\partial \sigma'_{ij}}{\partial x_j} \tag{3.12}$$

In a domain without singularities, the RHS of 3.12 vanishes, leading to the simplified expression of the reciprocal identity $\nabla \cdot (\mathbf{v} \cdot \sigma' - \mathbf{v}' \cdot \sigma) = 0$. This result will be used later as a starting point to build the integral form of the Stokes equations.

3.2.2 Integral representation of Stokes equations

Let consider two flows u and u' and their associated stress tensors σ and σ' occurring in the domain Ω enclosed by $\partial\Omega$, and for sake of simplicity, assume that both flows have the same viscosity denoted μ. The flow (u',σ') is the consequence of a point-like force $\mathbf{f}_0$ located at $\mathbf{X_0}$, and its fundamental solutions are given by:

$$u'(\mathbf{X}) = \frac{1}{4\pi\mu}\mathbf{G}(\mathbf{X},\mathbf{X_0})\mathbf{f}_0(\mathbf{X_0}) \tag{3.13}$$

$$\sigma'(\mathbf{X}) = \frac{1}{4\pi}\mathbf{T}(\mathbf{X},\mathbf{X_0})\mathbf{f}_0(\mathbf{X_0}) \tag{3.14}$$

where $\mathbf{G}$ and $\mathbf{T}$ are the green's function and its associated Stress tensor. We seek to compute the flow (u,σ), solution of the Stokes equation

$$\nabla \cdot \sigma = \mathbf{0} \qquad \nabla \cdot \mathbf{u} = 0 \tag{3.15}$$

and obeying to the following boundary conditions:

$$\mathbf{u} = \mathbf{U}(\mathbf{X}) \qquad \mathbf{X} \in \partial\Omega_1 \tag{3.16}$$

$$\mathbf{f} = \sigma \cdot \hat{\mathbf{n}} \qquad \mathbf{X} \in \partial\Omega_2 \tag{3.17}$$

where $\mathbf{U}$ and $\mathbf{f}$ are supposed to be known a priori, $\partial\Omega = \partial\Omega_1 \cup \partial\Omega_2$, and $\hat{\mathbf{n}}$ is the inward pointing normal vector (in opposition to the outward pointing normal denoted $\mathbf{n}$ and used in the Lorentz reciprocal identity). Using the reciprocal identity 3.12, successively integrating over the domain Ω, applying the divergence theorem, and replacing the primed variables by their expression 3.13 and 3.14 leads to:

$$\frac{1}{4\pi\mu}\int_{\partial\Omega} G_{ik}(\mathbf{X},\mathbf{X_0})f_{0,k}(\mathbf{X_0})\sigma_{ij}(\mathbf{X})\hat{n}_j(\mathbf{X})dl \\ -\frac{1}{4\pi}\int_{\partial\Omega} u_i(\mathbf{X})T_{ijk}(\mathbf{X},\mathbf{X_0})f_{0,k}(\mathbf{X_0})\hat{n}_j(\mathbf{X})dl = \int_{\Omega} -u_i(\mathbf{X})\frac{\partial\sigma'_{ij}}{\partial x_j}dA \quad (3.18)$$

Recalling the motion equation $\nabla\cdot\sigma' = -\mathbf{f}_0\delta(\mathbf{X}-\mathbf{X_0})$, using the properties of the 2D Dirac delta function, and substituting $\hat{\mathbf{n}}$ by $\mathbf{n}$, we rewrite the equation 3.18 as

$$-\frac{1}{4\pi\mu}\int_{\partial\Omega} G_{ik}(\mathbf{X},\mathbf{X_0})f_i(\mathbf{X})dl \\ +\frac{1}{4\pi}\int_{\partial\Omega} u_i(\mathbf{X})T_{ijk}(\mathbf{X},\mathbf{X_0})n_j(\mathbf{X})dl = \begin{cases} u_k(\mathbf{X_0}) & \text{if} \quad \mathbf{X_0}\in\Omega \\ 0 & \text{if} \quad \mathbf{X_0}\notin\Omega \end{cases} \quad (3.19)$$

where $\sigma_{ij}n_j = f_i$ is the surface force exerted by Ω on $\partial\Omega$. The first and the second integrals in the LHS are called namely the single and double layer potentials.

The single layer potential is shown to be continuous as the pole $\mathbf{X_0}$ approaches the boundary $\partial\Omega$, however the double layer potential is discontinuous. A demonstration can be found in [Barthès-Biesel 2012, p. 145]. Assuming that $\mathbf{X_0}$ is on $\partial\Omega$, the expression of the double layer is

$$\lim_{\mathbf{X_0}\to\partial\Omega}\int_{\partial\Omega} u_i(\mathbf{X})T_{ijk}(\mathbf{X},\mathbf{X_0})n_j(\mathbf{X})dl = \pm 2\pi u_k(\mathbf{X_0}) + \int_{\partial\Omega}^{PV} u_i(\mathbf{X})T_{ijk}(\mathbf{X},\mathbf{X_0})n_j(\mathbf{X})dl \quad (3.20)$$

where PV denotes the principal value of the double layer potential. The ± sign refers to whether $\mathbf{X_0}$ is approaching from inside (plus sign) or from outside (minus sign). This limit is only valid if the velocity and the normal are smooth across the boundary $\partial\Omega$ (*i.e.* $\partial\Omega$ is a Lyapunov curve, see [Hazewinkel 1990, p. 64] for a detailed definition of Lyapunov surfaces and curves). Substituting 3.20 into 3.19, we find that

$$-\frac{1}{4\pi\mu}\int_{\partial\Omega} G_{ik}(\mathbf{X},\mathbf{X_0})f_i(\mathbf{X})dl \\ +\frac{1}{4\pi}\int_{\partial\Omega}^{PV} u_i(\mathbf{X})T_{ijk}(\mathbf{X},\mathbf{X_0})n_j(\mathbf{X})dl = cu_k(\mathbf{X_0}) \quad (3.21)$$

where c is a constant that takes the following values depending from the position of the pole $\mathbf{X_0}$

$$c = \begin{cases} 0 & \text{if} \quad \mathbf{X_0}\notin\Omega \\ 1 & \text{if} \quad \mathbf{X_0}\in\Omega \\ 1/2 & \text{if} \quad \mathbf{X_0}\in\partial\Omega \quad (\mathbf{X_0} \ \text{approaching from outside} \ \partial\Omega) \end{cases} \quad (3.22)$$

Note that the pole and the target points can be switched, by recalling the symmetry properties of the Green's function and its associated stress tensor

$$G_{ik}(\mathbf{X},\mathbf{X_0}) = G_{ik}(\mathbf{X_0},\mathbf{X}) \tag{3.23}$$

$$T_{ijk}(\mathbf{X},\mathbf{X_0}) = -T_{ijk}(\mathbf{X_0},\mathbf{X}) \tag{3.24}$$

3.2.3 Boundary integral formulation for a single red blood cell in an unbounded geometry

The rbc will be regarded as a deformable particle enclosing an inner fluid with viscosity μ_2 and suspended in an outer fluid with viscosity μ_1. The objective is to study red blood cells via a simplified model based on vesicles, as will be explained later. We impose the following boundary condition

$$\mathbf{u} \mapsto \mathbf{u}^\infty(\mathbf{X}) \qquad\qquad \mathbf{X} \mapsto \infty \tag{3.25}$$

reading as, far from the rbc the velocity $\mathbf{u}$ is assumed to be equal to the velocity of the unperturbed flow $\mathbf{u}^\infty$. Recalling $\mathbf{X_0}$ as the observation (target) point, and assuming that $\mathbf{X_0}$ is located outside the rbc and meantime inside the domain Ω_1, where $\Omega = \Omega_1 \cup \Omega_2$. The boundary equation is given then by

$$u_k^\infty(\mathbf{X_0}) - \frac{1}{4\pi\mu_1}\int_{\partial\Omega} G_{ik}(\mathbf{X},\mathbf{X_0}) f_{1,i}(\mathbf{X})dl - \frac{1}{4\pi}\int_{\partial\Omega} u_i(\mathbf{X}) T_{ijk}(\mathbf{X},\mathbf{X_0}) n_j(\mathbf{X})dl = u_{1,k}(\mathbf{X_0}) \tag{3.26}$$

where

$$G_{ik} = -\delta_{ik}\ln|\mathbf{X}-\mathbf{X_0}| + \frac{(\mathbf{X}-\mathbf{X_0})_i(\mathbf{X}-\mathbf{X_0})_k}{|\mathbf{X}-\mathbf{X_0}|^2} \tag{3.27}$$

$$T_{ijk} = -4\frac{(\mathbf{X}-\mathbf{X_0})_i(\mathbf{X}-\mathbf{X_0})_j(\mathbf{X}-\mathbf{X_0})_k}{|\mathbf{X}-\mathbf{X_0}|^4} \tag{3.28}$$

are the free space Green's functions corresponding to an unbounded geometry. $\mathbf{f}_1 = \sigma_1 \cdot \mathbf{n}$ is the surface force exerted by the outer liquid on the external face of the rbc. Recalling the reciprocal identity, we write the integral equation for the flow inside the vesicle (domain Ω_2) for a point that is located within the domain Ω_1 but outside the domain Ω_2 (where we want to compute the flow)

$$u_k^\infty(\mathbf{X_0}) - \frac{1}{4\pi\mu_2}\int_{\partial\Omega} G_{ik}(\mathbf{X},\mathbf{X_0}) f_{2,i}(\mathbf{X})dl + \frac{1}{4\pi}\int_{\partial\Omega} u_i(\mathbf{X}) T_{ijk}(\mathbf{X},\mathbf{X_0}) n_j(\mathbf{X})dl = 0 \tag{3.29}$$

where $\mathbf{f}_2 = \sigma_2 \cdot (-\mathbf{n})$ is the surface force exerted by the inner liquid on the internal face of the vesicle. Combining 3.26 and 3.29, introducing $\Delta\mathbf{f} = \mathbf{f}_1 - \mathbf{f}_2 = \{\sigma_1 -$

$\sigma_2\} \cdot \mathbf{n}$ as the discontinuity in the interfacial stress force, and recalling $\lambda = \mu_2/\mu_1$, we obtain a boundary integral for a point located outside the rbc

$$u_k^\infty(\mathbf{X_0}) - \frac{1}{4\pi\mu_1}\int_{\partial\Omega} G_{ik}(\mathbf{X},\mathbf{X_0})\Delta f_i(\mathbf{X})dl \\ + \frac{1-\lambda}{4\pi}\int_{\partial\Omega} u_i(\mathbf{X})T_{ijk}(\mathbf{X},\mathbf{X_0})n_j(\mathbf{X})dl = u_{1,k}(\mathbf{X_0}) \quad (3.30)$$

Following the same procedure, we show that the flow for a point $\mathbf{X}_0$ located inside the vesicle is

$$u_k^\infty(\mathbf{X_0}) - \frac{1}{4\pi\mu_1\lambda}\int_{\partial\Omega} G_{ik}(\mathbf{X},\mathbf{X_0})\Delta f_i(\mathbf{X})dl \\ + \frac{1-\lambda}{4\pi\lambda}\int_{\partial\Omega} u_i(\mathbf{X})T_{ijk}(\mathbf{X},\mathbf{X_0})n_j(\mathbf{X})dl = u_{2,k}(\mathbf{X_0}) \quad (3.31)$$

And finally when $\mathbf{X}_0 \mapsto \partial\Omega$ from either sides, the boundary integral takes the following form

$$\frac{2}{(1+\lambda)}u_k^\infty(\mathbf{X_0}) - \frac{1}{2\pi\mu_1(1+\lambda)}\int_{\partial\Omega} G_{ik}(\mathbf{X},\mathbf{X_0})\Delta f_i(\mathbf{X})dl \\ + \frac{(1-\lambda)}{2\pi(1+\lambda)}\int_{\partial\Omega}^{PV} u_i(\mathbf{X})T_{ijk}(\mathbf{X},\mathbf{X_0})n_j(\mathbf{X})dl = u_k(\mathbf{X_0}) \quad (3.32)$$

The proof and calculation details for a three dimensional flow can be found in [Pozrikidis 1992, p 240-241], and stay valid for a two dimensional flow as well. We will in the following section and also in the appendix A, discuss briefly several constitutive equations to model the mechanical properties of the rbc membrane.

3.3 Red blood cell membrane models

The discontinuity in the interfacial force depend from the intrinsic characteristics of the interface (mechanical properties of the membrane), as well as from the physical properties of the inner and outer fluids. In general, for active particles (*e.g.* microswimmers), $\Delta\mathbf{f}$ has a finite value, and contribute actively in the dynamics of the flow. In contrast, passive particles (*e.g.* vesicles and red blood cells) are merely advected by the ambient flow, thus $\Delta\mathbf{f} = \mathbf{0}$. The dependency upon the different physical characteristics of the interface and the fluids needs to be expressed in terms of a constitutive equation. If the inertia of the interface can be neglected, the contribution of both fluids vanishes, and the interfacial surface force ($\Delta\mathbf{f}$) depends then solely from the mechanical properties and composition of the interface. Therefor the differential force balance requires

$$\Delta\mathbf{f} = -\mathbf{f}_{struct\mapsto fluid} \quad (3.33)$$

where $\mathbf{f}_{struct\mapsto fluid}$ is the load exerted by the structure (interface) on the fluid. Several constitutive equations can be found in the literature describing different kind

of interfaces (*e.g* capsules and vesicles). Some of this models were derived to ultimately depict the mechanical properties of the red blood cell membrane (see Appendix A). We recall that the rbc is characterized by a nontrivial coupling between a cytoskeleton that provides to the cell a resistance to both stretch and shear deformation, and a bilayer lipid membrane that provide a bending resistance (but no shear resistance).
In 1963 Brånemark and Lindström reported that rbcs recover from mechanical deformations within a fraction of a second after emerging from the microcirculation, and resume their biconcave shape again [Branemark 1963]. In 1970 Canham used this indication to draw the assumption that the biconcave shape requires the least energy to be maintained. Using Cassini ovals, he first showed that constraining the area and the volume to constant values (*e.g.* typical values of a rbc) is not sufficient to obtain the biconcave shape, thus the membrane is responsible for the rbc shape. Indeed, Fung and Tong 1968 pinpointed that the rbc can be deformed to an infinite number of shapes without tearing or stretching and without change of the enclosed volume, owing this to the small value of the pressure differential across the membrane at equilibrium [Fung 1968]. Canham considered each monolayer as

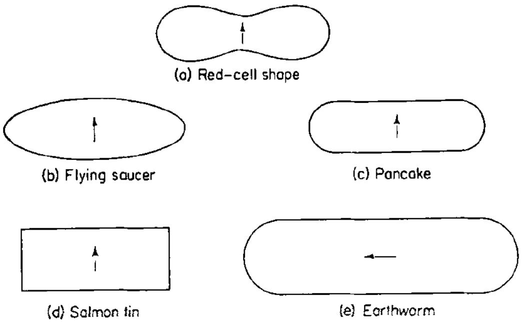

Figure 3.1: Different shapes with the same area and volume. The earthworm shape appears disproportional because of the inability to project a plane view into three dimensions. Courtesy from [Canham 1970]

an isotropic material that can resist temporarily to distortion (shearing or bending) without area changes, but the two monolayers as a membrane are anisotropic, thus no transfer of material between the two isotropic monolayers is permitted, that is not in agreement with the fluid nature of the membrane. The process of change of lipid molecules from one side of the bilayer to the other for closed phospholipids membranes turns out to be slow, in the order of hours [Homan 1988] whereas the time scale of the flip-flop exchange process is still unknown for the case of rbcs. The second assumption stated that the biconcave shape of the rbc corresponds to the minimum of elastic energy stored in the membrane. The stored elastic energy was assumed to be zero for a flat element of membrane and different from zero for a curved element of membrane. The third assumption said that the bilayer is impermeable, and the area of the membrane is conserved. And last but not least,

the membrane is supposed to have the same physical properties over the entire surface. This last assumption does not make unanimity and is in contradiction with some previous studies, among whom we cite [Fung 1968].
Based on a set of experimental measurements in [Canham 1968], the volume and the area of 23 rbcs were selected. For each cell, a family of shapes with the same volume and area was generated using a modified equation of Cassini ovals (3.34)

$$Y(x) = B[(C^4 + 4A^2x^2)^{0.5} - A^2 - x^2]^{0.5} \tag{3.34}$$

where B is a dimensionless parameter that allows to vary the shape, A and C are two constants with unit of length. By computing the bending energy using the equation (3.35)

$$\mathscr{H} = \oint \frac{\kappa}{2}(c_1 + c_2)^2 dA \tag{3.35}$$

where dA is the area element, c_1 and c_2 are the two principal curvatures, and κ is the bending stiffness. Canham showed that in each family, the member with the minimum value of the bending energy was the biconcave shape.
Although some of the hypothesis of Canham remained unproven, the shapes predicted by the bending energy model are indeed in a good agreement with the unstressed shape of a human rbc (see Fig.3.2).

A theory based on electrostatic energy density contained within the rbc surface was proposed by Adams 1973 in [Adams 1973] to explain the biconcave shape, and then compared to the minimum bending energy model introduced by Canham in 1970 [Canham 1970]. Although Adams provided an energy functional for the shape of the rbc, the exact solution could not be reached due to mathematical complexities. He rather showed that the minimum bending energy of the membrane leading to the biconcave shape of the rbc corresponded also to the minimum of the total electrostatic energy. Adams questioned the validity of the assumptions of Canham, and argued that most biological membranes are not an isotropic linearly elastic material and therefor the use of the surface integral of the sum of squares of the principal curvatures (minimum bending energy equation) is not justified.

Helfrich 1973 introduced a new parameter,the spontaneous curvature (called also the Helfrich spontaneous curvature), which describes the asymmetry of the two monolayers of the fluid membrane, and derived a free energy for a closed bilayer membrane (vesicle) reading in its general form as

$$\mathscr{H} = \oint \{\frac{\kappa}{2}(c_1 + c_2 - c_0)^2 + \kappa_G(c_1c_2)\}dA + \Delta P \int dV + \zeta \oint dA \tag{3.36}$$

where $c_1 = 1/R_1$ and $c_2 = 1/R_2$ are the principal curvatures, c_0 is the spontaneous curvature, κ and κ_G are the bending and the Gaussian curvature moduli [Helfrich 1973]. The first integral in the RSH represents the total elastic energy stored in the membrane (free energy associated with bending deformations on the surface). The second integral $\Delta P \int dV$ expresses the free energy associated to volume deformations induced by osmotic pressure differences between the inside and

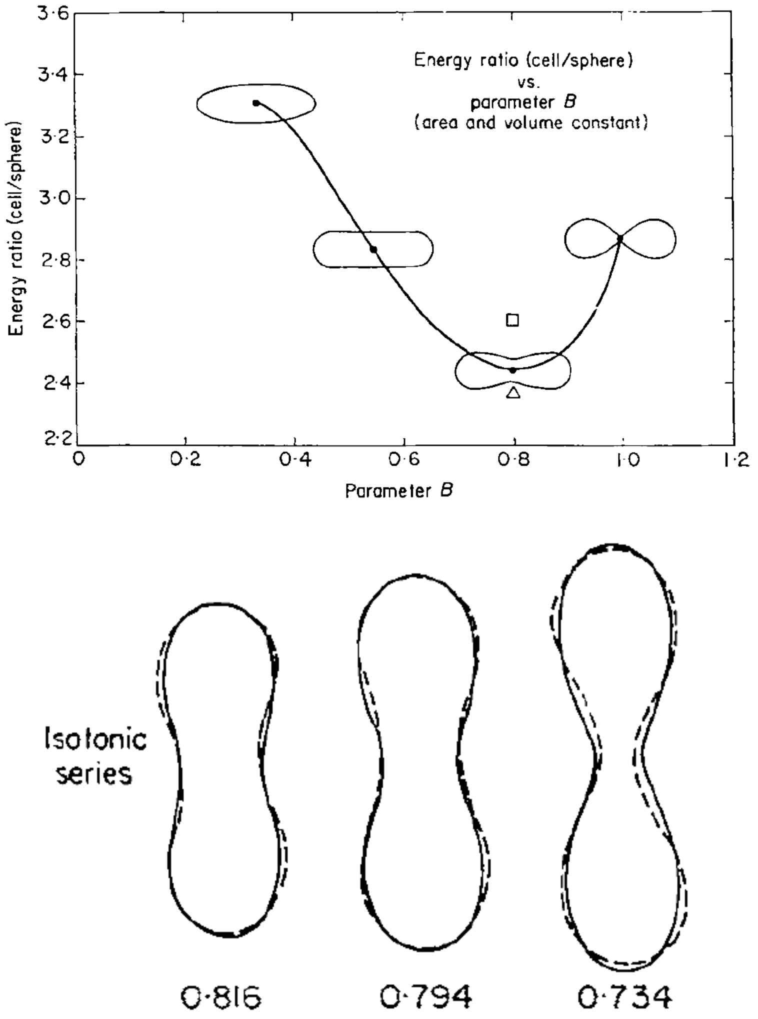

Figure 3.2: Equilibrium shapes obtained by minimizing the bending energy. Top: Members from the same family (same volume and area). The biconcave shape requires the least energy to be maintained. Bottom: Members from different families. Comparison between predicted (straight line) and observed (dashed lines) shapes. The numbers below each shape correspond to the sphericity index defined as $4.84V^{\frac{2}{3}}/A$ where V is the cell's volume and A its area. Courtesy from [Canham 1970].

the outside of the cell. The third integral accounts for the free energy associated to deformations induced by surface or other interfacial tensions. ΔP and ζ can both be seen as two Lagrange multiplier to constrain volume and area to fixed values. The total elastic bending energy can therefor be written in the most simplified form as the addition of two contributions, the mean and the Gaussian curvatures

$$\mathcal{H} = \frac{\kappa}{2} \oint (c_1 + c_2 - c_0)^2 dA + \kappa_G \oint c_1 c_2 dA \tag{3.37}$$

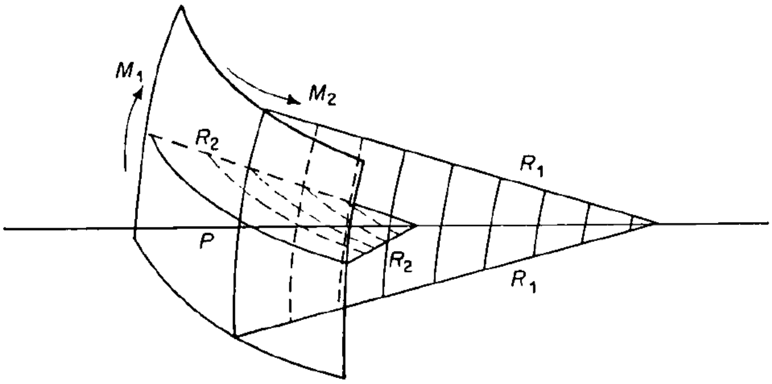

Figure 3.3: Sketch of the bending of an element of membrane. R_1 and R_2 are the principal radii of curvature. Courtesy from [Canham 1970].

where the area and volume constraints (or perimeter and area in two dimensions) can be added separately in the form of two Lagrange multipliers. The spontaneous curvature corresponds to the value of the mean curvature for an unstressed membrane. By considering only symmetrical membranes, this term can be disregarded (*i.e.* $c_0 = 0$). The mean curvature ($(c_1 + c_2)/2$) is expressed in a quadratic form to underline the non dependency of the elastic energy from the sign of the mean curvature. The Gaussian curvature is a topological invariant owing to the Gauss-Bonnet theorem. In two dimensions, this term is an irrelevant constant owing to the property $\oint cds = \oint \frac{d\theta}{ds}ds = 2\pi$.

Helfrich formulation has the convenience to use local Cartesian coordinates on the membrane. Considering the z axis as parallel to the surface normal vector $\mathbf{n}(x, y)$ on each membrane's node, the principal curvatures can be defined in term of the eigenvalues of the following matrix

$$M_H = \begin{bmatrix} \frac{\partial n_x}{\partial x} & \frac{\partial n_x}{\partial y} \\ \frac{\partial n_y}{\partial x} & \frac{\partial n_y}{\partial y} \end{bmatrix} \tag{3.38}$$

By recalling that $\mathbf{n}$ is normal to a uniquely defined surface[1], the mixed derivatives must then vanish ($\nabla \times \mathbf{n} = \mathbf{0}$), and the principal curvatures are expressed as

$$c_x = \frac{\partial n_x}{\partial x}, \qquad c_y = \frac{\partial n_y}{\partial y} \tag{3.39}$$

Taking advantage from the rotational symmetry of the membrane, only the combinations of derivatives of $\mathbf{n}$ that are independent of the orientation of the x and y axes appear in the expression of the total curvature elastic energy which can be

---

[1] We consider that the membrane constitutes an orientable surface with a normal vector pointing outward.

rewritten as

$$\mathscr{H} = \frac{\kappa}{2}\oint (tr(M_H) - c_0)^2 dA + \kappa_G \oint det(M_H) dA \tag{3.40}$$

where $tr(M_H)$ and $det(M_H)$ are the trace and the determinant of the matrix M_H.

For our problem, we will consider the following basic assumptions:

1. We assume that membrane is an infinitely thin closed bilayer (a one dimensional contour), encapsulating an inner fluid and suspended in an outer fluid.

2. The membrane is assumed to be symmetric (*i.e.* $c_0 = 0$).

3. The membrane is impermeable, therefor the area (volume in three dimensions) must be conserved. This condition is satisfied implicitly by the Green function. However, accumulative numerical errors at large times might induce a change in the area. Thus we need to use a Lagrange multiplier to ensure the conservation of the area.

4. The membrane should be inextensible. Condition that must be satisfied by using a Lagrange multiplier[2] to constrain the perimeter (area in three dimensions).

The load exerted by the two dimensional membrane on the fluid is obtained from the functional derivative[3] of the total curvature elastic energy 3.36, which reads in two dimensions as

$$\mathbf{f}_{struct\mapsto fluid} = -\frac{\delta \mathscr{H}}{\delta \mathbf{X}} = \kappa[\frac{\partial^2 c}{\partial s^2} + \frac{c^3}{2}]\mathbf{n} - c\zeta\mathbf{n} + \frac{\partial \zeta}{\partial s}\mathbf{t} \tag{3.41}$$

where ∂s is the arclength, $\mathbf{n}$ and $\mathbf{t}$ are namely the outward normal and the tangent unit vectors at a position vector $\mathbf{X}$ belonging to the membrane, and ζ is a Lagrange multiplier fulfilling the constraint of area and perimeter conservations. We introduce the following dimensionless quantities:

$$c^* = cL, \quad \zeta^* = \zeta L^2/\kappa_c, \quad s^* = s/L, \quad \mathbf{u}^* = \mathbf{u}T_c/L, \quad \mu_1^* = \mu_1/\mu_c, \quad \kappa^* = \kappa/\kappa_c$$

, and substitute (3.41) in (3.32), and write the subsequent boundary equation in a dimensionless form

$$u_k^*(\mathbf{X_0}) = \frac{2}{(1+\lambda)}u_k^{\infty *}(\mathbf{X_0}) + \frac{1}{2\pi\mu_1^*(1+\lambda)}\int_{\partial\Omega} G_{ik}^*(\mathbf{X},\mathbf{X_0}) f^*_{struct\mapsto fluid,i}(\mathbf{X})dl^* + \frac{(1-\lambda)}{2\pi(1+\lambda)}\int_{\partial\Omega}^{PV} u_i^*(\mathbf{X})T_{ijk}^*(\mathbf{X},\mathbf{X_0})n_j(\mathbf{X})dl^* \tag{3.42}$$

---

[2] The conservation of perimeter and area will be discussed later on in this chapter

[3] Details of the derivation can be found in the Appendix A of the PhD thesis of B. Kaoui (2009) [Kaoui 2009a].

where the stress jump across the membrane reads as

$$\mathbf{f}^*_{struct\mapsto fluid} = \frac{1}{C_a}\{\kappa^*[\frac{\partial^2 c^*}{\partial s^{*2}} + \frac{c^{*3}}{2}]\mathbf{n} - c^*\zeta^*\mathbf{n} + \frac{\partial \zeta^*}{\partial s^*}\mathbf{t}\} \tag{3.43}$$

We now introduce three dimensionless numbers that will be used hereafter to describe and study our system:

1. The capillary number $C_a = \frac{\mu_c L^3 \dot{\gamma}}{\kappa_c} = \frac{\tau_c}{T_c}$, which appears in the RHS of (3.43); describes the resistance of the membrane to the external flow. It represents as well the ratio between the characteristic shape relaxation time $\tau_c = \frac{\mu_c L^3}{\kappa_c}$ and the time scale of the flow $T_c = 1/\dot{\gamma}$, where $\dot{\gamma}$ is the shear rate.

2. A second dimensionless number $\lambda = \mu_2/\mu_1$ defines the viscosity ratio between the inner and the outer fluids.

3. A third dimensionless number $C_n = 2R_0/W$, describing the degree of confinement and reading as the ratio between the diameter of the cell and the width of the channel.

4. The fourth dimensionless number, the reduced area (ν), is the ratio between the actual fluid area enclosed by the vesicle contour ($S = \pi R_0^2$) and the area of a disk having the same perimeter as the vesicle. For a rbc, the reduced area is $\nu = 0.65$.
   The effective radius of the cell ($R_0 \equiv \sqrt{S/\pi}$), and the outer viscosity ($\mu_1 = \mu_c$) are chosen to be the characteristic length and viscosity scales, respectively. κ_c is the characteristic membrane rigidity. Time will be measured hereafter in unit of τ_c and distances in unit of R_0. To avoid overload notations in oncoming formulas, we will consider in the following unstarred variables as scaled. Unscaled variables will be expressed in real units.

At this level, we have developed a tool to study the flow of vesicles in an unbounded flow, as well as the morphology of vesicles in a static fluid (see Fig. 3.4). The next step will be to add the contribution of rigid walls to the problem.

3.4 Numerical procedure

Our problem reads as

$$\frac{d\mathbf{X}}{dt} = \mathbf{u}(\mathbf{f}_{mem}(\mathbf{X})) \tag{3.44}$$

where $\mathbf{f}_{mem} = \mathbf{f}_{struct\mapsto fluid}$, and $\mathbf{X}$ is a position vector lying on the interface. The interface can be simply regarded as a collection of Lagrangian nodes advected by the flow. In order to determine the advection velocity and thus the new position of the nodes, we need to compute the force exerted by the membrane on the fluid. Once

Figure 3.4: Shape transformation of a vesicle as a function of the reduced area in a static fluid computed using 3.42.

it is done, the velocity of each membrane's discretization points can be deduced, and the position of each node is updated in time using an explicit Euler scheme.

$$\mathbf{X}(t+dt) = \mathbf{X}(t) + \mathbf{u}(\mathbf{X}(t), t)dt \tag{3.45}$$

The advected membrane is a two dimensional incompressible fluid that can deform when subject to external stresses. Therefor, to fulfill the incompressibility condition, an evolution equation coupling the local curvature of each discretization node of the membrane with its normal and tangential velocities must be satisfied to keep the distance between two neighboring nodes constant during time. This may be achieved by the use of a special gauge, introduced in [Csahók 1999] to study fronts dynamics, and used in [Cantat 2003] to constrain the local arclength conservation of a two dimensional vesicle[4]; reading as

$$u_n c + \frac{\partial u_t}{\partial s} = 0 \tag{3.46}$$

where s is the curvilinear abscissa and ∂s is the arclength. This gauge is the counterpart of the continuity equation along the membrane ($\mathbf{t} \cdot \frac{\partial \mathbf{u}}{\partial s} = 0$). The incompressibility of the membrane (conservation of area and perimeter) implies the use of a Lagrange multiplier. This approach in addition from being computationally costly, shows some numerical instabilities for our problem as discussed in G. Ghigliotti PhD thesis [Ghigliotti 2010a, p. 46]. Therefor a tension-like parameter is introduced as a penalty instead of the Lagrange multiplier accounting for both tangential ($\frac{\partial \zeta}{\partial s}\mathbf{t}$) and normal ($-c\zeta\mathbf{n}$) membrane incompressibility, then substituting this in 3.41 gives

$$\mathbf{f}_{struct \mapsto fluid} = \kappa[\frac{\partial^2 c}{\partial s^2} + \frac{c^3}{2}]\mathbf{n} + K_{tens}[(\ell_m - \ell_0)\mathbf{t}_m + (\ell_p - \ell_0)\mathbf{t}_p] \tag{3.47}$$

where K_{tens} is a tension-like parameter, ℓ_m and ℓ_p are the lengths of namely the segment $X_{i-1}X_i$ and X_iX_{i+1}. $(\ell_m - \ell_0)$ and $(\ell_p - \ell_0)$ represent the change of lengths of the segments $X_{i-1}X_i$ and X_iX_{i+1} with respect to the reference length ℓ_0. $\mathbf{t}_m$ and $\mathbf{t}_p$ are the tangent unit vectors originating from the node X_i and pointing in the direction of the nodes X_{i-1} and X_{i+1} respectively. The tension-like parameter should be taken large enough to fulfill the perimeter conservation (for details see Refs. [Kaoui 2009a, p. 43] and [Ghigliotti 2010a, p. 46]). The use of a penalty-like function implies choosing a relatively small time step. Indeed, at each time step the eventual deviation of the perimeter and the reduced area from their initial values is corrected. Recall that the cell is characterized by a reduced area $\nu = \sqrt{S/[\pi(p(2\pi))]^2}$, where S and p are the surface and the perimeter of the cell. Constraining the perimeter and the reduced area will ensure a constant area over time, and therefor fulfilling the quasi-incompressibility of the membrane. [5]In a 3D system, the local membrane incompressibility can also be expressed using a spring-like potential ensuring a local conservation of the area. Nevertheless the spring-like potential alone is not working well, since the membrane can be subject to high stresses in some cases. A feedback loop on the reduced volume is used as a complement to avoid variations of the volume and area. In addition,

---

[4] A demonstration of the constraint equation can be found in Ref. [Cantat 1999a, p. 124]

[5] In this thesis, all the simulations were performed in 2D.

the membrane is remeshed periodically to suppress mesh entanglements. A major drawback of the spring-like potential model is that the numerical control parameters have to be fixed manually according to the problem investigated. A detailed description of the numerical scheme can be found in [Biben 2011].
The main steps of the algorithm can be summarized as:

1. Generating an initial shape or starting from a previous one.
2. Computing the tangent and normal unit vectors, and then the local curvature on each node.
3. Deducing the bending and tension-like forces using (3.47).
4. Computing the velocity on each node using (3.42). Once at this step, the task is to evaluate the product of a dense Matrix-Vector. The size of the Matrices (Green's functions) is $N \times N$ and the one of the vectors (velocity, force, normal and tangent unit vectors) is N, where $N = N_{mem} \times N_V$, N_{mem} is the number of nodes of the interface, and N_V the total number of interfaces.
5. Updating the nodes position via the advection scheme (Eulerian explicit scheme), and then going back to step 2.

The Green's functions are known to have a slow spatial decay leading to dense matrix-vector products ($\mathbf{Gf}_{mem}$ and $\mathbf{Tu}$). The size of the matrices depends on the number of discretization nodes, and can become easily cumbersome in case of many particle problems. Moreover, a problem involving boundaries will require the discretization of the walls leading to even larges matrices, that will need to be inversed at each time step in order to determine the walls' force that will satisfy the no-slip velocity. To overcome this difficulties, different approaches exist in the literature. The particle mesh Ewald (PME) proposes to decompose the Green's functions into a short and smooth parts, reducing the computation cost from $\mathcal{O}(N^2)$ to $\mathcal{O}(N \log N)$ [Zhao 2010]. The second approach consists to tackle the matrix-vector product, and uses a fast evaluation technique like the fast multipole method (FMM), that can reduce the computation cost to $\mathcal{O}(N)$ [Selmi 2011]. An alternative, that can be combined with the PME or the FMM consists in deriving the specific Green's functions for the considered boundary problem that will satisfy intrinsically the no-slip condition on the walls.

3.4.1 Image method for a flow confined between two parallel flat walls

First we consider the flow in an unbounded domain due to a Stokeslet with a given strength F located at $\mathbf{X_0}(x_0, y_0)$), and recalling the two dimensional Oseen tensor

$$G_{ik}(\mathbf{X}, \mathbf{X_0}) = -\delta_{ik} \ln r_0 + \frac{r_{0,i} r_{0,k}}{r_0^2} \tag{3.48}$$

where $\mathbf{r}_0 = \mathbf{X} - \mathbf{X}_0$, and $r_0 = |\mathbf{r}_0|$. Then we introduce the notations used in the Fig.3.5, where $r_n = |\mathbf{r}_n|$, and $R_n = |\mathbf{R}_n|$. The vectors $\mathbf{r}_n$ and $\mathbf{R}_n$ are defined as $\mathbf{r_n} = (x - x_0, y - y_0 - 2nW)$ and $\mathbf{R_n} = (x - x_0, y + y_0 + W - 2nW)$.
Considering the sum over all the reflections of the Stokeslet with respect to the two walls, we obtain

$$G^F_{ik}(\mathbf{X}, \mathbf{X_0}) = \sum_{n=-\infty}^{+\infty} -\delta_{ik} \ln r_n + \frac{r_{n,i} r_{n,k}}{r_n^2} - \sum_{n=-\infty}^{+\infty} -\delta_{ik} \ln R_n + \frac{R_{n,i} R_{n,k}}{R_n^2} \tag{3.49}$$

The first term in the RHS of 3.49 represents the sum of the point force and its images that have the same strength. Whereas the second term corresponds to the sum of images of the point force with the same strength but with an opposite sign. Unfortunately an infinite set of reflections is not enough to satisfy the desired boundary conditions. Indeed the distance from one of the walls; denoted h and sketched as the distance from the lower wall in Fig.3.5), appears implicitly[6] in our Green's function $\mathbf{G}^F$. To demonstrate that only the diagonal components of the fundamental Green's function vanish at the wall, we need to evaluate 3.49 at the boundaries. The two series diverge when n tends to infinity. This problem can be bypassed by using a special summation formula to obtain a regular expression of $\sum\limits_{n=-\infty}^{+\infty} \ln r_n$ as reported in [Lamb 1945, p. 68]. Next we write

$$\sum_{n=-\infty}^{+\infty} \ln r_n = \frac{1}{2} \ln\left(\cosh\left(x - x_0\right) - \cos\left(y - y_0\right)\right) + \frac{1}{2} \ln 2 \tag{3.50}$$

where the term $\frac{1}{2} \ln 2$ was added so the Green's function near the source point reduces to a Stokeslet. This modification was introduced in [Pozrikidis 1992, p. 94]. The fundamental Green's function is then expressed as

$$\mathbf{G}^F(\mathbf{X}, \mathbf{X_0}) = \begin{bmatrix} \alpha_1(\mathbf{X}, \mathbf{X_0}) - \alpha_2(\mathbf{X}, \mathbf{X}_0^{IM}) & \beta_1(\mathbf{X}, \mathbf{X_0}) - \beta_2(\mathbf{X}, \mathbf{X}_0^{IM}) \\ \beta_1(\mathbf{X}, \mathbf{X_0}) - \beta_2(\mathbf{X}, \mathbf{X}_0^{IM}) & \gamma_1(\mathbf{X}, \mathbf{X_0}) - \gamma_2(\mathbf{X}, \mathbf{X}_0^{IM}) \end{bmatrix} \tag{3.51}$$

where

$$\alpha_1(\mathbf{X}, \mathbf{X_0}) = -\tfrac{1}{2} \ln\left[\cosh\left(\tfrac{\pi(x-x_0)}{W}\right) - \cos\left(\tfrac{\pi(y-y_0)}{W}\right)\right] + \tfrac{1}{2} \frac{\frac{\pi(x-x_0)}{W} \sinh\left(\frac{\pi(x-x_0)}{W}\right)}{\cosh\left(\frac{\pi(x-x_0)}{W}\right) - \cos\left(\frac{\pi(y-y_0)}{W}\right)} \tag{3.52}$$

$$\beta_1(\mathbf{X}, \mathbf{X_0}) = \tfrac{1}{2} \frac{\frac{\pi(x-x_0)}{W} \sin\left(\frac{\pi(y-y_0)}{W}\right)}{\cosh\left(\frac{\pi(x-x_0)}{W}\right) - \cos\left(\frac{\pi(y-y_0)}{W}\right)} \tag{3.53}$$

$$\gamma_1(\mathbf{X}, \mathbf{X_0}) = -\tfrac{1}{2} \ln\left[\cosh\left(\tfrac{\pi(x-x_0)}{W}\right) - \cos\left(\tfrac{\pi(y-y_0)}{W}\right)\right] - \tfrac{1}{2} \frac{\frac{\pi(x-x_0)}{W} \sinh\left(\frac{\pi(x-x_0)}{W}\right)}{\cosh\left(\frac{\pi(x-x_0)}{W}\right) - \cos\left(\frac{\pi(y-y_0)}{W}\right)} \tag{3.54}$$

$$\alpha_2(\mathbf{X}, \mathbf{X}_0^{IM}) = -\tfrac{1}{2} \ln\left[\cosh\left(\tfrac{\pi(x-x_0)}{W}\right) - \cos\left(\tfrac{\pi(y+y_0+W)}{W}\right)\right] + \tfrac{1}{2} \frac{\frac{\pi(x-x_0)}{W} \sinh\left(\frac{\pi(x-x_0)}{W}\right)}{\cosh\left(\frac{\pi(x-x_0)}{W}\right) - \cos\left(\frac{\pi(y+y_0+W)}{W}\right)} \tag{3.55}$$

$$\beta_2(\mathbf{X}, \mathbf{X}_0^{IM}) = \tfrac{1}{2} \frac{\frac{\pi(x-x_0)}{W} \sin\left(\frac{\pi(y+y_0+W)}{W}\right)}{\cosh\left(\frac{\pi(x-x_0)}{W}\right) - \cos\left(\frac{\pi(y+y_0+W)}{W}\right)} \tag{3.56}$$

$$\gamma_2(\mathbf{X}, \mathbf{X}_0^{IM}) = \tfrac{1}{2} \ln\left[\cosh\left(\tfrac{\pi(x-x_0)}{W}\right) - \cos\left(\tfrac{\pi(y+y_0+W)}{W}\right)\right] - \tfrac{1}{2} \frac{\frac{\pi(x-x_0)}{W} \sinh\left(\frac{\pi(x-x_0)}{W}\right)}{\cosh\left(\frac{\pi(x-x_0)}{W}\right) - \cos\left(\frac{\pi(y+y_0+W)}{W}\right)} \tag{3.57}$$

---

[6] $y_0 = h - W$ (see Fig. 3.5)

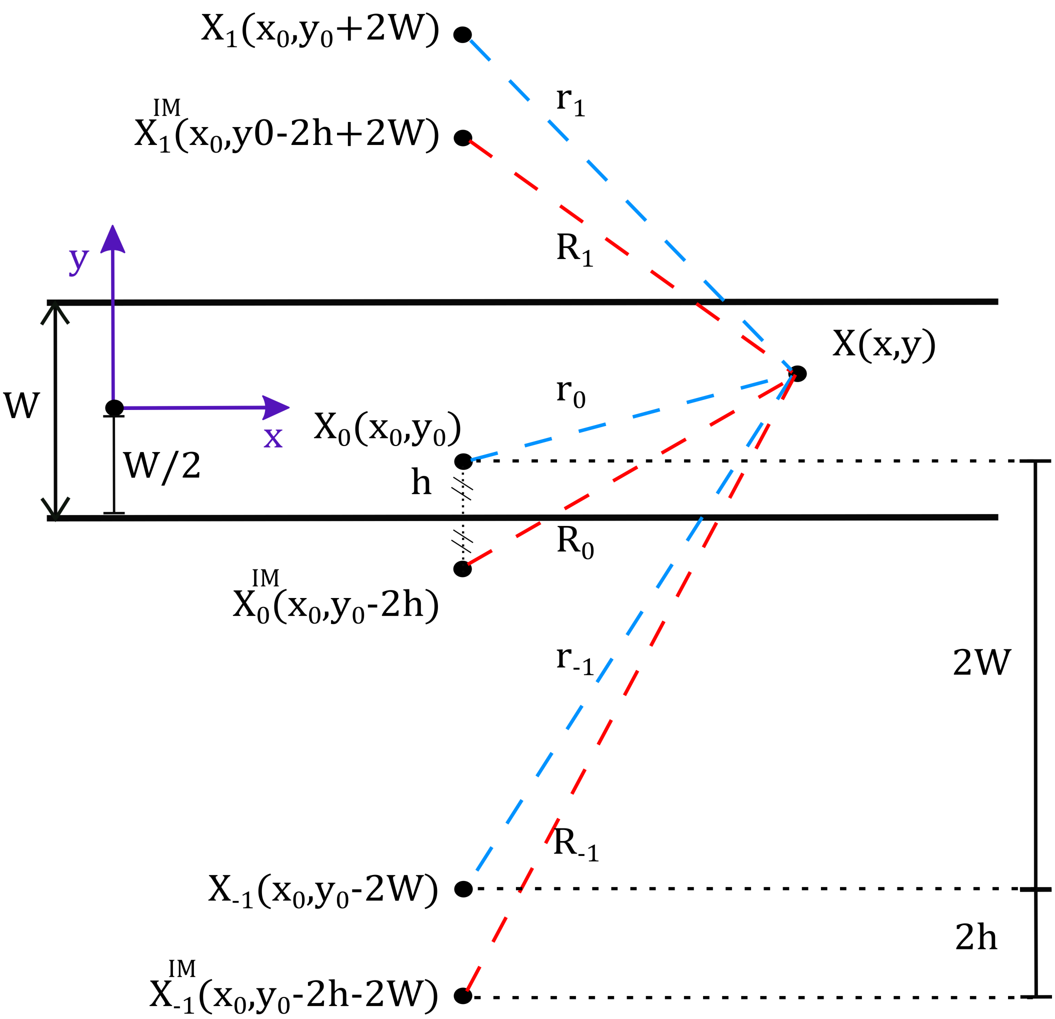

Figure 3.5: Sketch of a two dimensional Stokeslet in a confined geometry with its first few images, and other relevant vectors and notations for the description of the image technique leading to the computation of the specific Green's function accounting for two parallel walls. The point force is located at a distance $h = W/2 + y_0$ from the lower wall $\mathbf{X}_0(x_0, y_0)$, and the origin of the coordinates is located on the center of the channel. The superscript IM stands for the image of the source point $\mathbf{X}_0(x_0, y_0)$ with respect to the lower wall and then the network of reflections of this image $\mathbf{X}_0^{IM}(x_0, y_0)$.

At the boundaries ($y = \pm W/2$), we find that only the diagonal elements vanish.

$$\alpha_1(\hat{x}, \hat{y}^+) - \alpha_2(\hat{x}, \hat{y}^+_{IM}) = 0 \tag{3.58}$$

$$\alpha_1(\hat{x}, \hat{y}^-) - \alpha_2(\hat{x}, \hat{y}^-_{IM}) = 0 \tag{3.59}$$

$$\gamma_1(\hat{x}, \hat{y}^+) - \gamma_2(\hat{x}, \hat{y}^+_{IM}) = 0 \tag{3.60}$$

$$\gamma_1(\hat{x}, \hat{y}^-) - \gamma_2(\hat{x}, \hat{y}^-_{IM}) = 0 \tag{3.61}$$

$$\beta_1(\hat{x}, \hat{y}^+) - \beta_2(\hat{x}, \hat{y}^+_{IM}) = \frac{\frac{\pi\hat{x}}{W}\cos(\frac{\pi y_0}{W})}{\cosh(\frac{\pi\hat{x}}{W}) - \sin(\frac{\pi y_0}{W})} \tag{3.62}$$

$$\beta_1(\hat{x}, \hat{y}^-) - \beta_2(\hat{x}, \hat{y}^-_{IM}) = -\frac{\frac{\pi\hat{x}}{W}\cos(\frac{\pi y_0}{W})}{\cosh(\frac{\pi\hat{x}}{W}) + \sin(\frac{\pi y_0}{W})} \tag{3.63}$$

where $\hat{x} = x - x_0$, $\hat{y}^+ = W/2 - y_0$, $\hat{y}^- = -W/2 - y_0$, $\hat{y}^+_{IM} = W/2 + y_0 + W$, and $\hat{y}^-_{IM} = -W/2 + y_0 + W$.

Therefor we will have to add a counterpart to $\mathbf{G}^F$ in the form of an additional correction term that we will call the complementary component $\mathbf{G}^c$, in order to achieve the no-slip at the walls. $\mathbf{G}^c$ must satisfy the following boundary conditions on the walls:

$$G^c_{ii}(\hat{x}, \hat{y}^+) = G^c_{ii}(\hat{x}, \hat{y}^-) = 0 \tag{3.64}$$

$$G^c_{ik}(\hat{x}, \hat{y}^+) = -G^F_{ik}(\hat{x}, \hat{y}^+) \tag{3.65}$$

$$G^c_{ik}(\hat{x}, \hat{y}^-) = -G^F_{ik}(\hat{x}, \hat{y}^-) \tag{3.66}$$

The complementary Green's function is the solution of Stokes equations respecting the following boundary conditions on the walls 3.64, 3.65, and 3.66. For convenience, the solution is obtained in the Fourier space (see [Pozrikidis 1992, p. 98]) and the inverse Fourier transform is evaluated numerically using the inverse fast Fourier transform (IFFT) algorithm. The result is added to the expression given in 3.51 to obtain the desired Green's function.

Now that we have built our model, we can start studying the flow of RBCs in different situations. One of the advantage of the boundary integral method is that the external flow is decoupled from the disturbed velocity. In other words, it is relatively easy to switch from a shear flow to a Poiseuille flow or to a situation of a resting fluid. The code is validated by reproducing and completing a phase diagram of the motion of an isolated deformable vesicle past a confined channel with different confinement ratios and where the contribution of walls was implemented in a different way. We will discuss about this in the upcoming chapter (see chapter 4).

3.4.2 Alternative to the image technique

The boundary integral method with the proper Green's function constraining the boundary conditions provides us with a high accuracy tool to solve Stokes equations. Besides, the initial two dimensional problem can be reduced to a set of one dimensional integral equations over the boundaries which is quite convenient numerically. Moreover, the integration over the walls is not required since their contribution is included in the Green's function. The main drawback of this technique is that the geometry is fixed to parallel flat walls (in our case) and the boundary condition must be homogeneous everywhere on the walls (such as no-slip and impermeability). However it is always possible to model complicated geometries like the coaxial cylinders (Taylor-Couette) geometry [Ghigliotti 2011] or bifurcating channels [Calderon 2010], but at a certain price: a numerical discretization of the walls, additional integrals need to be calculated, and the no-slip velocity on the walls is not anymore explicitly satisfied. In contrary to the stress jump across the membrane, the force exerted by the walls on the fluid is unknown a priori, and its calculation can be done by a posteriori reasoning. In fact, this force acts as a spring force that tends to prevent the wall's nodes from being advected by the flow. The wall force is the solution of a dense linear system requiring the inversion of the free space Green's matrix for each node of the two walls. From our experience, this technique requests a significant number of discretization nodes, especially in the region where the cell is located. Another important point is the fact that the walls are quasi-rigid in the normal direction. This detail can be significantly important when the cell to tube diameter ratio is close to unity.

3.4.3 Time discretization

Since the computer does not understand the notion of continuous time, we need a way to discretize the time to N subdivisions. Again, several techniques exist to realize this task, such as backward and forward Euler schemes, and Runge-Kutta methods (explicit and implicit). Both classical Runge-Kutta method (RK4), and forward Euler scheme were tested. Since no differences in the outputs were observed, the more cost efficient method (the forward Euler scheme) was used. Basically we know the state (positions and velocities of the nodes) at the current time, and we want to jump to a later time. In a concrete manner, we know the positions of the nodes at a time t. Using this spatial informations, we have calculated the velocities at a time t following the procedure explained previously (see equation 3.42), and now we need to update the node's positions to the time $t + dt$.

$$\mathbf{X}(t + dt) = \mathbf{X}(t) + \mathbf{u}(\mathbf{X}, t)dt \tag{3.67}$$

The procedure is straightforward, once $\mathbf{X}(t + dt)$ is known, we can calculate $\mathbf{X}(t + 2dt)$ following the same scheme and so on.

CHAPTER 4

Dynamics and morphologies of a single vesicle in a confined Poiseuille flow

---

We have investigated the behavior of a single vesicle in a confined geometry under a Poiseuille flow. We have studied the effect of three parameters: i) the confinement, ii) the capillary number (strength of the flow), and iii) the viscosity contrast (ratio between the inner and outer fluids). Interestingly, the vesicles have shown a rich and complex dynamics, where transitions from a steady shape to chaos through a cascade of multiple periodic oscillations occurred by changing only one parameter. This motion actually can be assimilated to a flagella-like motion, where the vesicle via the tail, undergoes a periodic or a chaotic up-down motion. We performed a systematic scan in the three dimensional parameter space (λ, C_k, C_n), in order to explore the various intricate behaviors of a vesicle under a Poiseuille flow. In all simulations, we have set the reduced area ν to 0.6 which is close to the one of a RBC in 2D. The results are summarized in a phase diagram in the parameter plane (degree of confinement, flow strength). This finding highlights the level of complexity of a flowing vesicle in the small Reynolds number where the flow is laminar in the absence of vesicles and can be rendered turbulent due to elasticity of vesicles [Aouane 2014].

4.1 Introduction

Under a Poiseuille flow, the situation of interest in this chapter, it is known experimentally that RBCs exhibit a parachute as well a slipper shape [Skalak 1969, Schmid-Schönbein 1981, Abkarian 2008a, Tomaiuolo 2009].
Secomb and Skalak [Secomb 1982] have presented a model for the slipper shape based on a lubrication approximation. The slipper shape was also later observed in numerical simulations by Pozrikidis [Pozrikidis 2005b]. These authors used a capsule as a model for RBC. Capsules are shells made of polymers and are endowed with elastic properties, namely the shear elasticity that mimics the RBCs cytoskeleton, i.e. the spectrin network lying underneath the cell membrane. More recently, the minimal ingredients for the occurrence of a slipper shape were identified [Kaoui 2009b]: a two dimensional vesicle even in an unbounded Poiseuille flow exhibits a slipper solution when the flow strength is comparable to that in

the microvasculature. The slipper solution occurs as a result of loss of stability of the symmetric solution (called also parachute). These shapes were further investigated by including the effect of quasi-rigid bounding walls [Kaoui 2011b]. This study revealed large variety of shapes and dynamics such as the centered and off-centered periodic oscillations (called snaking). These oscillations are regular and stable in time. Subsequent study in 3D has also reported on similar phenomena [Fedosov 2014, Farutin 2014].

4.2 Description of the model

We consider the RBC in 2D as a vesicle: a closed deformable and non permeable membrane encapsulating an inner fluid and suspended in an outer fluid. The vesicle membrane withstands to bending but does not have a shear resistance, unlike RBCs, but they still share several dynamical properties with RBCs, like tank-treading and tumbling under linear shear flow, or parachute and slipper shapes under Poiseuille flow [Abkarian 2008b, Vlahovska 2009, Vlahovska 2013]. Moreover the stress free shape of a vesicle with the same surface-to-volume ratio as the RBC is a biconcave disk. The membrane total force is composed from a bending force, and a tension force to fulfill the area conservation constraint. The inner and outer fluids obey to Stokes equations. These equations are solved using the boundary integral formulation with the use of Green's function for two parallel walls, as described in chapter3. The external flow and confinement introduce two dimensionless numbers: the so-called capillary number (C_k) to quantify the flow strength over bending forces, and the confinement (C_n) to describe the ratio between the effective diameter of the vesicle and the width of the channel. The imposed Poiseuille flow is written as

$$\begin{cases} {u_x}^{\infty} &= u_0[1-(\frac{y}{W/2})^2] \\ {u_y}^{\infty} &= 0 \end{cases} \tag{4.1}$$

The capillary number is defined as

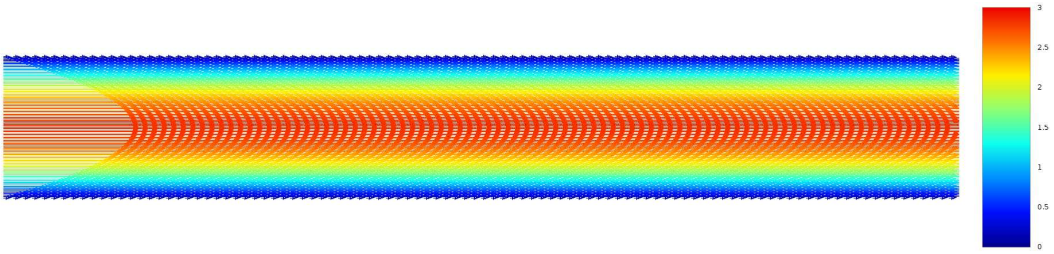

Figure 4.1: Profile of the imposed parabolic Poiseuille flow in absence of the cells. The colorbar codes for the magnitude of the velocity.

$$C_k = \frac{\eta_{out} R_0^4}{\kappa} \frac{u_0}{(W/2)^2} \equiv \tau_c \dot{\gamma} \tag{4.2}$$

and the confinement as

$$C_n = \frac{2R_0}{W} \tag{4.3}$$

where R_0, W and u_0 are the effective radius of the cell, the width of the channel and the maximum velocity of the unperturbed Poiseuille flow. We define the characteristic shear rate $\dot{\gamma}$ as the imposed velocity gradient evaluated at $y = R_0/2$, and it is equal to $R_0 u_0/(W/2)^2$, and $\tau_c = \eta_0 R_0^3/\kappa$ is the characteristic shape relaxation time. Time will be measured hereafter in unit of τ_c and distances in unit of R_0. In all simulations, we have set the reduced area τ to 0.6 which is close to the one of a RBC in 2D (see Fig. 3.4 and Fig. 3.2).

4.3 Results

The present study is a follow-up study to that of Kaoui et al. [Kaoui 2011b] and reveals a variety of new states. For example, we find that vesicles can first undergo snaking (periodic oscillation of the shape in the form of a snake motion) and suddenly undergo a new bifurcation showing period-doubling of the temporal oscillation upon variation of a control parameter (e.g. degree of confinement). On further variation of control parameter the system undergoes a subharmonic cascade oscillation before transiting to chaos. Other scenarios than period-doubling can also occur as we shall show. We investigate the occurrence of chaos using tools of dynamical systems. We present a full phase diagram in parameter space showing variety of dynamics (see Fig. 4.11).

4.3.1 Effect of flow strength and confinement on the shape of a vesicle with no viscosity contrast

We first set the viscosity contrast to $\lambda = 1$ and explored the effect of the confinement and the capillary number on the morphology of the cell. In order to test the new code based on the Green's function that vanishes at the wall [Thiébaud 2013], we have first confirmed the previously reported results [Kaoui 2011b, Tahiri 2013b], namely the existence of six different states: parachutelike shape, the confined and unconfined slipperlike shape, the centered and off-centered oscillating motion (called snaking in [Kaoui 2011b]) and peanut-like shape [Tahiri 2013b]). Fig. 4.3 shows the parachutelike and confined slipperlike solutions. The snaking motions (centered and non centered) recently reported by Kaoui et al. [Kaoui 2011b] and Tahiri et al. [Tahiri 2013b], have not exhausted all intricate dynamics. By investigating the evolution of solutions under close scrutiny we have discovered a variety of new states ranging from simple oscillations to complex multi-periodic oscillations, until chaotic motion prevails, as described below.

4.3.1.1 Transition to chaos via a subharmonic cascade

We have set $C_k W/R_0 = 5$ and varied the degree of confinement C_n. The results are shown in (Fig.4.4) where we represent the vertical position of vesicle center

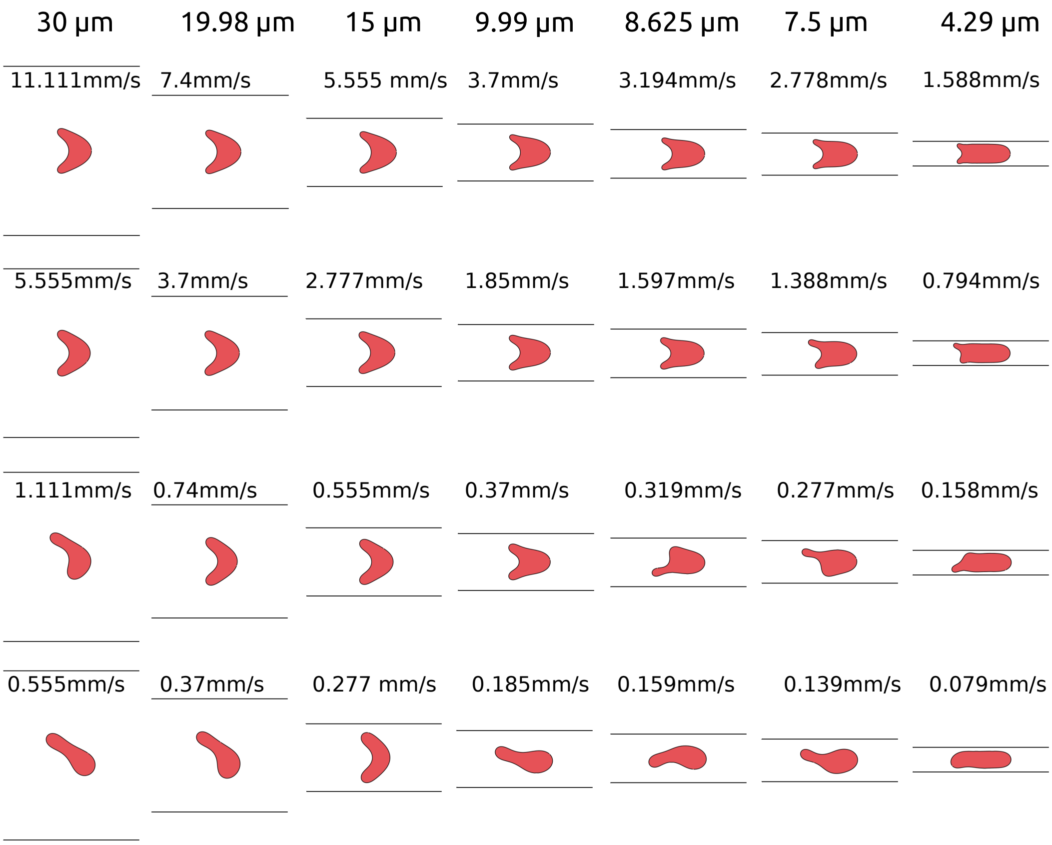

Figure 4.2: Different shapes exhibited by a vesicle subject to a Poiseuille flow. The slipper-like (asymmetric) and parachute-like (symmetric) shapes are observed. In addition, new dynamics are reported. The midplane velocity as well as the channel width are given in the figure.

of mass (y_{cm}) as a function of time. Below a first critical value of C_n, the slipper becomes unstable in favor of a snaking motion (off-centered). This is a Hopf bifurcation. Close to bifurcation point the temporal evolution of the amplitude of lateral excursion of center of mass (y_{cm}) remains constant over time (see Fig. 4.4b). By reducing further C_n the simple snaking solution undergoes a new bifurcation whereby the period of oscillation has doubled (Fig. 4.4c) and then quadrupled for a smaller value of C_n (Fig. 4.4d). By decreasing C_n further, dynamics enter a chaotic regime (Fig. 4.5).

In Fig. 4.6, we represent the amplitude A of excursion of center of mass in the y-direction (that is the absolute value of difference between two successive maxima). Since a slipper (as well as a parachute solution) moves along a line in the x-direction (cf. Fig.4.3) the amplitude of lateral excursion is zero above a critical value of $C_n = 0.75$ (Fig. 4.6). Fig. 4.6 shows the amplitude as a function of C_n, where we can see the beginning of a sub-harmonic cascade, and the signature of accumu-

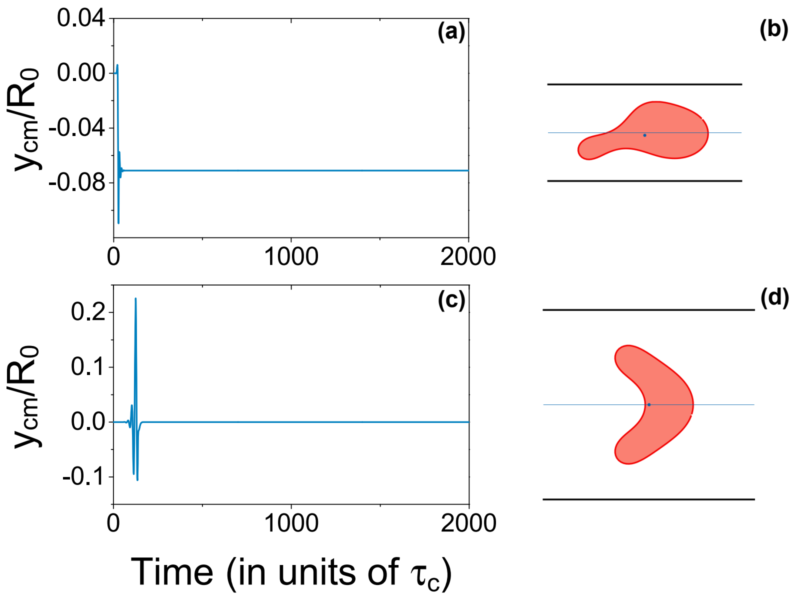

Figure 4.3: Stationary shape and history of the center of mass vertical position as a function of time: (a) and (b): slipper solution ($C_kW/R_0 = 6.25$ and $C_n = 0.8$); (c) and (d): parachute solution ($C_kW/R_0 = 6.25$ and $C_n = 0.44$). The x axis codes for the lateral position of the mass center y_{cm} of the cell scaled by the effective radius of the cell (R_0).

lation of bifurcation points. This is a universal behavior, as well documented in chaos textbooks [Schroeder 2012, Ott 2002, Bergé 1992]. The subharmonic cascade is one of the three generic scenarios of transition to chaos (the two others being intermittency and quasi-periodicity).

Here we have represented only the main oscillation (period 1), the period doubling (period 2) and quadrupling (period 4). Because of the universal accumulation in the sub-harmonic cascade (that is the location points of new bifurcations to higher order oscillations become closer and closer), the transition to period-8 and 16 for example requires tuning very carefully the control parameter as well as increasing numerical precision (a significant reduction of the numerical mesh size leads to excessive computation time) and it was not our aim to provide a very detailed analysis of the higher order period-doubling cascade. Starting from the regime of period-4 oscillation, we found that a quite small variation of C_n (of about 4%) leads to chaos, as shown in Fig. 4.5.

4.3.1.2 Transition to chaos via a period-tripling bifurcation

The subharmonic cascade is one of the three classical scenarios of transition to chaos (in addition to intermittency and quasi-periodicity). The sub-harmonic cascade corresponds to a cascade where at each bifurcation point the period is dou-

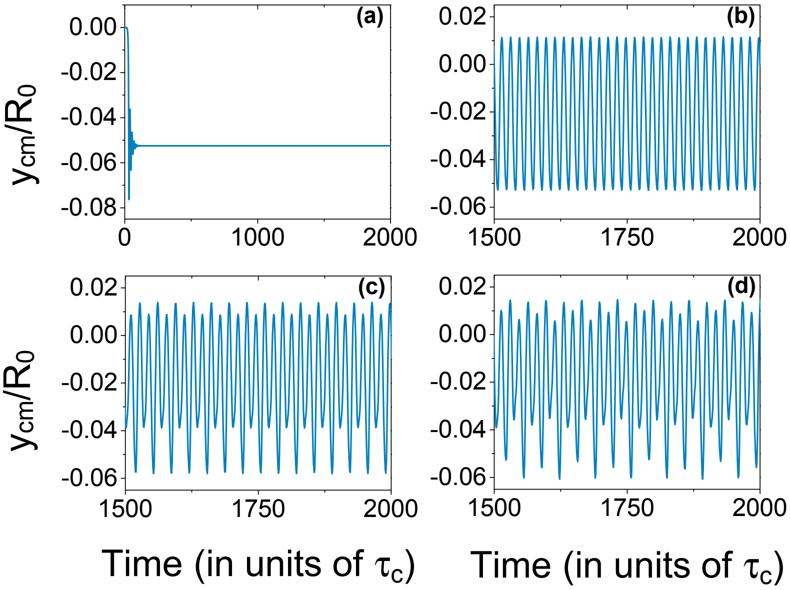

Figure 4.4: The center of mass vertical position as a function of time. (a) slipper solution ($C_k W/R_0$ = 5 and C_n = 0.769); (b) snaking ($C_k W/R_0$ = 5 and C_n = 0.733); (c) period-doubling ($C_k W/R_0$ = 5 and C_n = 0.729); and (d) period-quadrupling dynamics ($C_k W/R_0$ = 5 and C_n = 0.727).

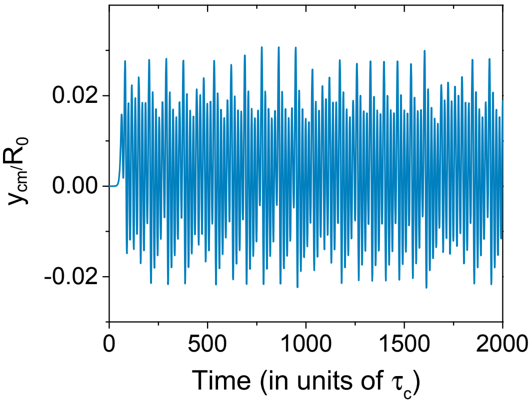

Figure 4.5: The center of mass vertical position as a function of time. An apparently chaos regime is found for $C_k W/R_0$ = 5 and C_n = 0.689.

bled (or the frequency is halved). By analyzing the dynamics of the initial snaking motion in other regions of parameter space, we have discovered that the snaking motion can also loose its stability in favor of a period-tripling bifurcation, which is a less known scenario as compared to the period doubling one. We show in Fig. 4.7 both a typical temporal signal and the bifurcation diagram.

Period-tripling bifurcations and more complex transitions were also reported in literature. We take as reference, for instance, the pioneering paper of Li and Yorke

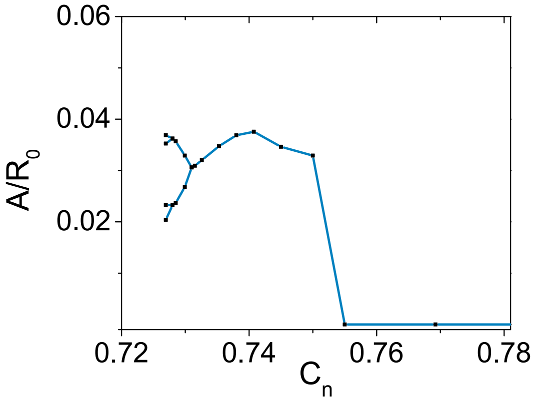

Figure 4.6: Period-doubling bifurcation diagram. The capillary number is fixed (C_kW/R_0 = 5), and only the confinement C_n is changed. The x and y axis stand for the confinement and the amplitude of the oscillations.

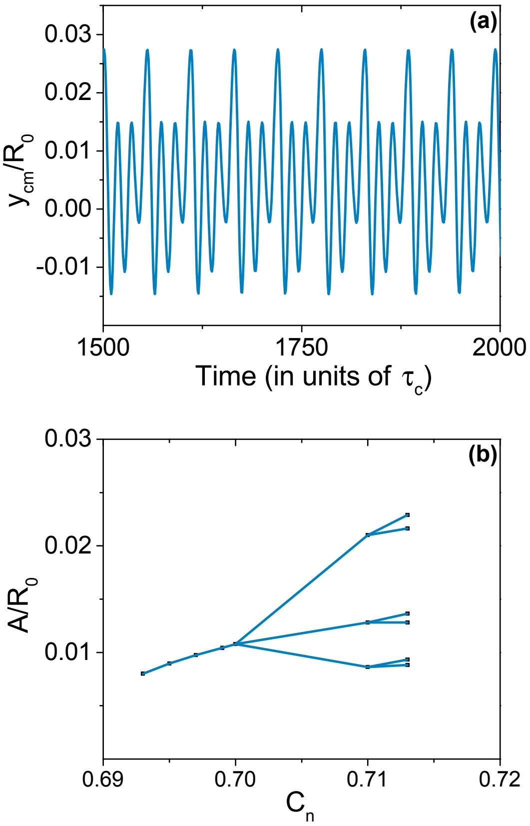

Figure 4.7: Period-tripling motion of the mass center. (a) temporal behavior for a period tripling dynamics (C_kW/R_0 = 4.611 and C_n = 0.71). (b) bifurcation diagram (C_kW/R_0 = 4.611).

[Li 1975] where they introduced the first mathematical definition of discrete chaos, showing the relation between the period three and chaos. Lui [Lui 2013] presented sufficient mathematical conditions for period-tripling and period-n bifurcations. Ze-Hui et al [Ze-Hui 2006] reported subharmonic bifurcations in a granular system, in the sequence of period-tripling, period-sextupling, and chaos. Zhusubaliyev and Mosekilde [Zhusubaliyev 2003] showed transition from periodic to chaotic oscillations through period-doubling, -tripling, -quadrupling, -quintupling, etc., bifurcations. They also discussed more complex transitions, from a family of cycle to another family of cycles with multiple periods.

4.3.1.3 Transition to Chaos:

In order to characterize chaotic dynamics we have performed a Poincaré map as well as Fourier transforms of the temporal evolution of center of mass amplitude. Fig. 4.8 displays the Poincaré sections relative to the different 1, 2, and 4 periodic

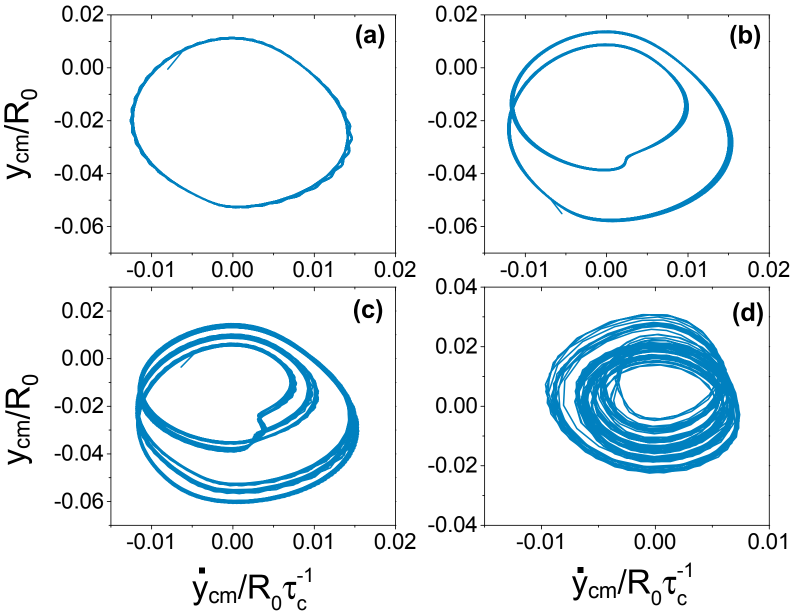

Figure 4.8: Poincaré sections of different oscillations observed by decreasing the confinement when the capillary number $C_k W/R_0$ has been fixed at 5. The y-axis stands for the y-component of the mass center of the cell and the x-axis for its derivative with respect to time. a)- $C_n = 0.733$. b)- $C_n = 0.729$. c)- $C_n = 0.727$. d)- $C_n = 0.689$.

oscillations, in addition to the chaotic one. In this case, the gradual decrease of the confinement under a low capillary number ($C_k W/R_0 = 5$ in these simulations) is responsible of the observed transitions. Snapshots of this motion are shown in Fig.4.9. Fig. 4.10 shows the Fourier spectrum of different dynamics. We see there the occurrence of the cascade until the transition to chaos.

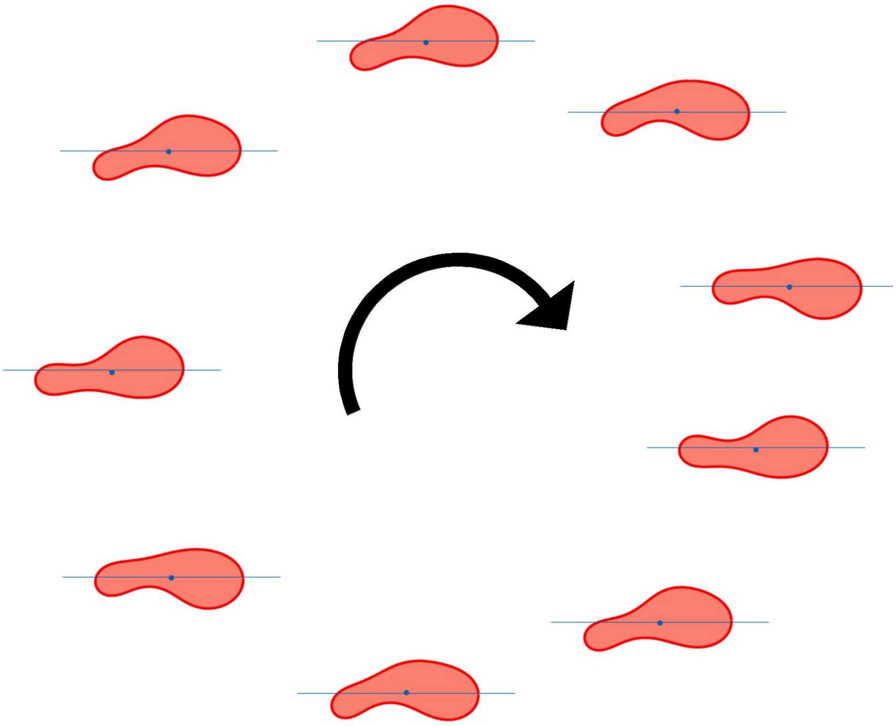

Figure 4.9: Snapshots of a cycle of period-doubling dynamics ($C_k W/R_0 = 5$ and $C_n = 0.729$). The cell seems to move like a spermatozoon, using its tail-like as a flagellum. The straight solid blue line indicates the centerline of the channel and the blue point codes for the mass center of the cell.

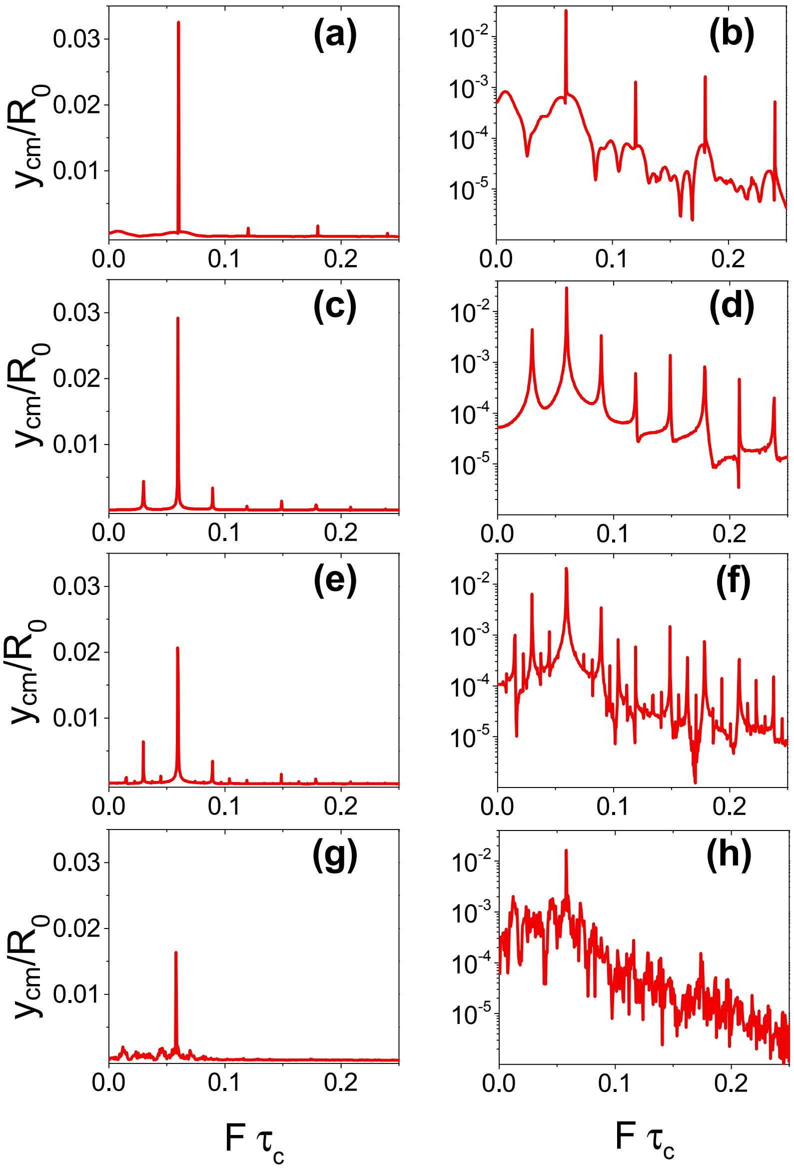

Figure 4.10: Fourier spectrum of different dynamics in linear (a), (c), (e), and (g) and semi-log (b), (d), (f), and (h) coordinates: **a** and **b** snaking ($C_k W/R_0$ = 5 and C_n = 0.733); **c** and **d** period-doubling ($C_k W/R_0$ = 5 and C_n = 0.729); **e** and **f** period-quadrupling ($C_k W/R_0$ = 5 and C_n = 0.727); and **g** and **h** chaotic dynamics ($C_k W/R_0$ = 5 and C_n = 0.689). The semi-log scale allows to see more easily the continuum spectrum characteristic of chaotic regimes. The x axis codes for the frequency F scaled by the characteristic time τ_c.

4.3.2 Phase diagram

We have performed a systematic analysis in order to determine the region of different dynamical manifestation going from order to chaos. The results are shown in Fig. 4.11. Besides the dynamics and shapes reported earlier [Kaoui 2011b, Tahiri 2013b], revealing slipper, parachute and snaking, we have identified here more complex dynamics, ranging from higher order oscillatory motion to chaos. Surprisingly enough, a simple situation treated here, namely a 2D vesicle under a Poiseuille flow, has revealed broadly 9 different kinds of motion (actually the number is even larger, since in Fig. 4.11 we do not specify the kind of multiple oscillation). This result highlights the complexity of this free boundary problem, where membrane elasticity that acting only via bending forces can here trigger rich dynamics.

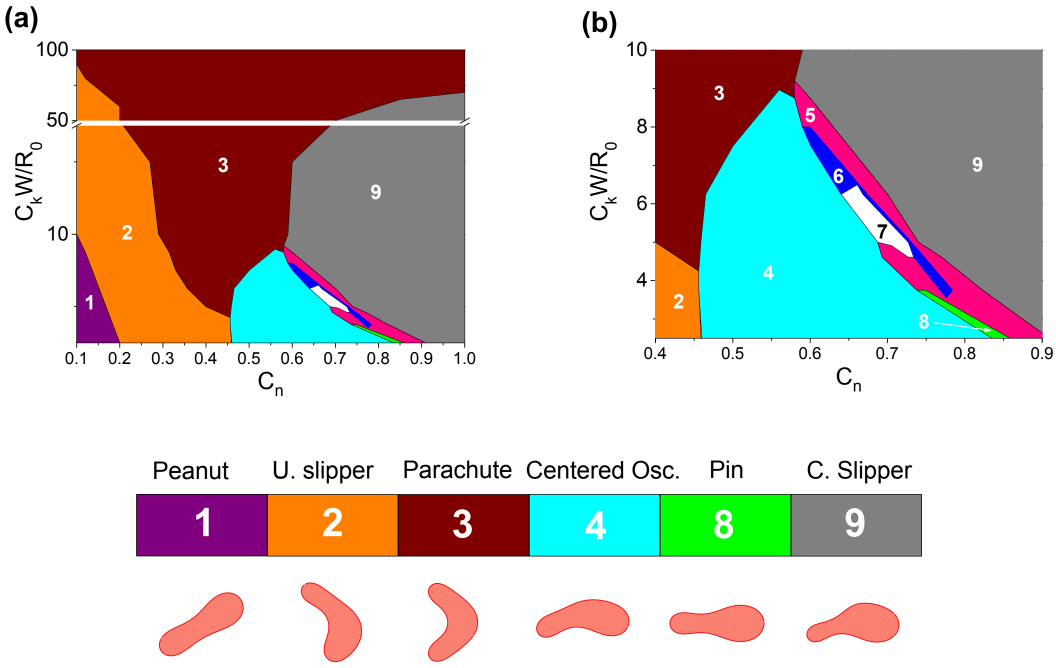

Figure 4.11: Phase diagram summarizing the different morphologies and dynamics of a single vesicle with a viscosity contrast set to unity ($\lambda = 1$). (a) overview of the phase diagram. (b) zoom on the region where oscillations occur. The combined effect of the confinement and flow strength leads to 9 distinct regions represented by different colors in the phase diagram: peanut-like shape (purple); unconfined slipperlike shape (orange); parachutelike shape (dark red); confined slipperlike shape (grey); centered oscillations (cyan); multiple periodic oscillations (dark blue); chaotic oscillations (white); off-centered oscillations (pink); and pin-like shape (green). Note that three regions are not represented in the legend namely: the multiple periodic, chaotic, and off-centered oscillations.

4.3.3 Benchmark

4.3.3.1 Spatial and Time discretizations

Figure 4.12: Stationary slipper-like shape computed for different values of the time and space discretizations. N_{mem} and dt denote respectively the number of discretization nodes and the time step. The capillary number and the confinement were fixed namely to $C_k = 10$ and $C_n = 0.23$.

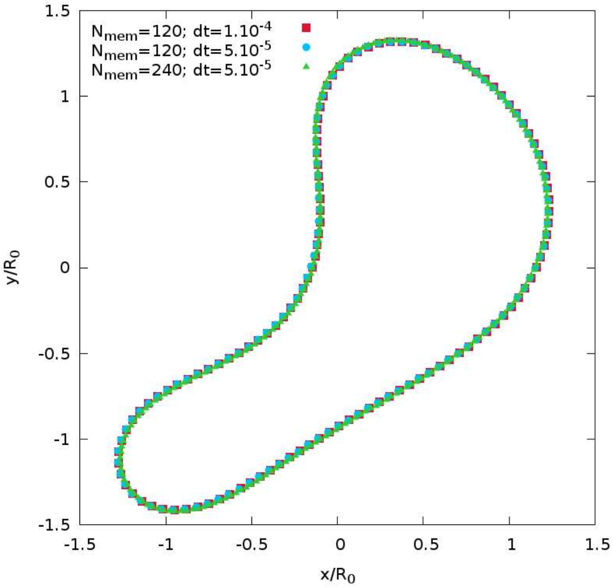

Figure 4.13: Stationary parachute-like shape computed for different values of the time and space discretizations. N_{mem} and dt denote respectively the number of discretization nodes and the time step. The capillary number and the confinement were fixed namely to $C_k = 10$ and $C_n = 0.40$.

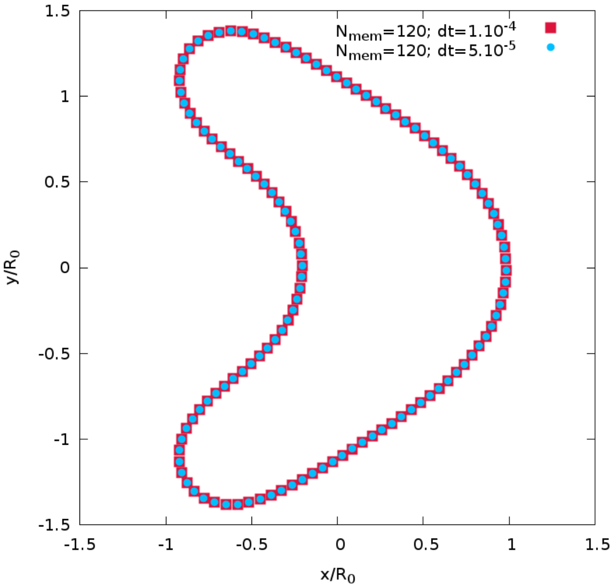

4.3.3.2 Initial Position and Shape

The figure 4.14 shows no dependency between the initial shape as well as initial position, and the oscillatory motion of the vesicle in the micro-channel. This mul-

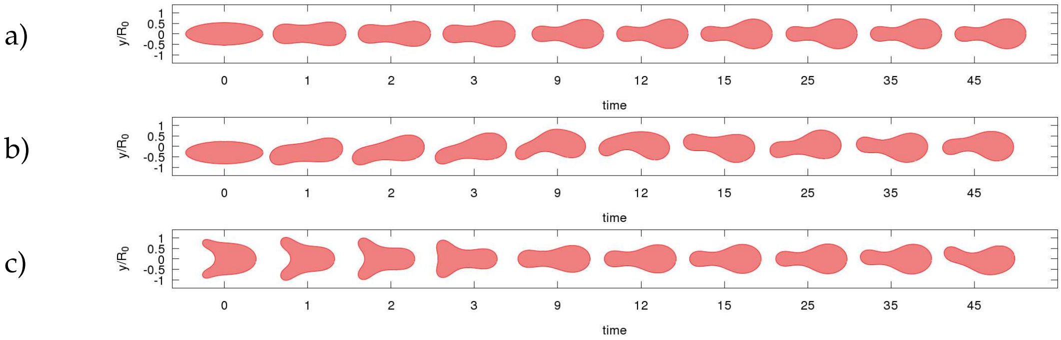

Figure 4.14: Shape evolution and lateral migration of a vesicle subject to a Poiseuille flow in a micro-channel for $C_\kappa = 4.836$, $C_n = 0.719$, $\tau = 0.6$ and $\lambda = 1$. The x-axis codes for the physical time and the y-axis for the position of the y-component of the mass center of the cell. The stationary solution is reached later and was not shown in these figures (see figure 4.15). The three simulations converge to the same solution, showing a multiple periodical oscillations (5-periodical). a)- the vesicle was set in the middle of the channel and initialized as an ellipse. b)- the vesicle was slightly shifted from the centerline of the channel. c)- the vesicle was initialized as a parachute and set in the middle of the channel.

tiple periodical oscillations persist also when changing the temporal and spatial discretizations. The history of the lateral migration of the y-component of the mass center is plotted in figure 4.15 and show clearly the existence of multiple periodical oscillations as stationary solution which, to our knowledge, was never reported in any theoretical or numerical study.

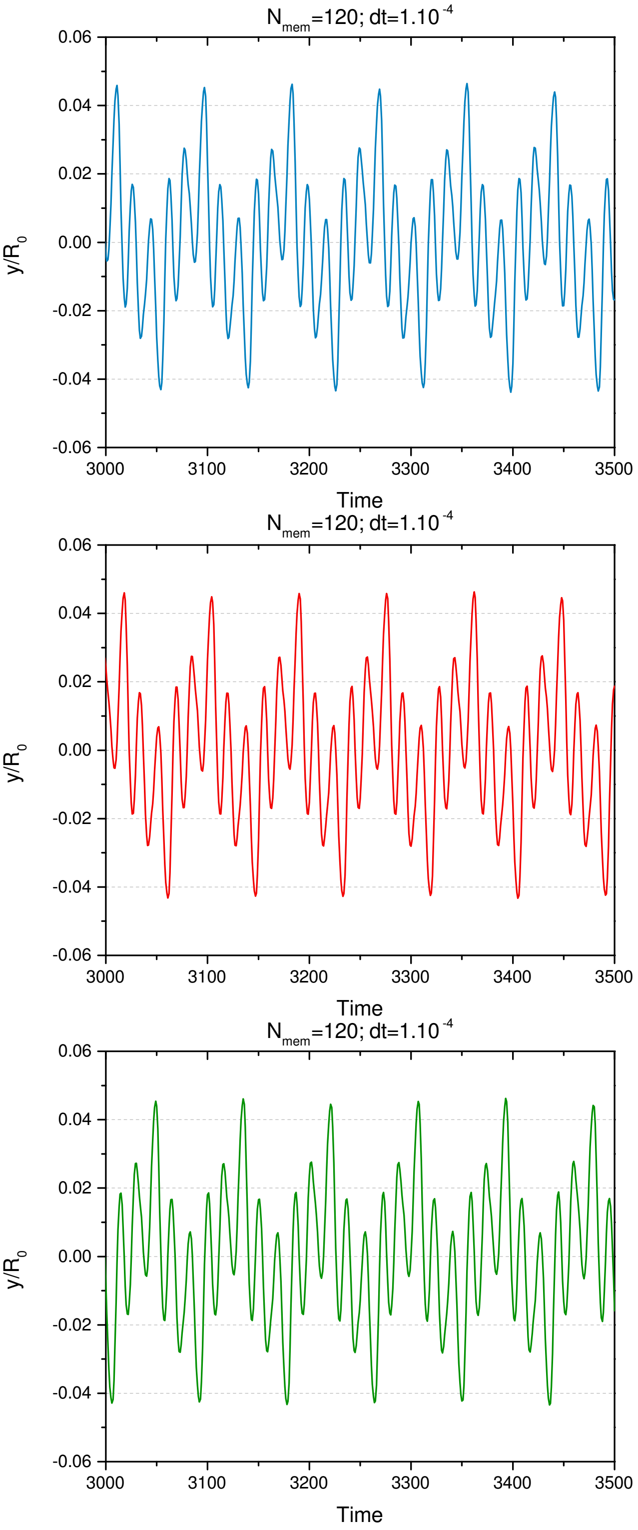

Figure 4.15: History of the lateral motion of the mass center of the vesicle for different initial shapes and positions. Top: the cell was initialized as an ellipse and placed in the center of the channel. Middle: the cell was initialized as an ellipse and slightly shifted from the center of the channel. Bottom: the cell was initialized as a parachute and placed in the center of the channel.

4.3.3.3 Pertinence of the Chaotic oscillations

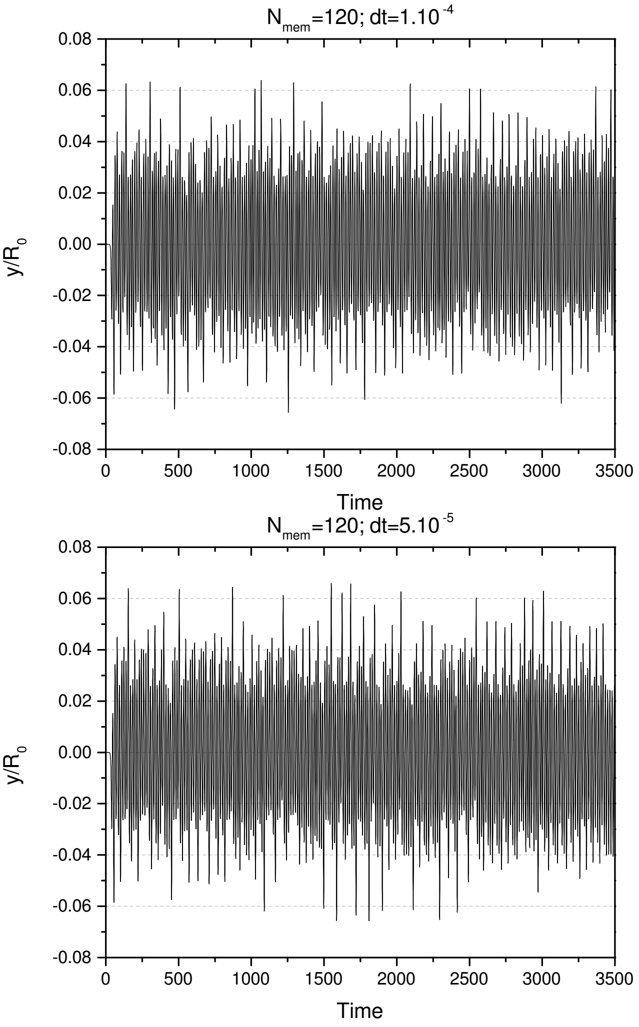

Figure 4.16: History of the lateral motion of the mass center of the vesicle showing a chaotic oscillations that persist even when changing the time discretization. The capillary number was fixed to $C_k = 6.25$ and the confinement to $C_n = 0.656$ which correspond to a channel width of around 9.15 microns. Top: $dt = 1.10^{-4}$. Bottom: $dt = 5.10^{-5}$.

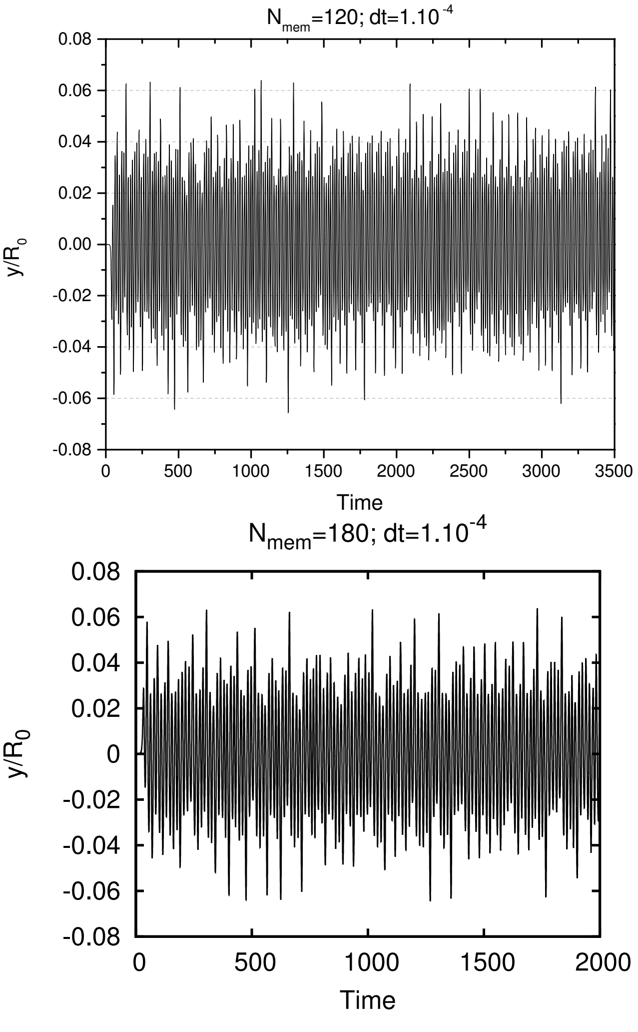

Figure 4.17: Same as figure 4.16 but changing the mesh number and fixing the time discretization to $dt = 1.10^{-4}$. Top: $N_{mem} = 120$. Bottom: $N_{mem} = 180$.

4.3.4 RBC-like vesicles in microcirculation conditions

The complex dynamics discussed above occur at low enough flow strength. We will examine now what happens at large enough flow strength by exploring other viscosity contrasts. We will start our study by fixing the viscosity ratio to $\lambda = 5$ ($\equiv$ a cytoplasmic viscosity of around 5 cP), which corresponds to the one of a young red cell. Recently Tahiri et al. [Tahiri 2013b] investigated numerically the deformation of a single vesicle bounded by two quasi-rigid walls (walls could deform slightly) using a boundary integral formulation in two dimensions. They reported, in addition to the symmetric and asymmetric regions, on a region of parameter space where there is a coexistence between the symmetric and asymmetric shapes (parachute and slipper). We have reinvestigated the effect of both confinement and capillary number on the morphology of a single vesicle for the case of rigid walls. We have observed two possible solutions for the range of parameters investigated namely: i)-parachutelike shapes and ii)-slipperlike shapes (Fig. 4.18). We have summarized the results in a phase diagram in (Fig. 4.19). Similar behavior was reported experimentally and discussed in [Schmid-Schönbein 1981]. We restrict the use of the word parachute for the strictly symmetrical solutions, where the word slipper covers the asymmetrical solutions. We have found series of symmetric-asymmetric-symmetric transitions. This transition was also observed in the experimental work of Abkarian et al. [Abkarian 2008a] and Tomaiuolo et al. [Tomaiuolo 2009], but not discussed in details. Tahiri et al. [Tahiri 2013b] report that a change in the inner viscosity of the cell from around 1 cP (viscosity

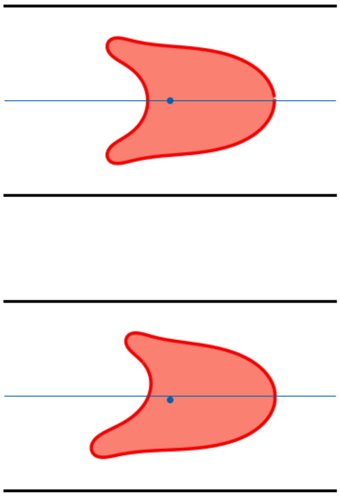

Figure 4.18: Stationary shapes exhibited by a rbc-like vesicle under the same conditions of flow and confinement ($C_k = 120$; and $C_n = 0.7$). Top: $\lambda = 5$ (cytoplasmic viscosity $\approx$5 cP). Bottom: $\lambda = 10$ (cytoplasmic viscosity $\approx$ 10 cP).

of the plasma), to around 5 cP (a typical value for a young red cell) leads to different stationary shapes. Given the importance of this parameter we have also investigated another larger value. It is important first to underline that (i) the cytoplasmic viscosity of the red cell is a variable from one cell to the other (within the same organism), due to age, and then (ii) its value depends on the mean corpuscular hemoglobin concentration (MCHC). The MCHC describes the concentration of the hemoglobin per unit volume of red cell. Cokelet and Meiselman report that the value of the cytoplasmic viscosity increases in a non-linear manner with the MCHC [Cokelet 1968]. During its lifespan, the mean cell volume (MCV) and the mean surface area of the red blood cell decrease with a constant ratio: the reduced volume of the cell remains the same [Linderkamp 1982, Guido 2009]. Since the concentration of the hemoglobin stays constant over time, the MCHC increases as function of the age of the cell. A typical value of the cytoplasmic viscosity for a young red blood cell is around $5-7$ cP, and corresponds to a value of MCHC of about $32g/dl$ [Mohandas 2008, Guido 2009]. For MCHC around $40g/dl$, the viscosity of the cell nearly quadruples [Chien 1987]. Therefore, one natural question is the impact of the cytoplasmic viscosity of the red cell on dynamics. We would like to see how does the phase diagram change (at high enough flow strength, corresponding to physiological values) when the viscosity contrast is high enough as compared to the so-called normal one, $\lambda = 5$. To fix the ideas we have set $\lambda = 10$, which corresponds to a cytoplasmic viscosity of around 10 cP . We report the results in Fig. 4.20. We observe that the slipperlike solution prevails when increasing the confinement and disappears for a $C_k W/R_0 \geq 190$. The separation region between the symmetric and asymmetric solutions is more pronounced than for the case of $\lambda = 5$. Indeed, for the range of the explored data, we do not observe any kind of transition from symmetry-asymmetry-symmetry (as for $\lambda = 5$), but rather a transition from symmetric to asymmetric shapes. We show clearly that the sta-

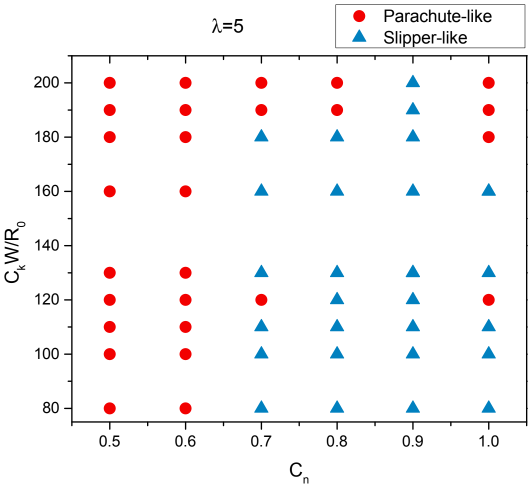

Figure 4.19: Phase diagram of a red cell-like vesicle ($\lambda = 5$) in a Poiseuille flow showing the existence of 3 different regimes at very high capillary number.

tionary solutions are sensitive to inner viscosity changes, as shown in Fig. 4.18. Considering that in most of the experimental works the cytoplasmic viscosity of the red cells is an unknown variable and most probably a non uniform one, this may give a lead about why for a fixed flow and confinement conditions, symmetric and asymmetric shapes can both be observed. Our study regarding this effect is only indicative and a systematic analysis should be postponed to the future. Indeed the size, the cytoplasmic viscosity, the membrane mechanical parameters (*i.e. bending stiffness*) of a healthy human young red blood cell are not constant, but rather lie in an interval of values, and change with the age of the RBC.This fact may make any direct comparison between experiments and numerics a bit difficult and challenging. As an example, the typical diameter of a red cell is 6 to 8 μm, where the accepted range of values for the bending rigidity of the membrane lies between 1.7×10^{-19} to $7 \times 10^{-19} J$ [Dao 2003]. The membrane stiffness may become higher in some pathological situation (*i.e. Malaria*).

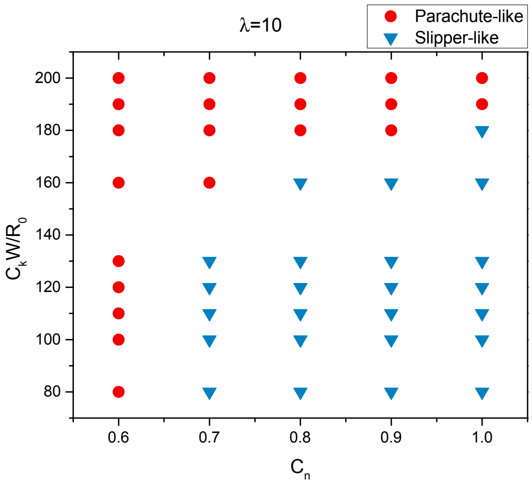

Figure 4.20: Phase diagram for $\lambda = 10$. The red and blue dots code respectively for parachutelike and slipperlike shapes.

4.4 Conclusions

The most pronounced result of our study is the discovery of surprisingly complex behavior of vesicles in a Poiseuille flow. This was possible because the effect of confinement and rigid boundaries was treated carefully for the first time. The dynamics has revealed 9 major distinct shapes and dynamics, ranging from symmetric and non-symmetric solutions, up to chaos. Dynamics of vesicles are treated here in the Stokes regime. In the absence of inertia, it is a classical result that the Poiseuille flow is always laminar. The existence of a single elastic object within the flow, acting only via bending forces, completely destroys the overall picture: chaotic dynamics take place. It would be interesting to investigate in the future the behavior of these chaotic regimes in the presence of many vesicles. It is tempt-

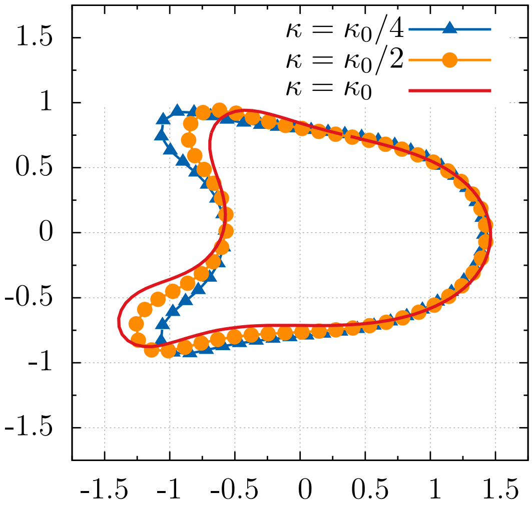

Figure 4.21: Effect of the membrane rigidity on the shape of the RBC. The values of the membrane stiffness (κ) are: i) $4 \times 10^{-19} J$ for the red line, $2 \times 10^{-19} J$ for the orange circles, and $1 \times 10^{-19} J$ for the blue triangles. Note that the accepted range of the membrane stiffness lies between 1.7×10^{-19} to $7 \times 10^{-19} J$. The x and y axis code for the x and y coordinates namely scaled by the typical radius of the cell.

ing to conjecture that the composite fluid would look like chaotic both in time (as reported here) but also in space. This problem could be viewed as a class of systems exhibiting the so-called elastic turbulence [Groisman 2000], that is a turbulence caused by the elasticity of the suspending entities when coupled to fluid flow in the purely Stokes regime. Elastic turbulence is characterized by a cascade of transfer of energy from large to small scales, akin to the Kolmogorov cascade for classical turbulence. A systematic analysis should be undertaken before drawing conclusive answers. The second important point to be discussed is the origin of the asymmetry in a symmetric problem. The asymmetry is inherited from the properties of the membrane of the vesicle. At equilibrium (in absence of external stresses), a vesicle will adopt a preferred shape (equilibrium shape) according to its reduced area (reduced volume in 3D) that will minimize the Helfrich free energy. By fixing a reduced area close to that of a red blood cell, Canham shows that the biconcave shape is the minimum energy of bending associated to constrained volume and area. When subject to external stresses (e.g. an imposed flow), independent from their natures, the vesicle's membrane will withstand deformations (bending and stretching). This resistance to the external stresses is measured by a dimensionless number, the Capillary number, which we define as the ratio between relaxation time of the membrane at rest and the flow time (defined as the inverse of the shear rate). At high shear rates, corresponding to physiological conditions in microcirculation, the flow time is faster than the relaxation time of the membrane, leading to almost (or completely) axisymmetric parachute-like or bullet-like shapes. The asymmetry is predominant only at low Capillary numbers. This is the reason why in experiments mimicking in vivo conditions in capillary flows, the slipper-like solutions are almost not present or instable. They may appear in the case of pathological or abnormal conditions affecting the membrane: rigidity for instance in early stages of malaria, and in cells in an advanced age where the cytoplasmic viscosity may be higher than 20 cP (whereas 5-7 cP is known as the typical value). Or more likely the asymmetry could be a consequence of hydrodynamic coupling, defects in the channels, or dust inside the channel where in these cases we may talk about instable asymmetric shapes. We are planning in the upcoming works to clarify the stability/instability of the slipper solution based on the elements mentioned in this discussion, to explain it in terms of potential or energy dissipation or other meaningful quantities.

CHAPTER 5

Mechanisms of Hydrodynamic Clustering

The red blood cells are known to form train of cells in the microcirculation attributed to a positive hydrodynamic interactions. We have investigated numerically the hydrodynamic coupling between the red blood cells (by using vesicles as a model) subject to a Poiseuille flow under different geometries. The effect of the inner viscosity, an intrinsic property of the red blood cell, on the pairing formation has been also studied. Interestingly, we found a stationary interparticle distance (an attractor) that depend of the channel width toward which the cells tend to evolve. A regime where a sign's reverse of the hydrodynamic interaction (negative coupling[1]) has been observed that depends from the channel width, and can be observed also by varying the inner viscosity.

5.1 Introduction

The motion of a linear array of rigid spheres at low Reynolds number (in absence of inertial effects) in a cylindrical tube under a Poiseuille flow was studied theoretically by [Wang 1969, Leichtberg 1976]. Wang and Skalak observed that the hydrodynamic interaction between the spheres is negligible above an interparticle distance of the order of the tube diameter. Leichtberg *et al.* reported that the velocity of the spheres decreases by increasing the array length, and that the outer spheres move faster than the central ones. The interparticle interactions, quantified via the relative velocity scaled by the midplane velocity of the imposed Poiseuille flow; are relatively small at low confinements, reach a maximum at middle confinements, and are quickly damped out at high confinement. The wall damping effect does not play an important role for closely packed arrays, whereas it becomes significantly important at larger interparticle spacing.

The hydrodynamic interaction between two drops was investigated experimentally by [Olbricht 1987]. They considered a pair of deformable drops with different sizes in a pressure-driven flow through a cylindrical capillary tube for a drop to tube diameter close from unity, and separated by an interparticle spacing greater than one tube diameter. The hydrodynamic interaction is owned to a difference in the particle velocities due to the difference in their sizes. The leading drop is bigger and moves slower than the trailing drop, which results in a decrease of the

---

[1] Negative from the sens that the hydrodynamic interactions lead to a repulsion.

spacing that becomes smaller than one tube diameter allowing then hydrodynamic interaction and formation of doublets (an array of two drops) before they coalesce into a single drop. Different combination of drops sizes, capillary numbers, and ratios between the inner and outer viscosities were taken into account. Among the results, it has been reported that an increase of the capillary number reduces the coalescence time in the cases where the trailing drop remains in the centerline of the channel. Above a critical capillary number and for a given size of the trailing drop, a lateral migration toward the wall is observed promoting a separation of the drops instead of an attraction. Indeed, if the size of the trailing drop is below a critical value, it is followed by a migration toward the wall. This critical size depends on the value of the capillary number.

Arrays of rigid spheres and deformable drops driven by a Poiseuille flow through a three dimensional rectangular channel in the Stokes regime was studied numerically by [Janssen 2012]. The effect of the deformability of the drops through different capillary numbers was also investigated. In the case of pairs of rigid spheres placed in the midplane of the channel, no relative particle motion can be produced since the particles move with constant and equal velocities. However for pairs of drops, the hydrodynamic interaction leads to an attraction at large separation distances and repulsion at small interdistances. The pair of drops tends to a stationary separation distance independently from the capillary number. In the case of a linear array of drops, the leading and trailing drops are always faster than the central ones. Thus, the trailing one catches up with the next one and form a pair. The pair moves slowly than single drops due to strong dipolar interactions between the pair drop and its direct neighbor. The same process will be repeated over time between the newly trailing drop and its neighbor. Meanwhile, the leading drop will quite the array, and the next drop will become the new leading and faster moving particle. The spacing between the trailing and leading drops will tend to increase in a monotonic manner. Nevertheless the repulsive nature of the short-ranged dipolar interactions does not allow to explain the formation of stable pairs. Indeed Janssen *et al.* pinpointed another contribution due to the deformability of the drops in the form of far-field quadrupolar interactions of an attractive nature. For complex deformable particles (i.e. biological cells), the effect of the geometry remains still unclear. Ghigliotti and co-workers studied numerically the pairing of a diluted suspension of vesicles; a popular model used to investigate red blood cells (RBCs); in an unconfined two dimensional geometry. They observed the formation of train of cells (called clusters) attributing this to a positive hydrodynamic interaction [Ghigliotti 2012]. McWhirter, Noguchi and Gompper investigated numerically the clustering of RBCs under a parabolic flow in three dimensional cylindrical channels [McWhirter 2011]. They have reported the formation of a fluid vortex or bolus between neighboring cells when clusters are formed, and pinpointed the effect of a decrease of velocity on the stability of the clusters. The formation/breakup of clusters is often observed in the microfluidics experiments built to depict the behavior of the RBCs in the microcirculation.

Colloidal particles confined between two parallel plates (quasi 2D geometry) were studied experimentally and theoretically by [Cui 2002, Cui 2004, Diamant 2005]. The complexity in these systems arises from the difficulty to decouple the effect of Brownian diffusion from hydrodynamic interactions. An antidrag between the moving particles attributed to a negative hydrodynamic coupling was reported. A change of sign of the hydrodynamic coupling in a cylindrical channel was also observed [Cui 2002]. The effect of boundaries on the hydrodynamic interactions has been studied in the case of water-in-oil droplets in 1D microfluidics [Beatus 2006, Beatus 2007, Shani 2014], and showed a non-monotonous behavior resulting from an interplay between the plug flow and the screening of the long-range hydrodynamic interaction induced by the confinement.

5.2 Description of the method

The present work employs a numerical approach based on the boundary integral method to solve the Stokes equations. The integral equation 3.42 is generalized for the case of N interfaces. The specific Green's functions satisfying the no-slip boundary at the two plates are calculated using the images method and a Fourier transform [Liron 1976, Thiébaud 2013]. The velocity along the membrane is given by

$$\begin{aligned}\mathbf{u}(\mathbf{X_0}) = \frac{2}{1+\lambda}\mathbf{u}^{\infty}(\mathbf{X_0}) + \frac{1}{2\pi\mu_1(1+\lambda)} \int\limits_{\sum_i \partial\Omega_i} \mathbf{G}(\mathbf{X},\mathbf{X_0})\mathbf{f}(\mathbf{X})dl(\mathbf{X}) \\ + \frac{(1-\lambda)}{2\pi(1+\lambda)} \int\limits_{\sum_i \partial\Omega_i} \mathbf{u}(\mathbf{X})\cdot\mathbf{T}(\mathbf{X},\mathbf{X_0})\cdot\mathbf{n}(\mathbf{X})dl(\mathbf{X})\end{aligned} \tag{5.1}$$

where $\mathbf{X}$ and $\mathbf{X}_0$ are two position vectors belonging to the membranes ($\partial\Omega = \partial\Omega_0 \cup \partial\Omega_1 \cup \cdots \cup \partial\Omega_n$). $\mathbf{u}$ and $\mathbf{u}^\infty$ are the membrane's velocity, and the imposed velocity. $\mathbf{G}$ and $\mathbf{T}$ stand for the Green's function for two parallel walls and its associated stress tensor. The Helfrich free energy (based on the bending energy) is used to model the membrane's response to the external stresses, and a tension-like energy via a Lagrange multiplier (denoted ζ) is added to fulfill the condition of inextensibility of the membrane (constant area and perimeter over time). The force exerted by the membrane on the fluid is then obtained by evaluating the functional derivative of the Hamiltonian (see chapter 3 for details). The cells are initially placed in the middle of the channel and subject to a Poiseuille flow.

5.3 Results

We perform simulations of a pair of vesicles flowing in channels with different widths. In all simulations, we have set the capillary number Ca to 10, the reduced area ν to 0.65, the viscosity ratio λ to unity, and varied the channel width. Fig. 5.1

shows the steady state of two cells flowing in channels with different widths. It comes out that at high and low confinements, the cells have a tendency to form clusters, when at middle confinement, the cells flow as single objects. Recalling the classical definition of a cluster of cells as: a train of cells separated by a distance smaller than 1.5 the diameter of the cell ($3R_0$ in our case). Then it follows

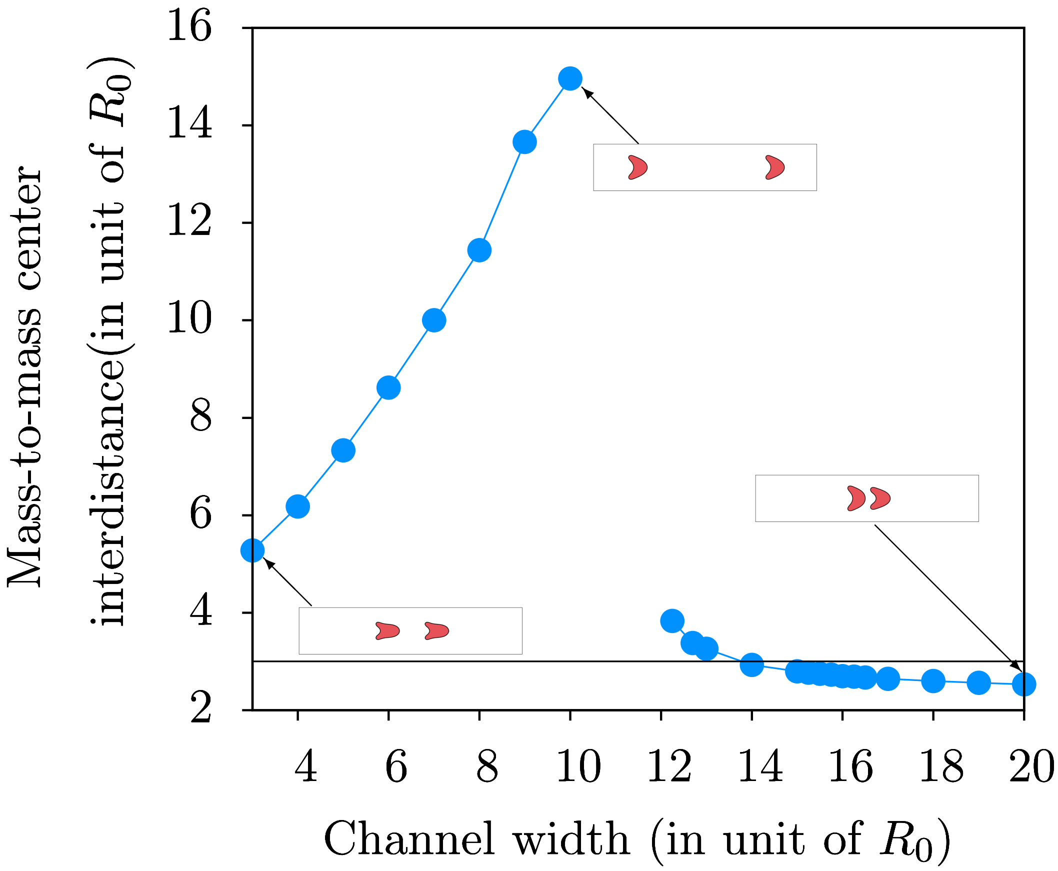

Figure 5.1: Mass-to mass center interdistance between two cells as a function of the channel width (W) for $\tau = 0.65$; $Ca = 10$; and a contrast of viscosity $\lambda = 1$. The solid horizontal black line corresponds to the arbitrary treshold distance of $3R_0$ introduced in [Tomaiuolo 2012] to define a cluster. The abrupt transition between $W = 10$ and $12R_0$ will be discussed in detail at the end of this chapter.

that clusters are not observed at high confinements, which correspond to situations studied in microfluidic experiments where cluster formation is reported. Before commenting this result, it is important to emphasize on the difference between our findings and those from the previous numerical work of GM where they disregarded the effect of confinement, by assuming an unbounded flow: situation where the walls are too far, so their effect on the cells could be neglected (the walls are not added to the model). This situation corresponds to the low confinement case (see Fig. 5.1), where our predicted stationary interdistances agree with the one of GM. It is important to recall that in experiments mimicking the flow of RBCs in microcirculation, the diameter of the cells is roughly the same as (or smaller than) the one of the channel. Therefor low confinement situations and unbounded geometries should not be used to explain experimental results as suggested in [Tomaiuolo 2012]. Moreover the notion of an unconfined Poiseuille flow is rather ambiguous since the effect of the confinement on the hydrodynamic interactions and pair formation is still not yet clear.

The spatial organization of vesicles into clusters similar to the one observed in microcirculation in the case of RBCs, has been explained by the mean of the hydrodynamic interactions leading to an attraction [McWhirter 2011, Ghigliotti 2012]. If the cells are close to each other, boli are created from the overlap of the velocity field induced by the cells. The cells are trapped and form a cluster (see Fig. 5.2). It is expected then due to the large interparticle distance at high confinement to do not observe boli by opposition to the low confinement clusters. Surprisingly at high confinement, situation of interest in experiments, boli are also observed between the cells which suggest that the cells are forming a cluster. The boli are more compressed laterally and squeezed horizontally (see Fig. 5.4) due to the confinement in comparison to low confined case. In the contrary, the experimental definition of a cluster based on the mass-to-mass center interdistance (i.e. $3R_0$) does not allow us to consider the pairs formed at high confinement as clusters strictly speaking. Therefor they are more likely flowing as single objects and supposed to not interact. It remains now to clarify whether the configuration with large interparticle distance and boli formed between the cells is a stable solution or not. In which case, we will have to redefine the notion of a cluster as reported in the literature.

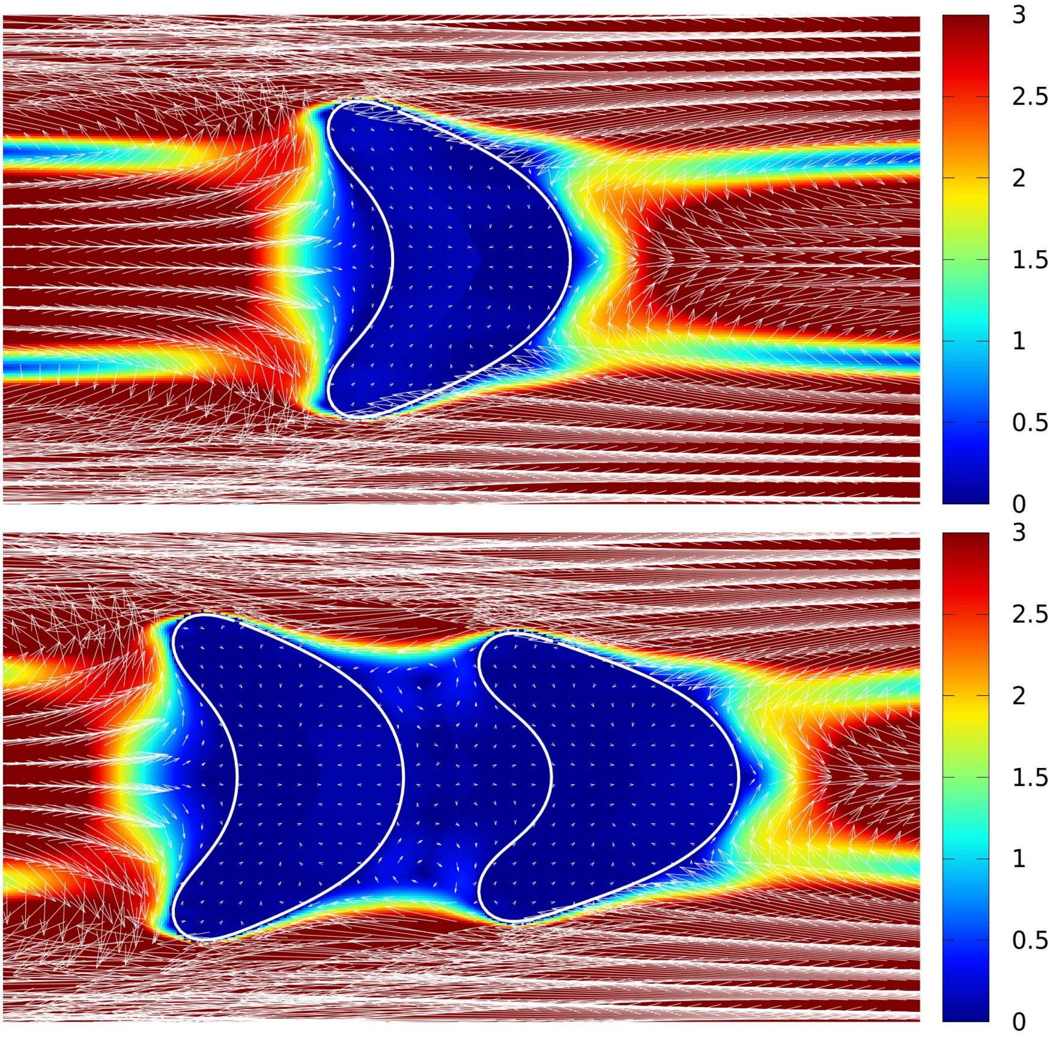

Figure 5.2: Velocity fields in the comoving frame of the cells: single vesicle (top), and a cluster of two vesicles (bottom). Two boli (vortices) are formed between the cells resulting from an overlap of the velocity field. The parameters read as: channel width $W = 20R_0$, the capillary number $C_a = 10$, the reduced area $\tau = 0.65$, and the viscosity ratio $\lambda = 1$.

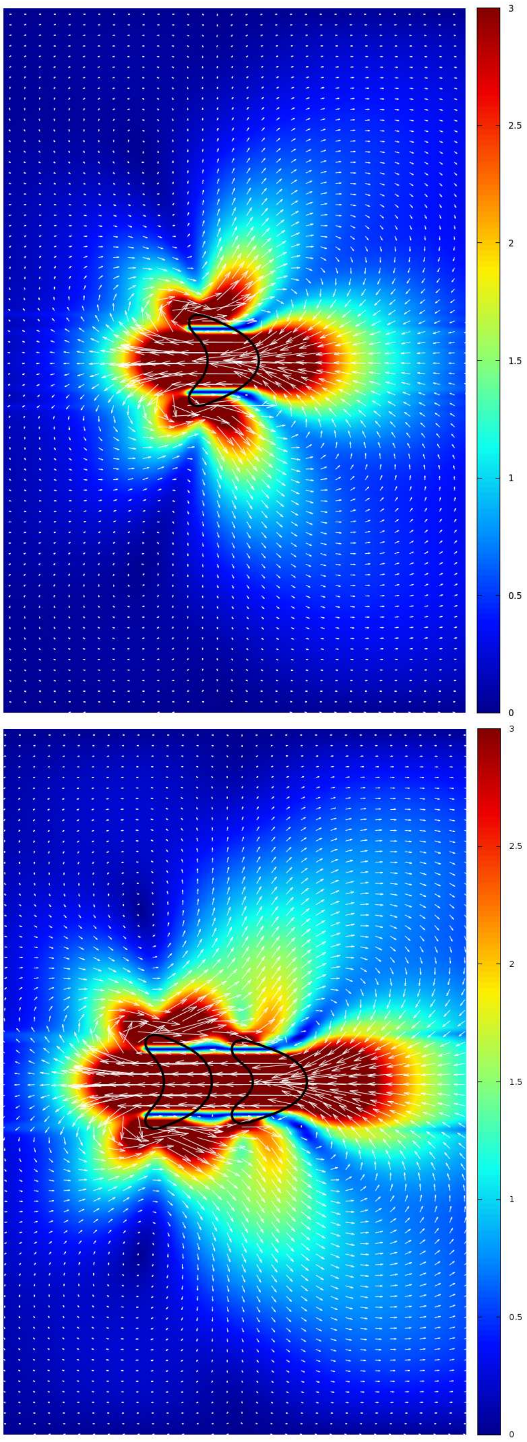

Figure 5.3: Disturbed velocity field induced by the cells obtained by subtracting the background velocity from the total velocity. Top: case of a single vesicle. Bottom: case of a cluster of two vesicles. Same parameters as in Fig.5.2.

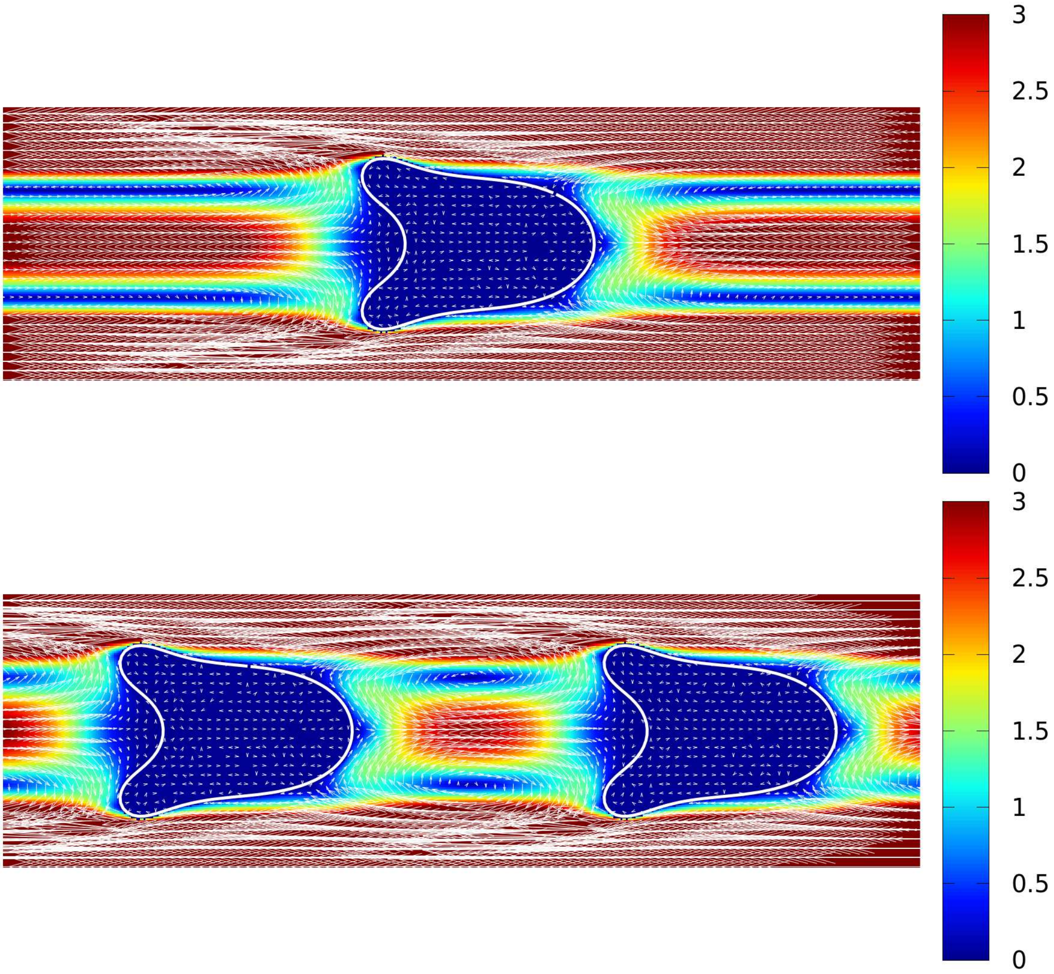

Figure 5.4: Velocity fields in the comoving frame of the cells: single vesicle (top), and a cluster of two vesicles (bottom). Two boli (vortices) are formed between the cells resulting from an overlap of the velocity field. The parameters read as: channel width $W = 3R_0$, the capillary number $C_a = 10$, the reduced area $\tau = 0.65$, and the viscosity ratio $\lambda = 1$.

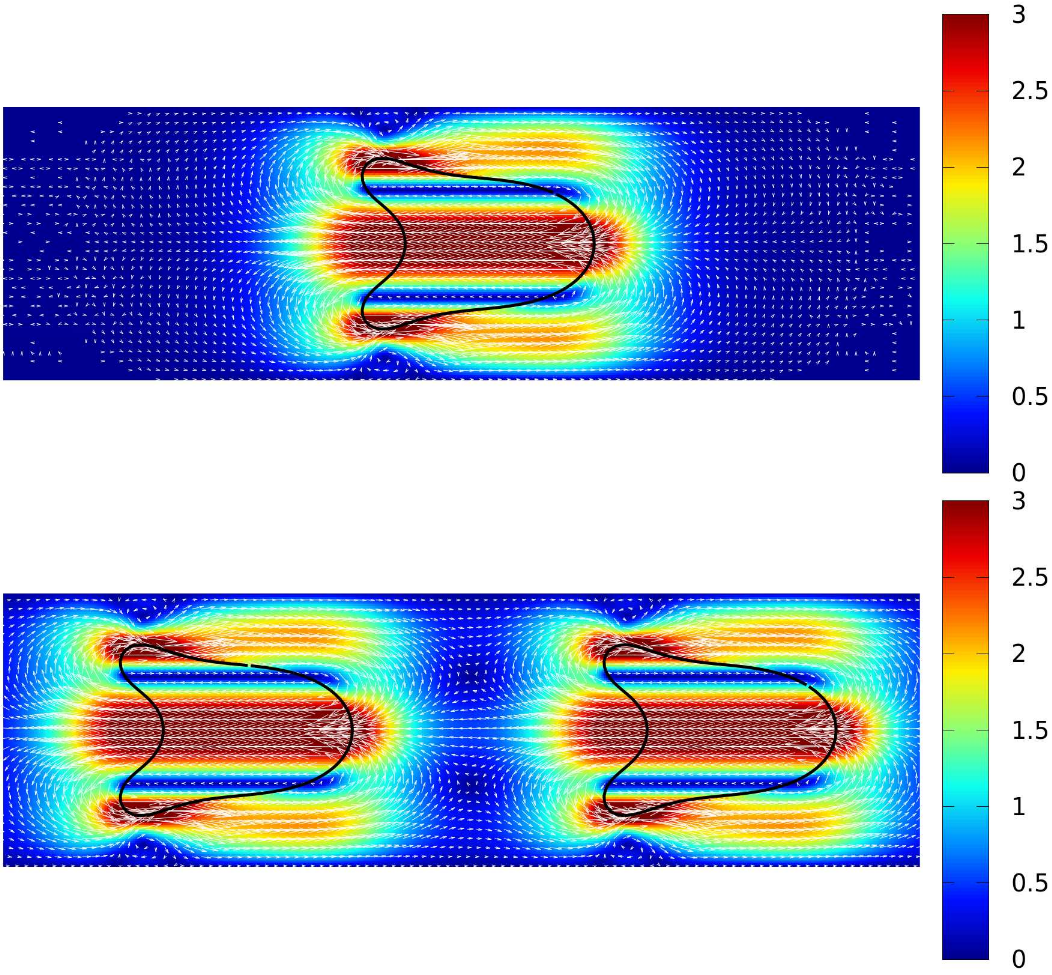

Figure 5.5: Disturbed velocity field induced by the cells obtained by subtracting the background velocity from the total velocity. Top: case of a single vesicle. Bottom: case of a cluster of two vesicles. Same parameters as in Fig.5.4.

5.3.1 Estimation of the hydrodynamic interaction length

To emphasize more on the intricate relation between confinement and pairing, the hydrodynamic interaction range was studied as function of the channel width. The estimation of this quantity is obtained by subtracting from the total dissipation, the background dissipation due to the imposed flow. Let's consider the function

$$f(x) = \ln(|\ \mathscr{D}(x)\ |), \quad x \in \mathbb{R}$$

where $\mathscr{D}$ is the dissipation induced by the cell near the wall.
The function f has a global maximum y_{max} at x_m such as

$$y_{max} = \ln(|\ \mathscr{D}(x_m)\ |)$$

and a global minimum y_{min} where the dissipation reaches a constant value corresponding to the limit of the hydrodynamic range (see Fig.5.6). Eventually, we can define the hydrodynamic length by the abscissa corresponding to the global minimum of f, but to avoid numerical noises, we add a positive non zero constant ε such as

$$y_{max} + \ln(\varepsilon) \longrightarrow y_{min}, \quad \texttt{and} \quad |\ y_{max} + \ln(\varepsilon)\ | < |\ y_{min}\ |$$

The interaction length (L_{int}) is defined as

$$L_{int}/2 = max(|\ [y_{max} + \ln(\varepsilon)] \cap f(x)\ |)$$

An example of how we define the interaction length of a single cell is given in the Fig.5.6. The interaction length is calculated from the mass center of the cell.
We found that the hydrodynamic interaction length is linearly proportional to the channel width (W) and is estimated to $4W$.

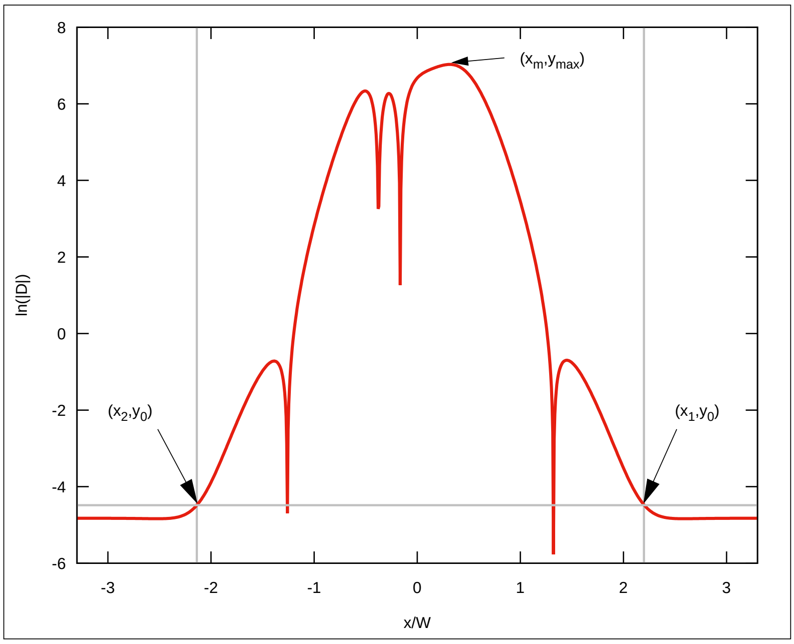

Figure 5.6: Interaction length of a single cell counted from its mass center. The solid red line represents the dissipation induced by the cell near the lower wall for the case of $W = 3R_0$.The grey lines are only guide for the different steps needed to define the interaction length. The interaction length is defined as twice the distance from the mass center of the cell located at $x = 0$, and $max(x1, x2)$ where x_1 and x_2 are the abscissa corresponding to the intersection between y_0 and $\ln(|\ \mathscr{D}(x)\ |)$. y_0 is defined as $y_0 = y_{max} + \ln(\varepsilon)$.

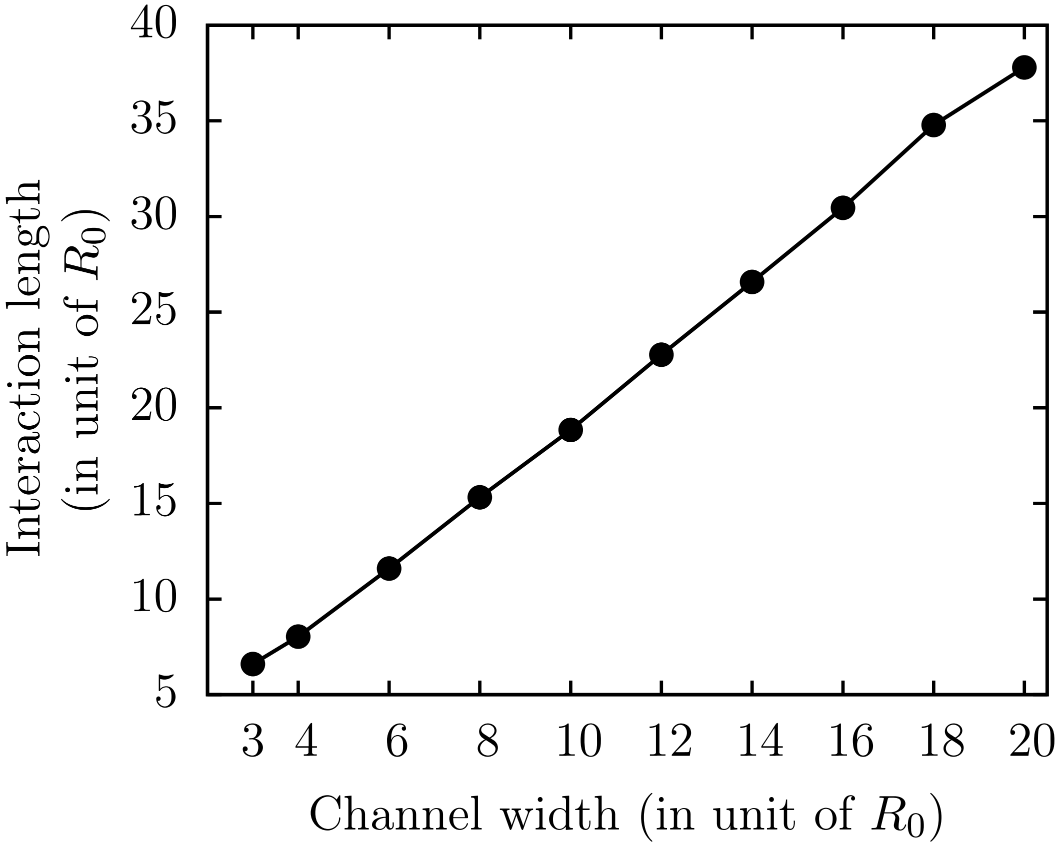

Figure 5.7: Estimation of the hydrodynamic interaction length induced by a single cell as a function of the channel width. The dissipation near one of the walls is used to define the interaction range. The reduced area is $\tau = 0.65$, and the viscosity ratio is $\lambda = 1$. The cell is subject to a Poiseuille flow with $Ca = 10$. The estimated range of the hydrodynamic interaction is around $4W$, where W is the channel width.

5.3.2 Phase diagram and basin of attraction

Now that we have an idea about the hydrodynamic interaction length as function of the confinement, we can evaluate the stability of the pairs by increasing and/or decreasing the stationary interdistance obtained at the end of the simulations. This is equivalent to adding a noise and checking whether the cells will tend again to their stationary interdistance or not. In Fig. 5.8, the channel width is fixed to $14R_0$, the capillary number to 10, and the cells are placed away from their stationary interdistance $df = 2.93R_0$. Starting from an initial interdistance of $10R_0$, the cells are attracting each other, and then reform a cluster with the same $df = 2.93R_0$. However, when the initial interdistance has been set to $11R_0$, the cells repeal each other, suggesting a negative hydrodynamic coupling by opposition to hydrodynamic interaction leading to an attraction. This sign's reversal is observed by either changing the channel width or the initial interdistance between the cells. Nonetheless for channel widths below $10R_0$ and those above $17R_0$, this phenomenon is not observed. A phase diagram summarizing these results is presented in Fig. 5.9. Interestingly, the first observation is that for channel widths below $W = 10R_0$ the final interdistances between the cells is far bigger than the threshold introduced by Tomaiuolo et al (TG) in [Tomaiuolo 2012]. Indeed, a typical distance of $3R_0$ has been used by TG to define clusters of RBCs experimentally. This definition is arbitrary and is not based on any theoretical reasoning. Stable fixed points (attractors) are observed in this region, corresponding to stable clusters. Therefor the clusters in this region has been underlooked in the previous experimental and theoretical works. The second important feature is the discon-

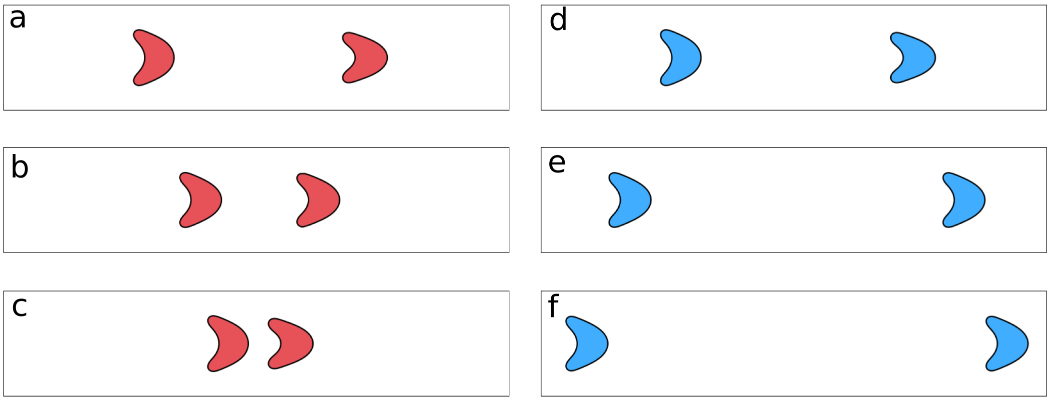

Figure 5.8: Hydrodynamic interaction between a pair of vesicles leading to two different scenarios, namely attraction (red), and repulsion (blue). Snapshots at different time steps are shown, upper and lower figures represent the initial and stationary configuration. Channel width was $14R_0$. The other parameters read as capillary number $Ca = 10$, reduced area $\tau = 0.65$, and viscosity ratio $\lambda = 1$. The initial mass-to-mass centers interdistance between the vesicles was: (a) $D_i = 10R_0$, and (d) $D_i = 11R_0$.

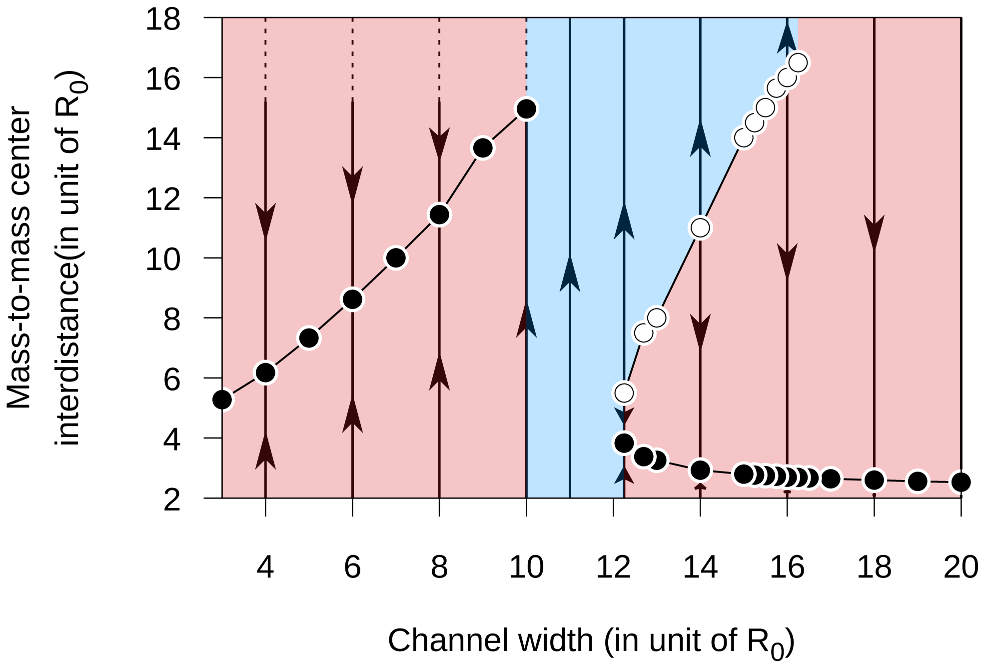

Figure 5.9: Phase diagram of the hydrodynamic interaction between two vesicles as a function of the confinement. The red area depicts the range of the basin of attraction. The solid black dots are the stable fixed points representing the stationary interdistances (attractors). The open circles represent unstable fixed points (repellers). A discontinuity is observed for channel widths $10R_0 < W < 12.25R_0$, where no stable solution is found. The blue area represents an area where the cells are repealing each others. The dashed lines represents regions where it was not possible to estimate the exact solution in a reasonable amount of time.

tinuous evolution of the interdistance as a function of the channel width. No stable solution is observed for a range of channel widths lying between $10R_0$ and $12.25R_0$. Above $W = 12.25R_0$, both stable and unstable fixed points are found. However, the unstable fixed points disappear at larger channels ($W > 16.25R_0$). The normalized relative velocity of the pair defined as the difference of velocities between the front and the backward cells ($u_2 - u_1$) normalized by the background midplane velocity (u_0) gives an insight about the change of sign of the hydrodynamic interaction as a function of the interparticle distance. The possible cases can be summarized as follow:

1. $(u_2 - u_1)/u_0 > 0$: the cells are repealing each other.

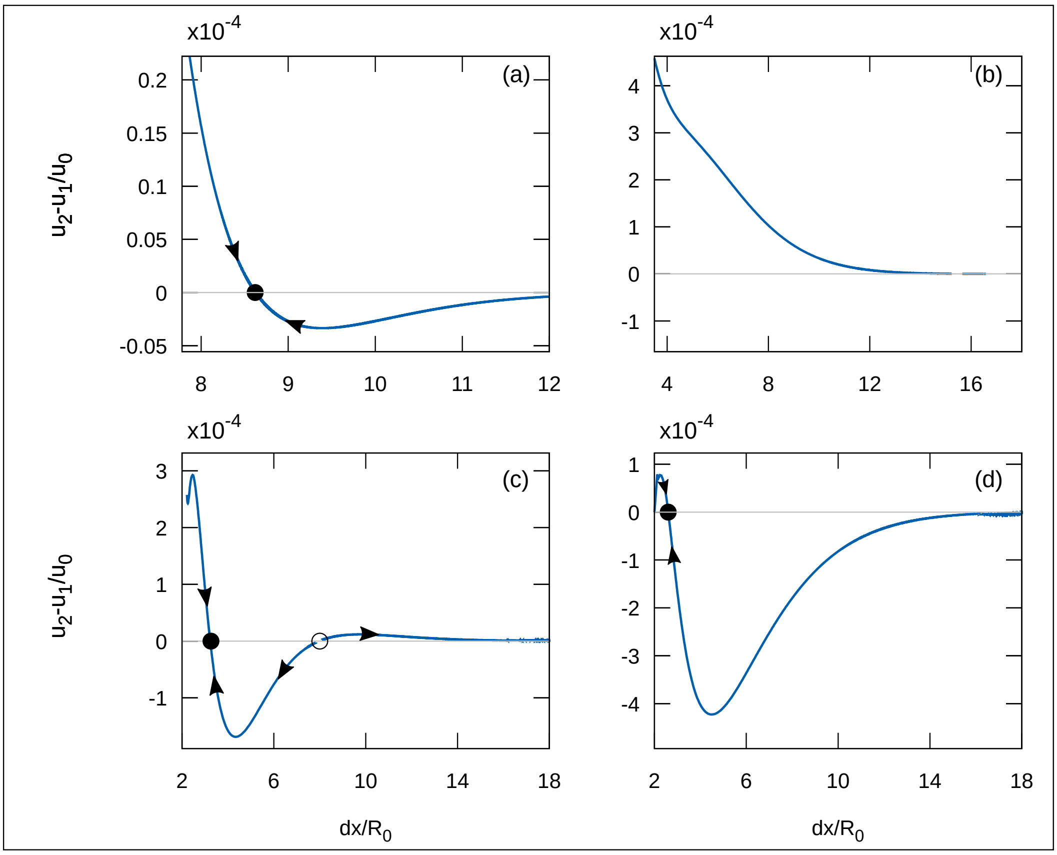

Figure 5.10: Normalized relative velocity as a function of the mass-to-mass center interdistance between the two cells. a) $W = 6R_0$; b) $W = 11R_0$; c) $W = 13R_0$; and d) $W = 18R_0$. The solid black dots are stable fixed points, and open circles represent unstable fixed points.

2. $(u_2 - u_1)/u_0 < 0$: the cells are attracting each other.
3. $(u_2 - u_1)/u_0 = 0$: the interdistance corresponds to a stable or unstable fixed point. If it is a stable fixed point then we are in the presence of a cluster.

The Fig. 5.10 depicts the different cases observed in the phase diagram. Fig. 5.10 (a) and (d) corresponding namely to $W = 6$ and $18R_0$ show cases where the initial interdistance tends towards the stable fixed point representing the stationary distance of the cluster. Fig. 5.10 (b) corresponds to the case where no stable solution is reached for $W = 11R_0$. In Fig. 5.10 (c), both stable and unstable fixed points are observed for $W = 13R_0$. Below the unstable fixed point, the interdistance is converging to the stable fixed point. Whereas above the unstable fixed point, the interdistance tends asymptotically to the next stable fixed point.

5.3.3 Effect of the intrinsic properties of the cells on clustering

5.3.3.1 Viscosity contrast

In Fig. 5.11, we consider a pair of vesicles flowing in a channel with a fixed diameter (W) of $3R_0$. The inner viscosity (μ_2) is varied from 1 cP to 20 cP, and the effect on clustering is studied. The other parameters read as: 0.65 for the reduced area, 10 for the capillary number, $1cP$ for the outer viscosity (μ_1). One should emphasize that for a healthy human RBC the physiological range of cytoplasmic viscosity $\mu_2 \geq$5 cP and increases in a non linear manner with the age of the cell exceeding the 20 cP. The first remark is the transition from symmetric parachute-like to asymmetric slipper-like shapes when increasing the inner viscosity. This transition induces a decrease of the interparticle distance since the slipper are faster than the parachute shapes. A discontinuity is observed for $7cP \leq \mu_2 \leq 9cP$, where we enter in a repulsion regime. So far these results are still preliminary, and a more detailed analysis is needed before drawing any conclusions.

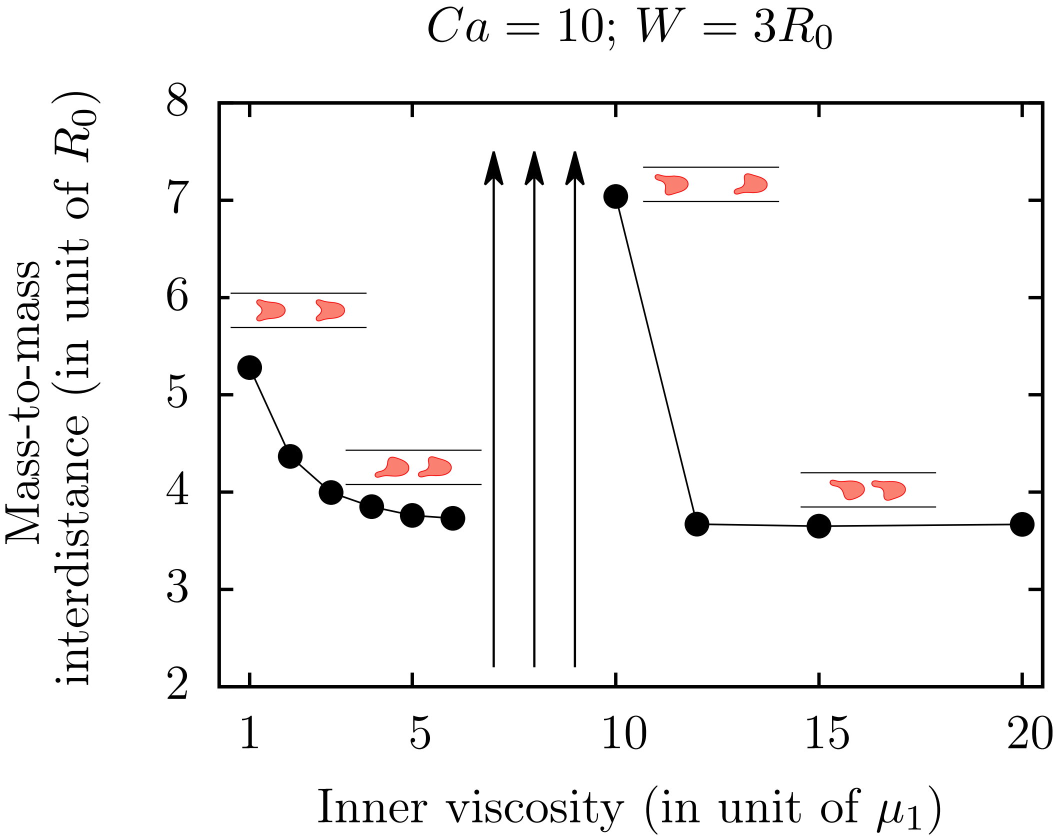

Figure 5.11: Effect of the inner viscosity on the stationary mass-to-mass center interdistance of a pair of two cells.

5.3.3.2 Membrane rigidity

The effect of the membrane bending stiffness on the interparticle distance of a pair of cells is investigated. In these simulations, the typical radius of our vesicles is $R_0 = 4\mu m$, the cytoplasmic viscosity is $\mu_2 = 5$ cP, and the membrane stiffness is $\kappa = 4 \times 10^{-19} J$. The accepted range of values for the bending rigidity of the membrane lies between 1.7×10^{-19} to $7 \times 10^{-19} J$. The reduced area (τ) of the vesicles is chosen to match the one of a human red blood cell ($\tau = 0.65$). We choose the flow parameters and confinement in such a way that we can do a comparative study with the experimental work done by V. Clavería, a PhD student at our laboratory. The main result regarding cluster induced by hydrodynamic interactions is the apparition of a double pick in the probability density function suggesting the existence of two stationary interparticle distances as shown in Fig. 5.12. Using numerical simulations based on these experiments, we find out that the wide interval of values of the membrane bending rigidity may lead to two different interdistances. This difference arises from the loss of symmetry as a consequence of an increase of rigidity within the physiological range (see Fig. 5.13).

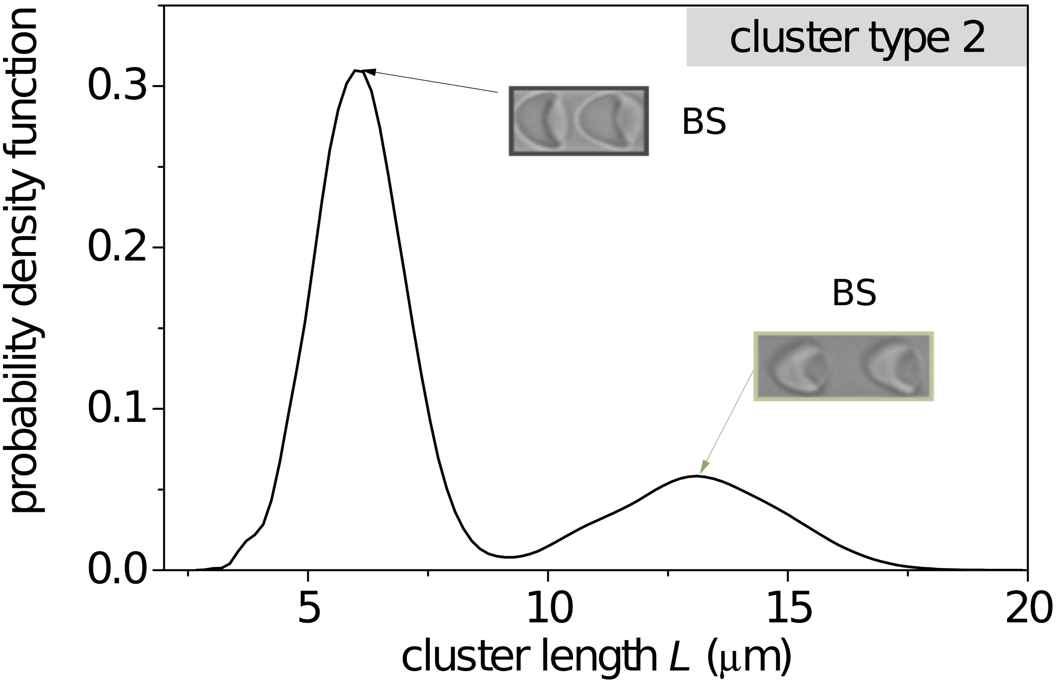

Figure 5.12: Probability density function of cluster formed by two cells. The figures on the graphs are representatives snapshots of the most frequent clusters configurations. The two peaks on the graph suggests two possible equilibrium states with two different interparticle distances. BS refers to the buffer solution without addition of macromolecules inducing aggregation. The Dextran case is not discussed in this chapter. Courtesy of V. Clavería experimental work in the group of Prof. Dr. C. Wagner in Saarland University.

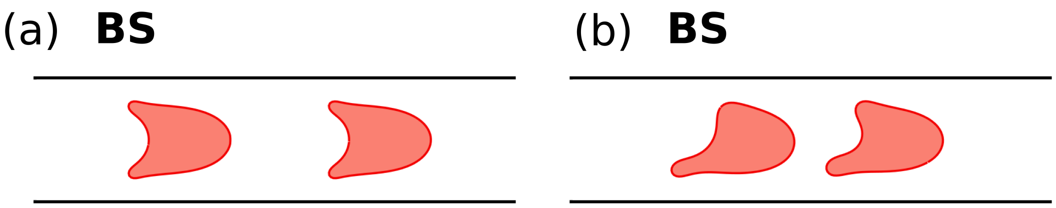

Figure 5.13: Effect of the membrane stiffness on the interparticle distance of a cluster formed by two cells. Membrane bending stiffness are (a) $\kappa = 4 \times 10^{-19} J$ and (b) $\kappa = 7 \times 10^{-19} J$.

5.4 Conclusions

The mechanism of pairing is investigated in the presence of bounding walls. The effects of the confinement and the intrinsic properties of the vesicles is considered. We observe first that the stationary interdistance between the cells increases with the increase of the channel width. Above a critical channel width $W = 10R_0$, a discontinuous transition occurs where no stable solution is found. The system becomes stable again at $W \geq 12.25R_0$, and an opposite effect of the confinement on the interdistance is observed in this area. Indeed, the interdistance decreases by increasing the channel width. The observed interdistances are similar to the one commonly used in the literature to define clusters of RBCs. Then, the stability of these clusters is studied by perturbing the system, which allow us to determine the consequent basin of attraction. The observed stationary interdistances correspond to stable fixed points (attractors) toward where the system evolve when driven out of equilibrium in the limit of the basin of attraction. Unstable fixed points (repellers) are also observed for a range of channel width lying between $W = 12.25$ and $16.25R_0$. The stable fixed points correspond to the stationary state of the cluster, and could be used instead of the more arbitrary definition based on the maximum interdistance of $3R_0$ proposed in [Tomaiuolo 2012]. In the last part of this chapter, it comes out from the experimental work on RBCs flowing in microchannels done in by group that the hydrodynamic interactions may lead to the formation of clusters with two stable interparticle distances even though the imposed flow and confinement were the same. This leaves us with the intrinsic properties of the RBCs as a probable cause. By investigating two of them separately (the inner viscosity and the membrane bending stiffness) we observe a bimodal distribution of the hydrodynamic clusters. Though we have pinpointed some of the ingredients that can explain the experimental observations on the flow of RBCs from one hand and showed the versatility of hydrodynamic interactions under confinement from the other hand, the full understanding of these phenomena cannot be achieved without building an analytical model that includes the effect of walls on hydrodynamic interactions between soft deformable objects.

CHAPTER 6

Aggregation of Red Blood Cells and Protein Induced Clusters in Microcirculation

---

In this chapter, we present a toy model to study the mechanism of aggregation of RBCs and cluster formation induced by macromolecules at flow condition. Using a combined experimental and numerical approach [Brust 2014], we show that, despite the large shear rate in microcapillaries, either fibrinogen or the synthetic polymer dextran leads to an enhanced formation of robust and stable clusters of red cells, even at hematocrit as low as 1%. In addition, a comparative study between clusters induced by pure hydrodynamic interactions and those formed in the presence of macromolecules shows a pronounced difference in the morphology and the intercellular distances.

6.1 Introduction

Blood performs multiple functions in the body, like oxygen, carbon dioxide and nutrients transfer or body temperature control by heat transfer. The flow properties of blood are complex, in opposite to simple fluids such as water or air. This complexity arises from its inhomogeneous composition: a little less than half of the blood is made up of cellular compartment suspended in an aqueous fluid (plasma). The solid part of the blood is mainly formed by erythrocytes, or red blood cells (98% of the blood cells), and the rest is composed by white cells and platelets. The plasma itself, is a complex solution of solutes: ions, metabolic molecules (e.g. glucose and amino acids) and proteins, suspended in water. In the healthy adult human, the red cells have a tendency to aggregate and form, under certain conditions, large aggregates called rouleaux. This phenomenon is a consequence of the presence of some kinds of macromolecules in the plasma such as fibrinogen (a plasma protein known to induce aggregation). According to the literature, the aggregates are supposed to disaggregate under the effect of shear forces. Under microcapillaries flow conditions, red cells are known to form small train of cells called clusters due to hydrodynamical interactions. The role of plasma proteins was marginalized due to the high shear rate in microcapillaries [Popel 2005]. In the present work, we investigate the effect of macromolecules on cluster formation under flow condition and the mechanism of rouleaux formation in a quiescent

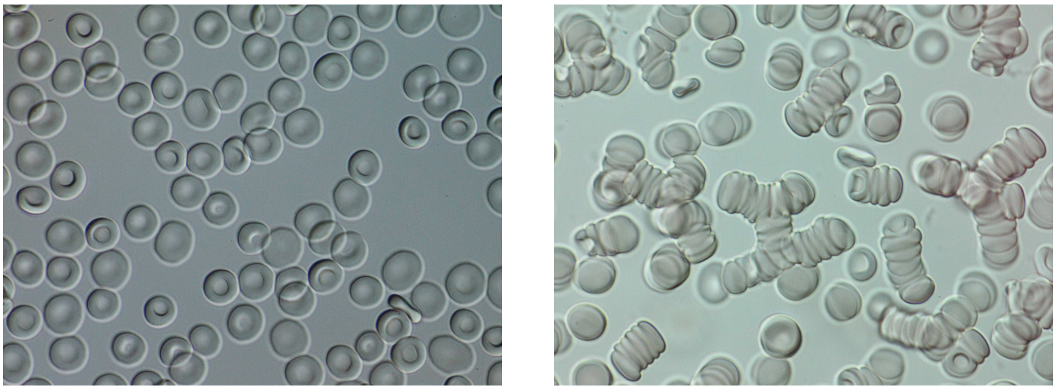

Figure 6.1: RBCs suspended in a phosphate buffer saline solution (PBS). Left: in the absence of macromolecules inducing aggregation (such as dextran and fibrinogen), the RBCs do not aggregate due to their surface negative charge. Right: in the presence of these macromolecules, the RBCs form a 3d aggregate called rouleaux when the adhesion forces (bridging or depletion) exceed the disaggregation forces. Courtesy of C. Ruloff (PhD student in Prof. Dr. C. Wagner's group).

fluid. A toy model is introduced based on experimental measurements of the adhesion energy between two RBCs [Brust 2014, Steffen 2013], and combined to the theoretical model described in chapter3.

6.2 Cell-cell interaction model

Currently, there are two different and opposite models to explain the aggregation of RBCs in polymer solutions: the bridging model and the depletion model. In the bridging model, it is assumed that erythrocyte membrane adsorb surrounding polymers (fibrinogen or dextran) and form a kind of bridge with the neighboring erythrocytes[Chien 1975, Maeda 1986b]. The depletion model was introduced more than half a century ago by Asakura and Oosawa[Asakura 1958], and states that if the space between two cells reaches a critical distance, the difference of osmotic pressure due to the lack of macromolecules in the intercellular region and the bulk will induce an attractive force which tends to minimize the space between the two cells. Neu and Meiselman have presented a model taking into account the strong electrostatic repulsion due to the negative charge of RBCs membrane, and the weak osmotic attractive forces due to the depletion effect induced by the macromolecules surrounding the RBCs. The depletion force model includes the effect of the polymer concentration, the polymer physiochemical properties on depletion layer thickness, and the polymer penetration depth into the RBC glycocalyx. Recalling that the glycocalyx refers to glycoproteins covering the membrane of the RBC, and responsible of its negative charge. Although it is a simplified model based on a couple of approximations, a good agreement with experimental measures of cell-cell affinity and RBC aggregation is observed [Neu 2002]. The draw-

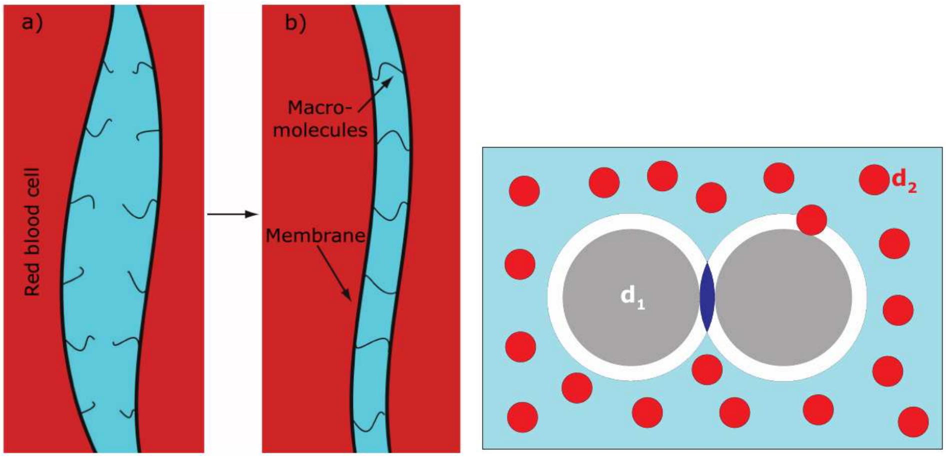

Figure 6.2: Schematic of the mechanism behind the aggregation of RBCs. Left: The macromolecules are adsorbed by the glycocalyx of the RBC, which may lead to the formation of bonds or bridges if another cell is close enough (in the range of the length of the polymer). Right: The macromolecules are depleted from the excluded region between two neighboring RBCs, leading to a poor polymer region between the cells, and a rich polymer region around. An osmotic gradient will induce an attractive force pushing the cells toward each other and forming a rouleaux. In both cases, if the adhesion forces (bridging or depletions) are higher than the disaggregation forces (due to electrostatic repulsion, membrane strains and mechanical shearing), the RBCs will form a rouleaux (a stack of cells) [Steffen 2012].

back of this model is the large number of parameters to tune depending from the physiochemical properties and the concentration of the polymers. In other words, a lot of different experimental data are needed in order to use this model for predictions. Based on a new set of experiments done in our group, the RBC-RBC adhesion energy has been quantified using the atomic force microscopy-based single cell force spectroscopy. The principle of this technique is described in Fig 6.3, and details are provided in [Steffen 2012, Steffen 2013]. These measurements provide us with the first direct experimental quantification of dextran and fibrinogen induced depletion forces between RBCs in their natural discocyte shape. The results are summarized in Fig 6.4. Knowing the total interaction energy allow us to use a Lennard-Jones potential to reproduce the intercellular interactions between the cells in order to mimic the effect of a given concentration of Dextran (70 and 150) or fibrinogen by fixing only one parameter: the intercellular surface energy. This parameter is deduced directly from the data in Fig 6.4.

$$\phi(r) = 4\varepsilon[(\frac{\sigma}{r})^{12} - (\frac{\sigma}{r})^{6}] \tag{6.1}$$

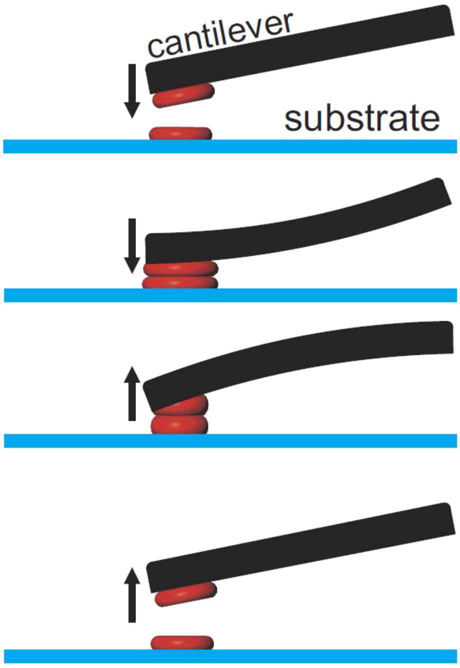

Figure 6.3: Sketch of the measurements of the adhesion energy using atomic force microscopy-based single cell force spectroscopy. One RBC is fixed to the cantilever, and the other one to the surface of a Petri dish containing a solution of macromolecules. Both cells are brought into close contact. Then when withdrawing the cantilever, the adhesion force is measured via the deflection of the cantilever. The measurements were performed for different concentrations of the synthetic sugar polymer dextran with different molecular weights (70 and 150 kDa), and for the protein fibrinogen [Steffen 2013, Brust 2014].

The weak depletion attractive and strong electrostatic repulsive forces at far and near distances are the negative derivative of the intercellular interaction potential

$$\mathbf{f}^{\phi}(\mathbf{X}) = -\int_{\sum_{j\neq i}\partial\Omega_j} \frac{\partial\phi(r)}{\partial r}\frac{\mathbf{r}}{r}ds(\mathbf{Y}) \tag{6.2}$$

where ε and σ denote for the surface energy and the zero force length distance. $\mathbf{r} = \mathbf{X} - \mathbf{Y}$, $r = \|\mathbf{X} - \mathbf{Y}\|$, and X and Y are two position vectors belonging to the $i-th$ and $j-th$ membrane respectively The Stokes equations are solved using the boundary integral technique introduced in chapter 3.

$$\mathbf{u}(\mathbf{X}_0) = \frac{2}{1+\lambda}\mathbf{u}^{\infty}(\mathbf{X}_0) + \frac{1}{2\pi\mu_1(1+\lambda)}\int_{\sum_i\partial\Omega_i} \mathbf{G}(\mathbf{X},\mathbf{X}_0)[\mathbf{f}(\mathbf{X}) + \mathbf{f}^{\phi}(\mathbf{X})]dl(\mathbf{X})$$
$$+\frac{(1-\lambda)}{2\pi(1+\lambda)}\int_{\sum_i\partial\Omega_i} \mathbf{u}(\mathbf{X})\cdot\mathbf{T}(\mathbf{X},\mathbf{X}_0)\cdot\mathbf{n}(\mathbf{X})dl(\mathbf{X}) \tag{6.3}$$

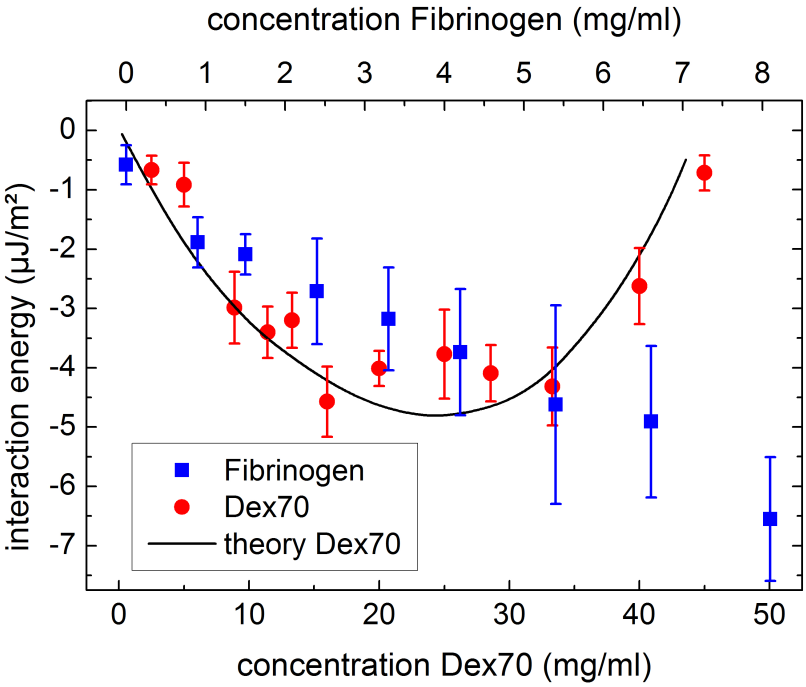

Figure 6.4: RBC-RBC adhesion energy as a function of macromolecules concentrations [Brust 2014]. The x-axis codes for the concentration of: (bottom) Dextran 70, and (top) Fibrinogen.

6.3 Results

The aggregation and flow of RBCs in microcirculation are investigated numerically. The cell model comprises closed inextensible membranes (giant vesicles) filled with fluid (modeling hemoglobin) and suspended in a different fluid (modeling plasma). The vesicles can freely deform in response to the imposed Poiseuille flow. Cells can interact by both hydrodynamic forces and by an additional interaction potential with interaction energies that were taken from single cell force spectroscopy measurements with fibrinogen and dextran.

6.3.1 Rouleaux formation in a quiescent fluid

The aggregation of RBCs is briefly studied and preliminary comparative results between experiments and numerical simulations are presented. We consider doublets and set of 7 cells placed in the middle of a channel of width $20R_0 \approx 60$ µm. The reduced area is fixed to 0.65, and the viscosity ratio to unity. The shape of the doublets and rouleaux of 7 cells as a function of the interaction energy is shown in Fig. 6.5. The equilibrium shapes of aggregate of RBCs was investigated by the mean of an adhesion potential where the interaction energies was changed systematically [Svetina 2008, Zhang 2008, Ju 2013]. Nevertheless, a quantification of

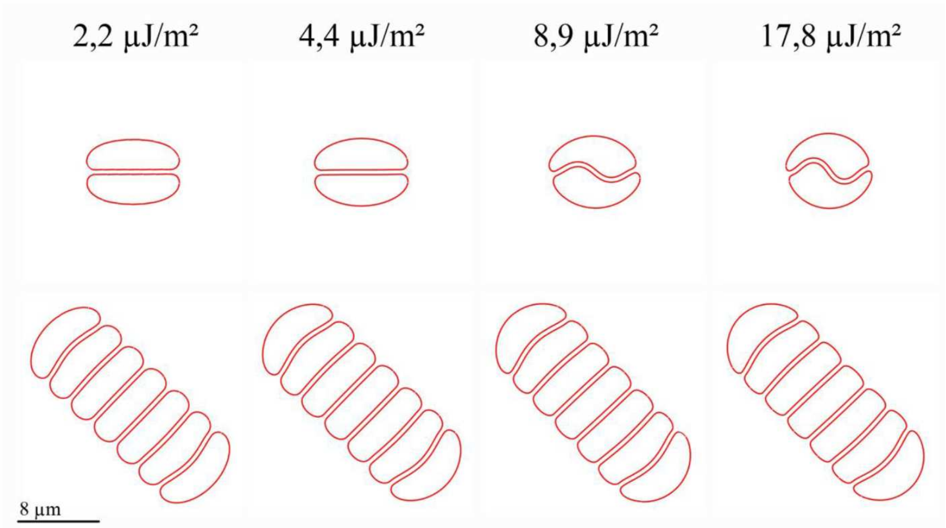

Figure 6.5: Effect of interaction energy on the morphology of aggregates of RBCs in case of doublets (top), and rouleaux of 7 cells (bottom).

the interaction energy corresponding to a specific concentration of Dextran or fibrinogen was lacking. In the best of our knowledge, our study is the first one where a correlation between interaction energies and concentration of dextran or fibrinogen can be done, leading to a more direct comparison with the experiments. At

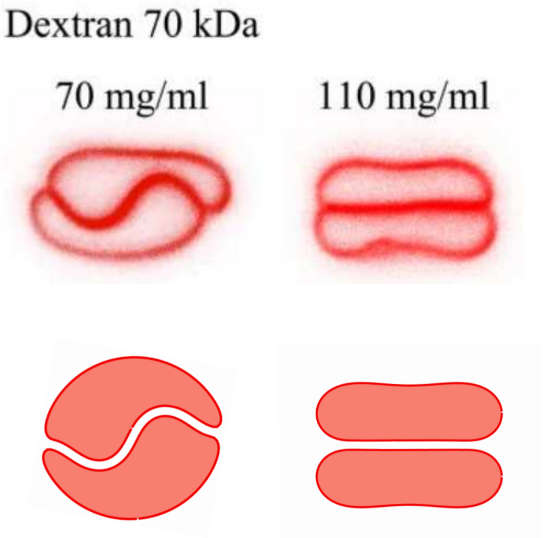

Figure 6.6: Comparison between the experimental shapes (top) and the predicted shapes (bottom) for high (left) and low (right) interaction energies. Note that the cells share the same mechanical properties and size in the theoretical model, which is not always the case in experiments.

low interaction energies, the contact area between the cells is flat (line-type). By increasing progressively the interaction energy, the contact area increases and the cells adopt a sigmoid shape. To characterize this shape transition, a sine function is used to fit the contact zone between the cells. The amplitude of the fitting sine for the case of doublets is plotted as a function of the interaction energy, and then compared to the experimental results[1] obtained as a function of the concentration of Dex70 and then fibrinogen. In order to fit the theoretical and experimental data, the maximum interaction energy is fixed by a direct comparison of the contact areas. The highest amplitude obtained in the theoretical predictions is chosen as the maximum of the bell-shape curve as depicted in Fig.6.7.

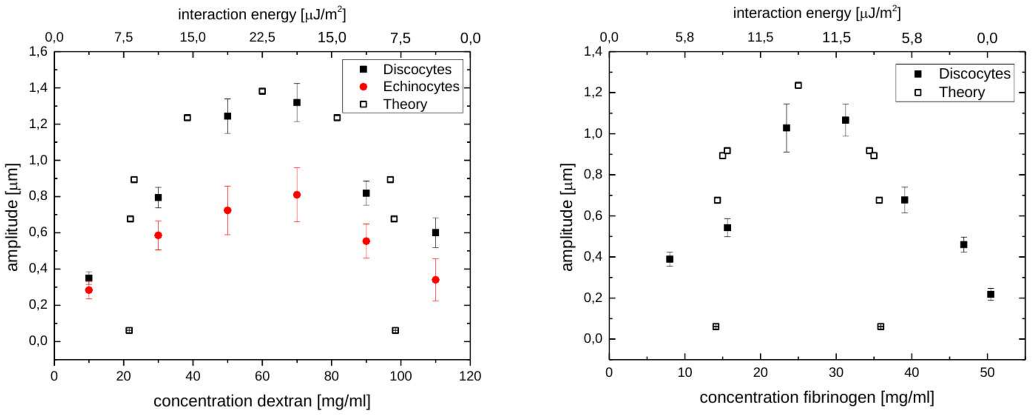

Figure 6.7: Amplitude of the contact zone between two cells as a function of the interaction energy in case of Dex70 (left) and fibrinogen (right). The echinocytes correspond to abnormal shapes (spiky membranes) adopted by healthy RBCs when they touch the cover slip.

---

[1] The experimental work is done by D. Flormann, a PhD student with the group of Prof. Dr. C. Wagner.

6.3.2 Flow of RBCs-like vesicles in microcirculation

We take an initial set of five cells in two channels of widths 4.5 and 12 μm, which are typical values in human capillaries (4.5 μm corresponds to the height of our experimental channels and 12 mm where we found that the clusters persist even though they could experience stronger shear stresses out of the center and pass on top of each other). The velocities explored at the center of the channel are approximately 1 mm/s. The viscosity ratio is set to 5 which corresponds to a cytoplasmic viscosity of ≈ 5 cP, and the reduced area to 0.65. Theses values are chosen close to the one of a typical young human RBC. The cells are initially disposed along a line in the middle of the channel (Fig. 6.8). We progressively increase the interaction energy and analyze the subsequent behavior of the initial configuration. Fig. 6.9 summarizes our findings. In both experiments and numerics, we observe a tendency of having bigger clusters while increasing the interaction energy. In the experimental curves Fig 6.9-left, the increase of the interaction energy leads to a decrease of the single cells and an increase of the clusters. The size of the clusters (number of cells per cluster) increases with the interaction energy. In Fig. 6.10, the interaction energy is increased from top to bottom. At low interaction energies, the cells that are initially arranged in a cluster tend to flow as single cells[2] because the disaggregation forces (combination of electrostatic repulsion, membrane strain, and mechanical shearing due to the flow) are still higher than the

Figure 6.8: Sketch depicting the initial configuration of the cells in channel.

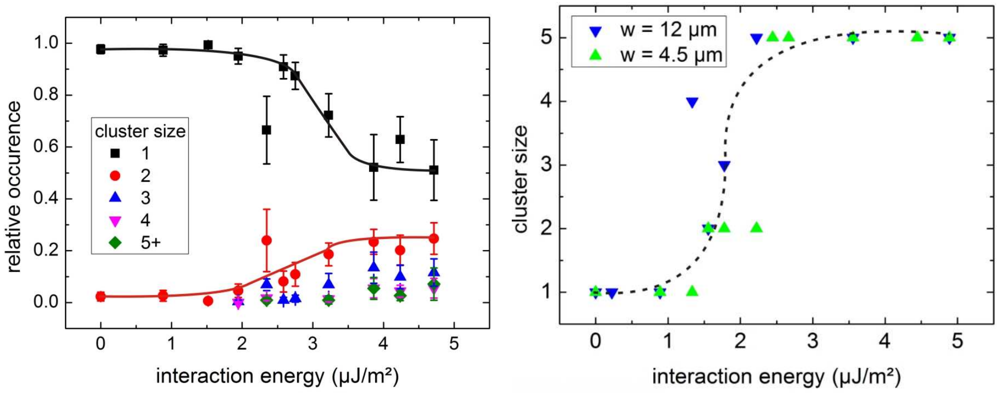

Figure 6.9: Cluster size as a function of the interaction energy. Left: the probability of having a cluster of a given size (relative occurrence) is plotted as a function of the interaction energy (experiments). Right: same as left but in the case of two different channel widths (numerics).

---

[2] as discussed in the previous chapter, though the interdistance is relatively large, the cells are still interacting hydrodynamically

aggregation forces. At normal levels of fibrinogen, clusters of two and three cells start to form and persist in time. Approaching concentrations of fibrinogen within the limit of the physiological range, stable and persistent clusters of 5 cells are formed. Both numerical and experimental works show cluster size transitions at the same interaction energies. It is interesting to mention that the experiments are performed in narrow channels, where the long ranged hydrodynamic interactions effect are minimized (screening), and the cluster formation depends on the cells' entrance in the channels since the aggregation forces are short ranged. But once the cluster is formed mainly due to aggregation forces, it continues flowing as a stable cluster in the channel. At larger channels, it is expected that the long ranged hydrodynamic interactions lead to the formation of clusters. The question is whether there is a difference between hydrodynamic clusters with and without macromolecules.

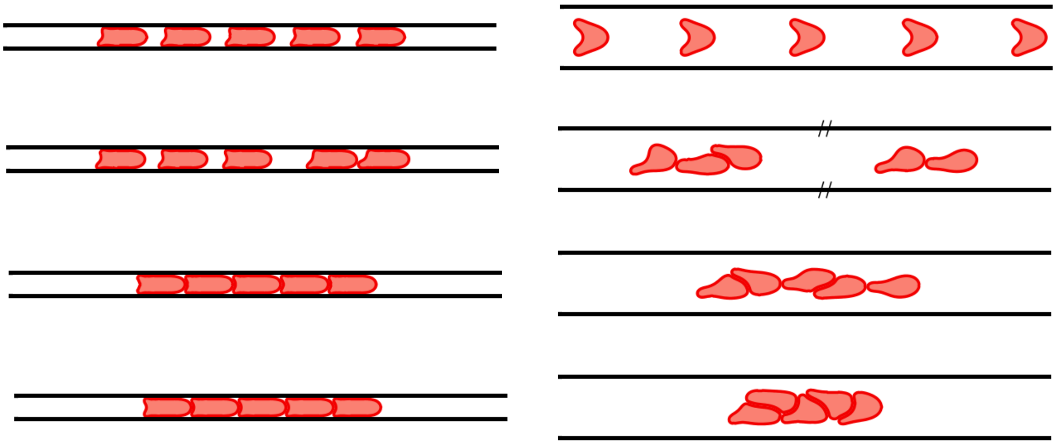

Figure 6.10: Stationary configuration of the cells as a function of the interaction energy. From top to bottom, the interaction energy reads as: 0, 1.78, 3.56, and 4.89 μJ/m^2, corresponding namely to concentrations of fibrinogen:0, 1, 4 (still in the physiological range), and 6.5 mg/mL (level of fibrinogen corresponding to stroke patients [Di Napoli 2001]). The width of the channel is 4.5 μm (left), and 12 μm (right).

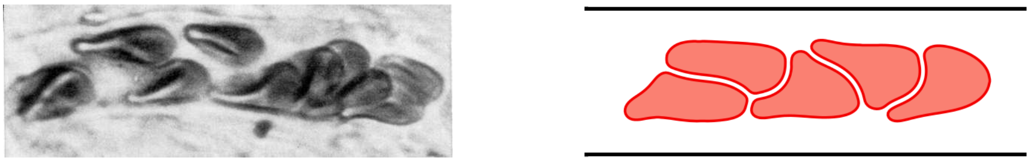

Figure 6.11: RBCs in zigzag arrangement flowing in a capillary of 12 μm diameter in presence of fibrinogen. Left: in vivo human RBCs [Skalak 1969]. Right: in silico RBCs-like vesicles.

Experiments are performed in channels of 12 μm diameters in the presence and absence of Dex70 and then Dex150. The RBCs are driven with an input mid-plane velocity of around 2.12 mm/s. A part of these results related to pure hydrodynamic interactions is discussed in chapter 5. Numerical simulations are performed along with the experiments[3]. We consider a pair of RBCs-like vesicles with a membrane rigidity of 4×10^{-19} J, a cytoplasmic viscosity of 5 cP, a reduced area of 0.65, and a typical radius of 4 μm. The interaction energies used to mimic dextran 70 and 150 are namely ε =4.8 μJ/m^2 and ε =12 μJ/m^2. Our study revealed a significant differences in the morphology and the intercellular distances between the clusters formed with and without macromolecules. To quantify the relation between the interaction energy and the morphology of the clusters, we have measured the interacting contact zone length, by setting a threshold on the distance between nodes from different interfaces corresponding to a distance of $2^{1/6}\sigma$ at which the minimum potential is reached. The results are reported in Figure 6.15.

Figure 6.12: Numerical simulations depicting the stationary shapes of clusters of two cells. (a) cluster formed in absence of macromolecules, (b) in presence of Dex70, and (c) in presence of Dex150.

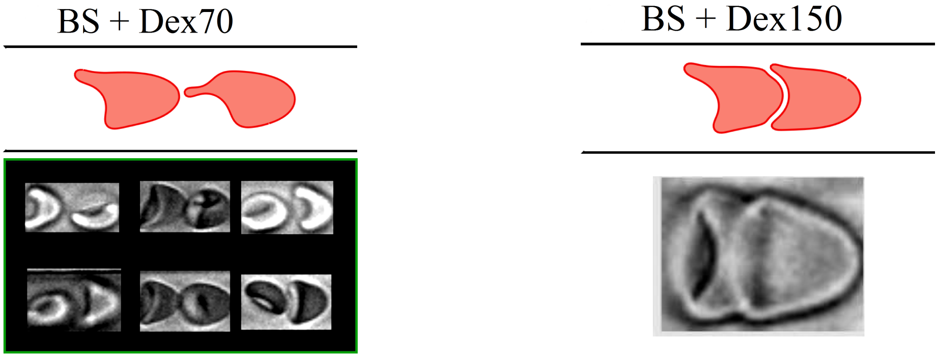

Figure 6.13: Morphology of the clusters formed in the presence of Dex70 (left), and Dex150 (right). Top: numerical simulations. Bottom: in vitro experiments on human RBCs (Courtesy of V. Clavería).

Indeed, in addition to the long ranging hydrodynamic interactions initiating the formation of the cluster, the short ranging adhesion mechanism induced by the interaction between macromolecules and the cells' surface helps to compact the cluster, and hence reducing the intercellular distance. The cells in the clusters formed in presence of macromolecules look almost touching each other. An

---

[3] Experimental work performed by V. Clavería, a PhD student with the group of Prof. Dr. C. Wagner.

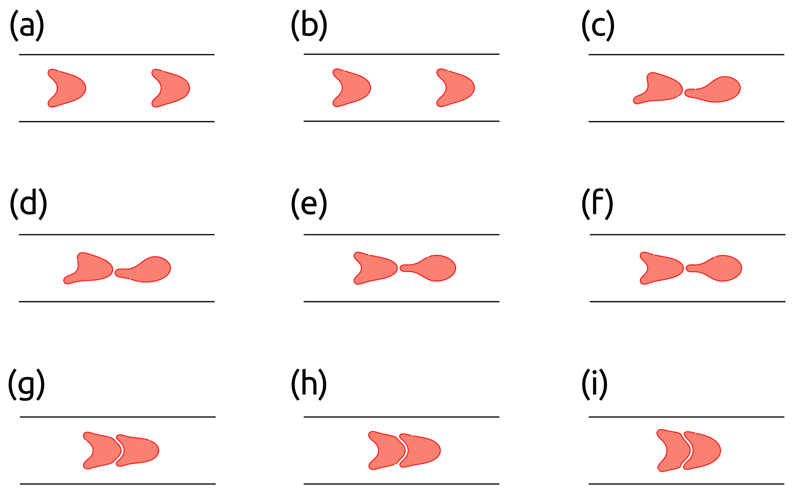

Figure 6.14: Stationary configurations of a pair of cells as a function of the interaction energy (ε). (a)$\varepsilon = 0$; (b) 2.66; (c) = 3.11; (d) = 3.55; (e) = 4.44; (f) = 5.33; (g) = 6.22; (h) = 7.11; and (i) = $14.22 \mu J/m^2$. The parameters used read as $Ca = 10$, $\nu = 0.65$, $\lambda = 1$, and $W = 4R_0$.

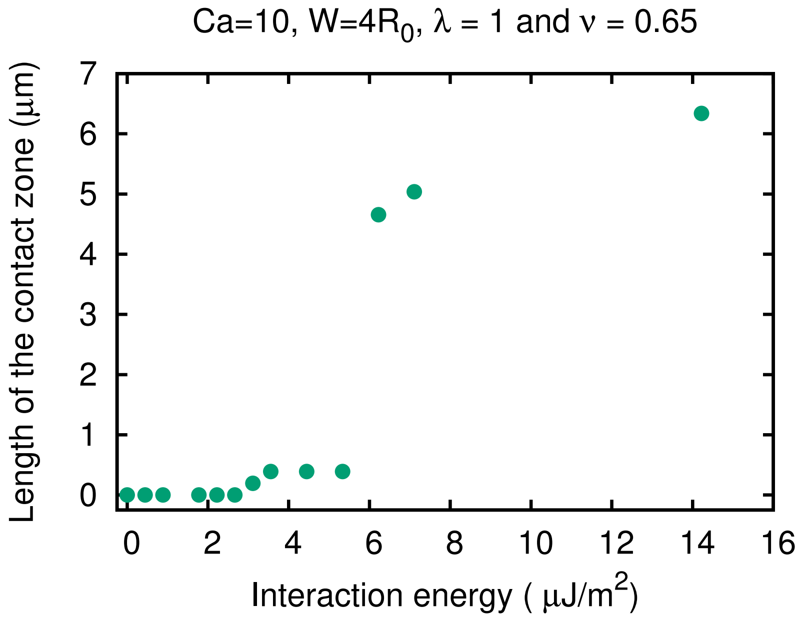

Figure 6.15: Effect of the interaction energy on the length of the contact zone.

increase in the intercellular interaction energy leads to a further decrease of the distance between the cells of the cluster and an increase of the interacting contact zone (See Fig. 6.14 and Fig. 6.15). Our attention was drawn to the sudden sharpe increase of the interacting contact zone length by a factor of 12 observed when the interaction energy went up from 5.33 to 6.22 µJ/m^2, whereas this factor went down to 1.08 for an increase of interaction energy from 6.22 to 7.11 μJ/m^2. This work is still undergoing while we wrote this chapter; more quantitative results are expectable in the near future.

6.4 Conclusions

A toy model combined with experimental studies is introduced for the first time to investigate the mechanism of aggregation in absence and presence of an external flow. Aggregates are formed in the larger vessels (in the macrocirculation) and are destroyed once they enter to the microcirculation where the shear rate is high enough to induce the disaggregation. Unlike in the macrocirculation, the flow profile in the microcirculation is parabolic. In this condition, it is known that the RBCs tend to migrate toward the centerline of the flow, where the shear rate is relatively small. Therefor the effect of the macromolecules should persist in the microcirculation despite the high wall shear rate. Our interest goes first to the formation of aggregates of RBCs (the so-called rouleaux) in a quiescent fluid. The effect of the concentration of macromolecules on the morphology of the aggregates is reported. The concentration of macromolecules is quantified in term of interaction energy [Steffen 2013, Brust 2014] and then plugged directly in the theoretical model to mimic the presence of the macromolecules. The contact area between the cells shows a change from flat contact zone to a pronounced sigmoid while increasing the interaction energy. The theoretical predictions are in a good agreement with the experimental results. The main result is that the morphology of the aggregates can be correlated with a specific interaction energy that corresponds to a given concentration of macromolecules (e.g. fibrinogen), which can be used as a prognosis to detect eventual diseases such as atherosclerosis [Handa 1989, Sabeti 2005]. The second part of this chapter is dedicated to study the contribution of both hydrodynamic and macromolecule induced interactions on the flow of RBCs in the microcirculation. To achieve this, we combine an experimental and a numerical approach to study the effect of macromolecules concentration, via their interaction energies quantified with the help of the single cell force spectroscopy measurements, on the clusters formation. Our findings underline the role of macromolecules in the formation of more stable and persistent clusters in the microcirculation. This should affect not only the local rheology of blood but also the RBC distribution in the microcirculatory network and the related oxygen delivery to tissues through the potential impact of clusters on cell distribution at bifurcations. The mechanism of clustering in presence and absence of macromolecules was investigated in a dilute suspension. The long ranging hydrodynamic interactions –when they are positive –lead to an attraction between neighboring cells and the formation of clusters with clear and visible space between them. In such configurations, the short range adhesion interactions due to the macromolecules can then take place and enhance the formation of more compact and sticky-type clusters.

CHAPTER 7

Conclusions and Perspectives

7.1 Conclusions

In this thesis, we have studied two-dimensional deformable interfaces driven by an external flow in confined geometries. In chapter 3, we have introduced the theoretical background needed to build a boundary integral equation from Stokes equations. We have employed the image technique to derive the Green's function satisfying the proper boundary conditions on the walls. This has provided us with a powerful tool to study realistic problems related to the flow of red blood cells in microcirculation, and compare our predictions with experiments performed in our team. In chapter 4, we have used our model to investigate the dynamical behavior of a single vesicle subject to a parabolic Poiseuille flow. The vesicles are inextensible elastic passive interfaces enclosing an inner fluid and suspended in an outer fluid. They interact with the surrounding fluids only via bending forces that are derived from the free Helfrich curvature energy. The inextensibility of the membrane is constrained locally which ensures a global conservation of the area and the perimeter. In chapter 5, we have extended the boundary formulation for the case of N interfaces and studied the pairing mechanism due to the intricate coupling between hydrodynamic interactions and confinement. In chapter 6, we have introduced a toy model to include the cell-cell interaction forces due to the presence of macromolecules in the outer fluid.
The main findings can be summarized as follows:

- The dynamic of a single vesicle in a confined geometry under a Poiseuille flow has revealed 9 major distinct shapes and dynamics, ranging from symmetric and non-symmetric solutions, up to chaos. In the absence of inertia (in the Stokes regime), it is a classical result that the Poiseuille flow is always laminar. The existence of a single elastic object within the flow, acting only via bending forces, completely destroys the overall picture: chaotic dynamics take place. Transitions from steady shapes to chaos through a cascade of subharmonic oscillations occurred by changing only one parameter. This study was published in [Aouane 2014].

- In the absence of macromolecules, the mechanism of pairing is controlled by the hydrodynamic interactions. The effects of the confinement have been investigated. Stable interparticle distances corresponding to stable fixed points (attractors) toward where the system tend to evolve in the limit of the basin

of attraction have been found. Unstable fixed points as well as a discontinuity have been observed for a given range of channel widths. A change of the nature of the hydrodynamic interactions leading to repulsion (instead of attraction) and therefor to the breakup of the clusters has been observed. An intricate and complex interplay between the confinement, external noises and intrinsic properties of the cells can trigger this phenomena.
Experiments in our group on purely hydrodynamic clusters at fixed flow conditions and confinement have shown a bimodal distribution of the interparticle distance of the clusters. Our numerical model has confirmed the same behavior by changing the membrane bending stiffness, an intrinsic property of the red blood cells, within the physiological range [Claveria 2015].

- The role of the macromolecules on cluster formation has been investigated. The adhesion energy corresponding to a concentration of a specific macromolecule has been quantified by our team, and the values can be plugged directly in our toy model that depends only on one parameter: the intercellular surface energy. The numerical predictions on aggregation of RBCs has shown a good agreement with the experimental data from our team, although it is still an ongoing work [Flormann 2015]. The formation of clusters in presence of plasma protein fibrinogen (or the synthetic sugar polymer dextran) has been investigated in microchannels. The conditions have been set to mimic the flow of red blood cells in microcirculation. The numerical predictions have shown a correlation between the increase of the adhesion energy and the increase of the size (number of cells) of the cluster. These transitions occur at the same level of adhesion energy observed in our experiments. We have pinpointed the role of macromolecules in the formation of more stable clusters that can persist for a long time during the flow in the microcirculation. These findings have a significant impact on the understanding of the rheology of blood, and the distribution of oxygen to tissues through the potential impact of clusters on cell distribution at bifurcations. It is worthy to recall that before this study, the macromolecule effect was neglected in most of the theoretical models since it was commonly accepted that the shear forces are high in the microcirculation. This is an invalid assumption because the RBCs have the tendency to migrate toward the centerline of the flow where the shear forces are low. Our findings were published in [Brust 2014].
  We have investigated the differences between the purely hydrodynamic clusters and the one formed in presence of macromolecules. Our results have shown a significant morphological difference suggesting the existence of two kind of clusters in agreement with the experimental observations. The intricate mechanisms occurring in the presence of macromolecules allow cases where mixed type of clusters can be observed experimentally [Claveria 2015].

7.2 Perspectives

It would be interesting to investigate in the future:

- The behavior of these chaotic regimes in the presence of many vesicles, and in more realistic cases by taking into account the presence of macromolecules.
- A simplified theoretical model explaining the nature reversal of the hydrodynamic interactions as a function of a set of key parameters.
- The effect of confinement on pair formation to the case of many vesicles. It would be rather interesting to observe the effect of the number of cells on the basin of attraction and the reference attractors (the ones predicted for a pair of two cells).
- The effect of adhesion energy on the rheology of blood in shear and Poiseuille flows.
- The critical shear rate needed to break a big aggregates into smaller ones. This can be used in experiments to obtain aggregates with a specific size (number of cells).

CHAPTER 8

Conclusions et Perspectives

8.1 Conclusions

Dans cette thèse, nous avons étudié le mouvement d'intérfaces déformables sous écoulements dans une géométrie confinée. Dans le chapitre 3, nous avons discuté des étapes nécessaire pour construire une formulation intégrale à partir des équations de Stokes. Nous avons utilisé la technique des images pour dériver les fonctions de Green satisfaisant les conditions aux limites sur les parois. Nous avons développé un outil puissant pour étudier des problèmes liés à l'écoulement des globules rouges dans la microcirculation, puis nous avons comparé nos prédictions avec les résultats experimentaux effectués dans notre équipe. Dans le chapitre 4, nous avons utilisé notre modèle pour étudier la dynamique d'une vésicule isolée soumise à un écoulement de Poiseuille. La vésicule est une interface passive élastique et inextensible, qui englobe un fluide interne et est suspendue dans un fluide externe. Elle interagit avec les fluides environnant uniquement via les forces de courbures (qui sont dérivées de l'énergie libre de courbure d'Helfrich). L'inextensibilité de la membrane est contrainte localement ce qui assure une conservation globale de la surface et du périmètre. Dans le chapitre 5, nous avons étendu le modèle au cas de N interfaces et ensuite étudié les mécanismes de formation de clusters dûs au couplage complexe entre les interactions hydrodynamiques et le confinement. Dans le chapitre 6, nous avons introduit un modèle simplifié pour inclure les les forces d'interactions intercellulaires dûes à la présence de macromolécules. Les principaux résultats peuvent être résumé comme suit:

- la dynamique d'une vésicule isolée dans une géométrie confinée soumise à un écoulement de Poiseuille a révélée 9 types de formes et dynamiques distinctes, allant des solutions symétriques et asymétrique, au chaos. En l'absence d'inertie (dans un régime de Stokes), l'écoulement de Poiseuille est connu pour être toujours laminaire. Le couplage d'une interface élastique isolée - interagissant seulement via les forces de courbures - avec l'écoulement, détruit complétement le tableau: une dynamique chaotique occure. La transition des formes stationnaires au chaos à travers une cascade oscillations sous-harmoniques survient en variant seulement un seul paramètre. Cette étude a été publié dans [Aouane 2014].

- En l'absence des macromolécules, le mécanisme de formation de clusters est contrôlé par les interactions hydrodynamiques. Les effets du confinement ont été exploré. Des interdistances stationnaires correspondant à des

points stables fixes (attracteurs) vers lesquelles le système tend à évoluer dans la limite du bassin d'attraction ont été trouvé. De même, des points instables fixes et une discontinuité ont été observé pour un certain intervalle de confinements. Un changement dans la nature des interactions hydrodynamiques menant à une répulsion (au lieu d'une attraction) et donc à la destruction des clusters a été observé. Une relation complexe entre le confinement, les perturbations externes et les propriétés intrinsèque des cellules peuvent induire ce phénomène.
Des expériences faites dans notre groupe sur les clusters hydrodynamiques sous des conditiosn d'écoulement et de confinement constants ont montré une distribution bimodale de l'interdistance des clusters. Le même résultat a été observé numériquement en variant la rigidité de la membrane, une des propriétés intrinsèques des globules rouges, dans les limites physiologiques [Claveria 2015].

- Le rôle des macromolécules dans la formation des clusters a été étudié. L'énergie d'adhésion correspondant à une concentration d'une certaine macromolécule a été quantifié expérimentalement par notre équipe. Les valeurs ainsi obtenues peuvent être directement injecté dans notre modèle qui ne dépend que d'une seule variable: l'énergie intercellulaires. Les prédictions numériques obtenues dans le cas de l'étude des agrégations des globules rouges et la formation de rouleaux concorde assez bien avec les résultats obtenus expérimentalement dans notre équipe [Flormann 2015]. La formation de clusters dans des microcanaux mimant l'écoulement des globules rouges dans la microcirculation en présence de fibrinogène (ou de dextran) a été étudié. Les résultats numériques ont montré une corrélation entre l'augmentation de l'énérgie d'adhésion et l'augmentation de la taille des clusters (nombre de cellules formant le cluster). Ces transitions occurent pour les mêmes niveaux d'énergie d'adhésion observée dans nos expériences. Nous avons montré le rôle des macromolécules dans la formation de clusters plus stable qui peuvent persister longtemps dans la microcirculation. Ces résultats ont un important impact sur la rhéologie du sang, et sur la distribution de l'oxygène dans les tissues à travers l'effect possible des clusters sur la distribution des cellules dans les bifurcations. C'est important de rappeler qu'avant cette étude, l'effet des macromolécules a été négligé dans la plupart des modèles théoriques puisqu'il était communément admis que les forces de cisaillement sont très élevées dans la microcirculation. Ceci est une hypothèse non fondée parce que les globules rouges ont tendance à migrer vers le centre du canal où les forces de cisaillement sont trop faibles. Nos résultats ont été publié dans [Brust 2014].
  Nous avons étudié la différence entre les clusters hydrodynamiques et ceux formés en présence de macromolécules. Nos résultats ont montré une différence morphologique soulignant l'existance de deux types de clusters en concordance avec les résultas expérimentaux. Des cas de clusters mixtes té-

moignant d'un couplage complexe entre les interactions hydrodynamiques et les interactions induites par la macromolécules ont été observé expérimentalement [Claveria 2015].

8.2 Perspectives

Il serait intéressant d'étudier dans le future:

- Le comportement des régimes chaotiques en présence de plusieurs vésicules, et dans un cas plus proche de la réalité en considérant la présence des macromolécules.
- Un simple modèle théorique expliquant le changement de la nature des interactions hydrodynamiques en fonction d'un jeu de paramètres.
- L'effet du confinement sur la formation de clusters dans le cas de plusieurs vésicules. Il serait intéressant de voir l'effet du nombre de cellules sur le basin d'attraction et les points stables fixes (ceux prédit dans le cas d'un cluster de deux cellules).
- L'effet de l'énergie d'adhésion sur la rhéologie du sang dans des écoulements de cisaillement et de Poiseuille.
- Le taux de cisaillement critique pour briser les rouleaux en de plus petits agrégats. Ce résultat peut-être utilisé pour obtenir des agrégats d'une taille spécifique (nombre des cellules).

CHAPTER 9

Zusammenfassung und Ausblick

9.1 Zusammenfassung

In der vorliegenden Arbeit wurden verformbare Grenzflächen untersucht, verursacht durch externe Flüsse in einer eingeschränkten Geometrien. Im Kapitel 3 wurde zur Ableitung der Randintegralgleichungen für den zweidimensionalen Fall aus den Navier-Stokes-Gleichungen der theoretische Hintergrund dargelegt. Zur Ableitung der Greenschen Funktionen mit den geeigneten Randbedingungen an den Grenzflächen wurde die Spiegelbildtechnik benutzt. Dieses leistungsstarke Werkzeug ermöglichte die realistische Untersuchung von Problemstellungen, welche bei der Bewegung von roten Blutzellen in Mikrozikulationen auftreten. Diese Ergebnisse wurden mit experimentellen Daten aus der Arbeitsgruppe verglichen. Im Kapitel 4 wurde das vorgestellte Modell benutzt um das dynamische Verhalten einzelner Vesikel in einem parabolischen Poiseuille-Fluss zu beschreiben. Vesikel sind suspendierte, passive, volumenerhaltende, elastische Grenzflächenobjekte, welche eine innere von einer äußeren Flüssigkeit abgrenzen. Die Wechselwirkung mit der umgebenden Flüssigkeit wird alleinig durch die Biegekraft gekennzeichnet. Diese wird aus der Helfrichschen Krümmungsenergie abgeleitet. Die Nichtausdehnbarkeit der Membrane ist eine lokale Erhaltungsgröße und führt zur globalen Erhaltung der Oberfläche und des Durchmessers. Im Kapitel 5 wurde der Randintegralmechanismus erweitert auf den Fall von N gekoppelte Grenzflächen um die komplizierten hydrodynamischen und durch Randeffekte verursachten Wechselwirkungen zu untersuchen. Im Kapitel 6 wurde ein einfaches Modell zur Beschreibung der Zell-Zell Wechselwirkungskräfte vorgestellt um den Einfluss von vorhandenen Makromolekülen in der äußeren Flüssigkeit zu beschreiben. Die Hauptergebnisse der vorliegenden Arbeit können zusammengefasst werden zu:

- Die Dynamik eines einzelnen Vesikels in einer eingeschränkten Geometrie bei einem Poiseuille-Fluss kann eingeteilt werden in 9 verschiedene Formen und Dynamiken, beginnend bei symmetrischen über unsymmetrischen Lösungen bis hin zum chaotischen Verhalten. Der Poiseulle-Fluss, abgeleitet von der Stokes-Gleichung welche die Trägheitsterme vernachlässigt, ist grundsätzlich laminar. Bei Anwesenheit eines einzelnes elastischen Objektes, welches lediglich über die Biegekräfte wechselwirkt, wird dieses Bild komplett zerstört, sogar ein chaotisches Verhalten kann auftreten. Die Übergänge von stationären hin zum chaotischen Verhalten, über eine Kaskade von mehreren harmonischen periodischen Oszillationen, können durch Änderung eines einzigen Parameters hervorgerufen werden. Diese Ergebnisse wurden in [Aouane 2014] publiziert.

- In Abwesenheit von Makromolekülen beruht der Paarbildungsmechanismus lediglich auf der hydrodynamischen Wechselwirkung. Die Einflüsse von eingeschränkten Geometrien wurden untersucht. Stabile Abstände zwischen den Partikeln korrespondieren mit stabilen Fixpunkten (Attraktoren) in Bereichen wo das System sich hin zu einem Grenzzyklus entwickelt. Für bestimmte Kanalbreiten wurden Instabile Fixpunkte, wie auch Diskontinuitäten gefunden. Es wurden Situationen gefunden wo die hydrodynamische Wechselwirkung zur Abstoßung (anstatt zur Anziehung) führte. Dieses spiegelt das Aufbrechen von Clustern wider und ist das Ergebnisses eines komplizierten und komplexem Wechselspiels zwischen der geometrischen Einschränkung, externen Rauschquellen und den intrinsischen Eigenschaften der Zellen. Experimente in unserer Arbeitsgruppe unter den Bedingungen einer reinen hydrodynamischen Wechselwirkung bei definierten Flusseigenschaften und Geometrien zeigten eine bimodale Verteilung in den Abständen zwischen den Clustern. Das vorgestellte numerische Modell kann dieses Verhalten erklären, siehe [Claveria 2015]. Es basiert auf verschiedenen Zellmembranesteifigkeiten, innerhalb des physiologischen Parameterbereiches. Diese Steifigkeit ist eine intrinsische Eigenschaft von roten Blutzellen.

- Der Einfluss des Vorhandenseins von Makromolekülen auf die Clusterbildung wurde untersucht. Die Anziehungskraft zwischen zwei roten Blutzellen als Funktion der Konzentration der Makromoleküle wurde in unserer Arbeitsgruppe quantifiziert. Dieser Werte wurden im vorgestellten Minimalmodell benutzt, welche nur von einem Parameter abhängig ist, der Oberflächenenergie zwischen den Zellen. Die numerischen Vorhersagen zur Aggregation von roten Blutzellen waren in guter Übereinstimmung mit ersten experimentellen Ergebnissen. Diese Untersuchungen sind weiterhin Gegenstand der aktuellen Forschung [Flormann 2015]. Die experimentellen Untersuchungen zur Clusterbildung in Mikrokanälen sind repräsentativ für den Fluss von roten Blutzellen in Mikrozirkulation beim Vorhandensein des Plasmaproteins Fibrinogen (oder dem synthetischen Zuckerpolymer Dextran). Die numerischen Untersuchungen zeigten eine direkte Korrelation zwischen der angenommenen Anziehungskraft und der Größe der Cluster (Anzahl der Zellen im Cluster). Die Übergänge in der Clustergröße bei verschiedenen Anziehungskräften in den numerischen Simulationen waren in Übereinstimmung mit experimentellen Ergebnissen. Somit konnte die wichtige Rolle des Vorhandenseins von Makromolekülen für die Clusterbildung hin zu stabileren und länger bestehenden Clustern bei der Mikrozirkulation dargelegt werden. Diese Ergebnisse haben einen signifikanten Einfluss in die Interpretation der rheologischen Daten von Blut und die Verteilung des Sauerstoffs im Gewebe aufgrund der Zellverteilung an Abzweigungen. Es soll erwähnt werden, dass vor den stattgefundenen Untersuchungen, der Einfluss der Makromoleküle in theoretischen Modellen größtenteils vernachlässigt wurde, da allgemein angenommen wurde, dass die Scherraten bei der Mikrozirkulation groß sind. Diese Annahme ist falsch, da die roten Blutzellen die Tendenz zeigen sich zur Mittelachse zu bewegen, wo die Scherraten klein sind. Die Ergebnisse wurden in [Brust 2014] publiziert. Es wurden die Unterschiede herausgestellt zwischen den rein hydrodynamischen Clustern und denen welche durch das Vorhandensein von Makromolekülen entstehen. Die Ergebnisse zeigten einen klaren morphologischen Unterschied womit zwei Arten von Clustern definiert werden konnten. Dies ist in Übereinstimmung mit experimentellen Ergebnissen. Die komplizierten Mechanismen beim Vorhandensein von Makromolekülen führen zu gemischten Clusterarten, welche experimentell beobachtet wurden [Claveria 2015].

9.2 Ausblick

In zukünftigen Arbeiten wäre es interessant folgende Punkte zu Untersuchen:

- Die Beschreibung des chaotischen Verhaltens wenn viele Vesikel vorhanden sind und der mehr realistische Fall mit Berücksichtigung der Anwesenheit von Makromolekülen.
- Ein einfaches theoretisches Modell, welches die der Umkehrung der hydrodynamischen Wechselwirkung als Funktion von Schlüsselparametern beschreibt.
- Der Einfluss von eingeschränkten Geometrien auf die Paarbildung im Fall von vielen Vesikel. Es wäre interessant den Einfluss der Zellanzahl auf den Haupattraktor zu untersuchen im Vergleich zum Attraktor hervorgerufen durch Paare von zwei Zellen.
- Der Einfluss der Anziehungskraft zwischen den Grenzflächen auf die Rheologie des Blutes in Scher- und Poiseuille-Flüssen.
- Die Bestimmung der kritischen Scherrate um große Cluster in kleinere aufzuspalten. Diese kann in Experimenten mit spezifizierten Aggregatgrößen (Zellanzahl) Anwendung finden werden.

APPENDIX A

Membrane models

Several constitutive equations can be found in the literature describing different kind of interfaces (*e.g* capsules and vesicles). Some of this models were derived to ultimately depict the mechanical properties of the red blood cell membrane. Different approaches exist in the literature (in addition to teh model introduced in chapter 3), we cite among others the Mooney-Rivlin model which is a generalization of the neo-Hookean law, where the membrane is considered as an isotropic hyperelastic thin sheet of a three-dimensional incompressible material [Pozrikidis 2005a, Liu 2006]. The strain energy function is then expressed as a linear combination of the first and second invariants namely I_1 and I_2 of the left Cauchy-Green deformation tensor (Finger deformation tensor),

$$W_{MR} = C_1(I_1 - 3) + C_2(I_2 - 3) \tag{A.1}$$

where C_1 and C_2 are the material constants and are determined empirically. For a rbc, C_1 =2.57 $\times$ 10^6 dyn/cm^2 and C_2 =0.257 $\times$ 10^6 dyn/cm^2, corresponding to a Young modulus of 10^7 dyn/cm^2 [Liu 2006]. When the deformations of a linear material are very small, $C_2 \mapsto 0$ and the Mooney-Rivlin is reduced to a neo-Hookean model. Modified versions of the Mooney-Rivlin and Neo-Hookean models have been adopted by several authors to emphasize more on a specific aspect of the material behavior or to express the components of the strain energy function in a more "handy" way [Skalak 1973, Barthes-Biesel 1981, Eggleton 1998, Pozrikidis 2003]. A second popular model, the Evans-Skalak model [Evans 1980], proposes a strain energy function build upon deformation measurements for human rbcs, and given by

$$W_{ES} = K_{rbc}(\lambda_1\lambda_2 - 1)^2 + \alpha_{rbc}[\frac{\lambda_1^2 + \lambda_2^2}{2\lambda_1^2\lambda_2^2} - 1] \tag{A.2}$$

where $\lambda_{1,2}$ are the extension ratios expressed in local in-plane curvilinear coordinates. K_{rbc} =500 dyn/cm is the area dilatation modulus, and α_{rbc} =6 $\times$ 10^{-3} dyn/cm is the shear modulus. Several studies pinpointed the role of the bending energy in the equilibrium shape of the rbc [Fung 1965, Canham 1970, Lew 1972] and showed a non-trivial coupling with the membrane tension (shear stresses): shear stresses are induced when the membrane is bend even if the tension is isotropic in each monolayer [Secomb 1988]. Therefor in the absence of terms accounting for the bending moment, a stress-free shape (biconcave shape for a rbc) needs to be define. A parametric equation for the unstressed shape of the rbc was proposed by Evans and Fung 1972 (EF),

$$D(r) = [1 - (r/R_0)^2]^{0.5}[C_0 + C_2(r/R_0)^2 + C_4(R/R_0)^4] \tag{A.3}$$

where R_0 =3.91 µm is the radius of the cell and r is the distance from the axis of symmetry. C_0, C_2 and C_4 are empirical coefficients defined namely as 0.81 µm, 7.83 µm and −4.39 µm [Evans 1972]. To consider the relation between bending stiffness and the externally imposed bending moment on the membrane, a constitutive linear law was proposed in [Pozrikidis 2010], and then coupled to the membrane in-plane tension as following

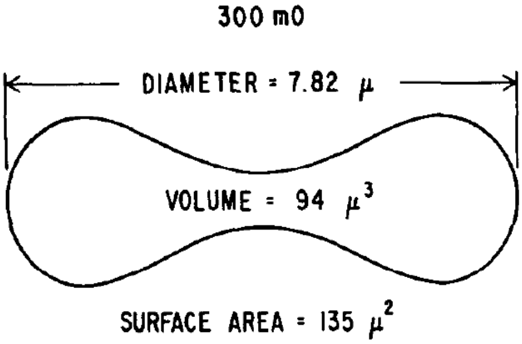

Figure A.1: Unstressed shape of a rbc obtained from the parametric equation of EF. The coefficients plugged in the equation were determined on individual rbcs in a suspension with a tonicity of 300 mO [Evans 1972].

$$\Delta \mathbf{f} = -(E_D \frac{\partial \lambda_s}{\partial l} + E_B \kappa \frac{\partial(\kappa - \kappa_R)}{\partial l})\mathbf{t} + (E_D(\lambda_s - 1)\kappa - E_B \frac{\partial^2(\kappa - \kappa_R)}{\partial l^2})\mathbf{n} \tag{A.4}$$

where E_D and E_B are the elastic and the bending moduli, $\lambda_s \equiv \partial l / \partial l_R$ is the stretch, l_R is the membrane elementary arclength when the membrane is relaxed, and κ and κ_R are the curvature and resting curvature of the membrane.

Bibliography

[Abkarian 2008a] M. Abkarian, M. Faivre, R. Horton, K. Smistrup, C. A Best-Popescu and H. A Stone. *Cellular-scale hydrodynamics*. Biomedical Materials, vol. 3, no. 3, page 034011, 2008.

[Abkarian 2008b] M. Abkarian and A. Viallat. *Vesicles and red blood cells in shear flow*. Soft Matter, vol. 4, pages 653–657, 2008.

[Adams 1973] K.H. Adams. *A theory for the shape of the red blood cell*. Biophysical journal, vol. 13, no. 10, page 1049, 1973.

[Aouane 2014] O. Aouane, M. Thiébaud, A. Benyoussef, C. Wagner and C. Misbah. *Vesicle dynamics in a confined Poiseuille flow: From steady state to chaos*. Phys. Rev. E, vol. 90, page 033011, Sep 2014.

[Aris 1989] R. Aris. Vectors, tensors, and the basic equations of fluid mechanics. Dover Publications, New York, 1989.

[Asakura 1958] S. Asakura and F. Oosawa. *Interaction between particles suspended in solutions of macromolecules*. Journal of Polymer Science, vol. 33, no. 126, pages 183–192, 1958.

[Baghshani 2010] H. Baghshani, S. Nazifi, M. Saeb and S. Saeb. *Influence of road transportation on plasma concentrations of acute phase proteins, including fibrinogen, haptoglobin, serum amyloid A, and ceruloplasmin, in dromedary camels (Camelus dromedarius)*. Comparative clinical pathology, vol. 19, no. 2, pages 193–198, 2010.

[Banerjee 1962] S. Banerjee, R.C. Bhattacharjee and T.I. Singh. *Hematological studies in the normal adult Indian camel (Camelus dromedarius)*. American Journal of Physiology – Legacy Content, vol. 203, no. 6, pages 1185–1187, 1962.

[Barthes-Biesel 1981] D. Barthes-Biesel and J.M. Rallison. *The time-dependent deformation of a capsule freely suspended in a linear shear flow*. Journal of Fluid Mechanics, vol. 113, pages 251–267, 1981.

[Barthès-Biesel 2012] D. Barthès-Biesel. Microhydrodynamics and complex fluids. CRC Press, 2012.

[Baskurt 1996] O.K. Baskurt. *Deformability of red blood cells from different species studied by resistive pulse shape analysis technique*. Biorheology, vol. 33, no. 2, pages 169–179, 1996.

[Baskurt 2007] O.K. Baskurt. Handbook of hemorheology and hemodynamics. Biomedical and health research. IOS Press, 2007.

[Baskurt 2011] O. Baskurt, B. Neu and H.J. Meiselman. Red blood cell aggregation. Taylor & Francis, 2011.

[Batchelor 2000] G.K. Batchelor. An introduction to fluid dynamics. Cambridge Mathematical Library. Cambridge University Press, 2000.

[Beatus 2006] T. Beatus, T. Tlusty and R. Bar-Ziv. *Phonons in a one-dimensional microfluidic crystal*. Nature Physics, vol. 2, no. 11, pages 743–748, 2006.

[Beatus 2007] T. Beatus, R. Bar-Ziv and T. Tlusty. *Anomalous microfluidic phonons induced by the interplay of hydrodynamic screening and incompressibility*. Physical review letters, vol. 99, no. 12, page 124502, 2007.

[Bergé 1992] P. Bergé, Y. Pomeau and C. Vidal. L'ordre dans le chaos. Hermann, 1992.

[Biben 2011] T. Biben, A. Farutin and C. Misbah. *Three-dimensional vesicles under shear flow: Numerical study of dynamics and phase diagram*. Phys. Rev. E, vol. 83, page 031921, Mar 2011.

[Branemark 1963] P.I. Branemark and J. Lindstrom. *Shape of circulating blood corpuscles*. Biorheology, vol. 1, pages 139–142, 1963.

[Brust 2013a] M. Brust. *Rheological properties of Red Blood Cells*. PhD thesis, Universität des Saarlandes (Germany) & Université Joseph Fourier, Grenoble (France), 2013.

[Brust 2013b] M Brust, C Schaefer, R Doerr, L Pan, M Garcia, PE Arratia and C Wagner. *Rheology of human blood plasma: Viscoelastic versus Newtonian behavior*. Physical review letters, vol. 110, no. 7, page 078305, 2013.

[Brust 2014] M. Brust, O. Aouane, M. Thiébaud, D. Flormann, C. Verdier, L. Kaestner, MW Laschke, H. Selmi, A. Benyoussef, T. Podgorski*et al. The plasma protein fibrinogen stabilizes clusters of red blood cells in microcapillary flows*. Scientific reports, vol. 4, 2014.

[Calderon 2010] A.J. Calderon, B. Eshpuniyani, J.B. Fowlkes and J.L. Bull. *A boundary element model of the transport of a semi-infinite bubble through a microvessel bifurcation*. Physics of Fluids (1994-present), vol. 22, no. 6, page 061902, 2010.

[Canham 1968] P.B. Canham and A.C. Burton. *Distribution of size and shape in populations of normal human red cells*. Circulation Research, vol. 22, no. 3, pages 405–422, 1968.

[Canham 1970] P.B. Canham. *The minimum energy of bending as a possible explanation of the biconcave shape of the human red blood cell*. Journal of Theoretical Biology, vol. 26, no. 1, pages 61–81, 1970.

[Cantat 1999a] I. Cantat. *Dynamique de vésicules en adhésion*. PhD thesis, Université Joseph Fourier, Grenoble, 1999.

[Cantat 1999b] I. Cantat and C. Misbah. *Dynamics and similarity laws for adhering vesicles in haptotaxis*. Physical review letters, vol. 83, no. 1, page 235, 1999.

[Cantat 1999c] I. Cantat and C. Misbah. *Lift force and dynamical unbinding of adhering vesicles under shear flow*. Physical review letters, vol. 83, no. 4, page 880, 1999.

[Cantat 2000] I. Cantat, C. Misbah and Y. Saito. *Vesicle propulsion in haptotaxis: A local model*. The European Physical Journal E, vol. 3, no. 4, pages 403–412, 2000.

[Cantat 2003] I. Cantat, K. Kassner and C. Misbah. *Vesicles in haptotaxis with hydrodynamical dissipation*. The European Physical Journal E: Soft Matter and Biological Physics, vol. 10, no. 2, pages 175–189, 2003.

[Chien 1975] S. Chien. *Biophysical Behaviour of Suspensions, in" The Red Blood Cell*. pages 1031–1133. D.M. Surgenor, 1975.

[Chien 1987] S. Chien. *Red cell deformability and its relevance to blood flow*. Annual review of physiology, vol. 49, no. 1, pages 177–192, 1987.

[Claveria 2015] V. Claveria, O. Aouane, M. Thiébaud, M. Abkarian, G. Coupier, C. Misbah, T. John and C. Wagner. *Clusters of red blood cells in microcapillary flow: hydrodynamic versus macromolecule induced interaction*. Submitted, 2015.

[Cokelet 1968] G.R. Cokelet and H.J. Meiselman. *Rheological Comparison of Hemoglobin Solutions and Erythrocyte Suspensions*. Science, vol. 162, no. 3850, pages 275–277, 1968.

[Comeglio 1996] P. Comeglio, S. Fedi, A.A. Liotta, A.P. Cellai, E. Chiarantini, D. Prisco, F. Mecacci, E. Parretti, G. Mello and R. Abbate. *Blood clotting activation during normal pregnancy*. Thrombosis research, vol. 84, no. 3, pages 199–202, 1996.

[Coupier 2008] G. Coupier, B. Kaoui, T. Podgorski and C. Misbah. *Noninertial lateral migration of vesicles in bounded Poiseuille flow*. Physics of Fluids (1994-present), vol. 20, no. 11, page 111702, 2008.

[Csahók 1999] Z. Csahók, C. Misbah and A. Valance. *A class of nonlinear front evolution equations derived from geometry and conservation*. Physica D: Nonlinear Phenomena, vol. 128, no. 1, pages 87–100, 1999.

[Cui 2002] B. Cui, H. Diamant and B. Lin. *Screened Hydrodynamic Interaction in a Narrow Channel*. Phys. Rev. Lett., vol. 89, page 188302, Oct 2002.

[Cui 2004] B. Cui, H. Diamant, B. Lin and S.A. Rice. *Anomalous Hydrodynamic Interaction in a Quasi-Two-Dimensional Suspension*. Phys. Rev. Lett., vol. 92, page 258301, Jun 2004.

[Dao 2003] M. Dao, C.T. Lim and S. Suresh. *Mechanics of the human red blood cell deformed by optical tweezers*. Journal of the Mechanics and Physics of Solids, vol. 51, no. 11-12, pages 2259–2280, 2003. Proceedings of a Symposium on Dynamic Failure and Thin Film Mechanics, honoring Professor L.B. Freund.

[Di Napoli 2001] M. Di Napoli, F. Papa and V. Bocola. *C-reactive protein in ischemic stroke an independent prognostic factor*. Stroke, vol. 32, no. 4, pages 917–924, 2001.

[Diamant 2005] H. Diamant, B. Cui, B. Lin and S.A. Rice. *Hydrodynamic interaction in quasi-two-dimensional suspensions*. Journal of Physics: Condensed Matter, vol. 17, no. 31, page S2787, 2005.

[Eggleton 1998] C.D. Eggleton and A.S. Popel. *Large deformation of red blood cell ghosts in a simple shear flow*. Physics of Fluids (1994-present), vol. 10, no. 8, pages 1834–1845, 1998.

[Ernst 1993] E. Ernst and K.L. Resch. *Fibrinogen as a cardiovascular risk factor: a meta-analysis and review of the literature*. Annals of Internal Medicine, vol. 118, no. 12, pages 956–963, 1993.

[Evans 1972] E. Evans and Y.C. Fung. *Improved measurements of the erythrocyte geometry*. Microvascular research, vol. 4, no. 4, pages 335–347, 1972.

[Evans 1976] E.A. Evans and R.M. Hochmuth. *Membrane viscoelasticity*. Biophysical Journal, vol. 16, no. 1, page 1, 1976.

[Evans 1980] .E Evans, R. Skalak*et al.* *Mechanics and thermodynamics of biomembranes*. 1980.

[Fåhraeus 1929] R. Fåhraeus. *The suspension stability of the blood*. Physiological Reviews, vol. 9, no. 2, pages 241–274, 1929.

[Fåhræus 1931] R. Fåhræus and T. Lindqvist. *The viscosity of the blood in narrow capillary tubes*. American Journal of Physiology–Legacy Content, vol. 96, no. 3, pages 562–568, 1931.

[Farutin 2012] A. Farutin, O. Aouane and C. Misbah. *Vesicle dynamics under weak flows: Application to large excess area*. Physical Review E, vol. 85, no. 6, page 061922, 2012.

[Farutin 2014] A. Farutin and C. Misbah. *Symmetry breaking and cross-streamline migration of three-dimensional vesicles in an axial Poiseuille flow*. Phys. Rev. E, vol. 89, page 042709, Apr 2014.

[Fedosov 2014] D. A. Fedosov, M. Peltomaki and G. Gompper. *Deformation and dynamics of red blood cells in flow through cylindrical microchannels*. Soft Matter, vol. 10, pages 4258–4267, 2014.

[Flormann 2015] D. Flormann, O. Aouane, L. Kaestner, T. Podgorski, S. Svetina, C. Misbah and C. Wagner. *Contact zones of small and large red blood cell clusters from low to high dextran and fibrinogen concentrations*. In preparation, 2015.

[Fung 1965] Y.C. Fung. *Theoretical considerations of the elasticity of red cells and small blood vessels*. In Federation Proceedings, volume 25, pages 1761–1772, 1965.

[Fung 1968] Y.C. Fung and P. Tong. *Theory of the sphering of red blood cells*. Biophysical journal, vol. 8, no. 2, page 175, 1968.

[Ghigliotti 2009] G. Ghigliotti, H. Selmi, B. Kaoui, G. Biros and C. Misbah. *Dynamics and rheology of highly deflated vesicles*. In Esaim: proceedings, volume 28, pages 211–226. EDP Sciences, 2009.

[Ghigliotti 2010a] G. Ghigliotti. *Dynamics and rheology of a suspension of vesicles and red blood cells*. PhD thesis, Université Joseph Fourier, Grenoble, 2010.

[Ghigliotti 2010b] G. Ghigliotti, T. Biben and C. Misbah. *Rheology of a dilute two-dimensional suspension of vesicles*. Journal of Fluid Mechanics, vol. 653, pages 489–518, 2010.

[Ghigliotti 2011] G. Ghigliotti, A. Rahimian, G. Biros and C. Misbah. *Vesicle migration and spatial organization driven by flow line curvature*. Physical review letters, vol. 106, no. 2, page 028101, 2011.

[Ghigliotti 2012] G. Ghigliotti, H. Selmi, L. El Asmi and C. Misbah. *Why and how does collective red blood cells motion occur in the blood microcirculation?* Physics of Fluids (1994-present), vol. 24, no. 10, page 101901, 2012.

[Goldsmith 1989] H.L. Goldsmith, G.R. Cokelet and P. Gaehtgens. *Robin Fahraeus: evolution of his concepts in cardiovascular physiology*. American Journal of Physiology-Heart and Circulatory Physiology, vol. 257, no. 3, pages H1005–H1015, 1989.

[Goldsmith 1999] H.L. Goldsmith, D.N. Bell, S. Spain and F.A. McIntosh. *Effect of red blood cells and their aggregates on platelets and white cells in flowing blood*. Biorheology, vol. 36, no. 5, pages 461–468, 1999.

[Groisman 2000] A. Groisman and V. Steinberg. *Elastic turbulence in a polymer solution flow*. Nature, vol. 405, no. 6782, pages 53–55, 2000.

[Guido 2009] S. Guido and G. Tomaiuolo. *Microconfined flow behavior of red blood cells in vitro*. Comptes Rendus Physique, vol. 10, no. 8, pages 751–763, 2009.

[Handa 1989] K. Handa, S. Kono, K. Saku, J. Sasaki, T. Kawano, Y. Sasaki, T. Hiroki and K. Arakawa. *Plasma fibrinogen levels as an independent indicator of severity of coronary atherosclerosis*. Atherosclerosis, vol. 77, no. 2, pages 209–213, 1989.

[Hazewinkel 1990] M. Hazewinkel. Encyclopaedia of mathematics. Numeéro vol. 6 de Encyclopaedia of Mathematics. Springer Netherlands, 1990.

[Helfrich 1973] W. Helfrich. *Elastic Properties of Lipid Bilayers: Theory and Possible Experiments*. Z. Naturforsch., vol. 28c, pages 693–703, 1973.

[Homan 1988] R. Homan and H.J. Pownall. *Transbilayer diffusion of phospholipids: dependence on headgroup structure and acyl chain length*. Biochimica et Biophysica Acta (BBA)-Biomembranes, vol. 938, no. 2, pages 155–166, 1988.

[Janssen 2012] P.J.A. Janssen, M.D. Baron, P.D. Anderson, J. Blawzdziewicz, M. Loewenberg and E. Wajnryb. *Collective dynamics of confined rigid spheres and deformable drops*. Soft Matter, vol. 8, no. 28, pages 7495–7506, 2012.

[Jeon 1992] K.W. Jeon and M. Friedlander. International review of cytology. Numeéro vol. 130. Elsevier Science, 1992.

[Ju 2013] Meongkeun Ju, Swe Soe Ye, Hong Tong Low, Junfeng Zhang, Pedro Cabrales, Hwa Liang Leo and Sangho Kim. *Effect of deformability difference between two erythrocytes on their aggregation*. Physical biology, vol. 10, no. 3, page 036001, 2013.

[Kaestner 2012] L. Kaestner, P. Steffen, D.B. Nguyen, J. Wang, L. Wagner-Britz, A. Jung, C. Wagner and I. Bernhardt. *Lysophosphatidic acid induced red blood cell aggregation in vitro*. Bioelectrochemistry, vol. 87, pages 89–95, 2012.

[Kannel 1990] W.B. Kannel, R.B. D'Agostino, P.W.F. Wilson, A.J. Belanger and D.R. Gagnon. *Diabetes, fibrinogen, and risk of cardiovascular disease: the Framingham experience*. American heart journal, vol. 120, no. 3, pages 672–676, 1990.

[Kaoui 2008] B. Kaoui, G.H. Ristow, I. Cantat, C. Misbah and W. Zimmermann. *Lateral migration of a two-dimensional vesicle in unbounded Poiseuille flow*. Physical Review E, vol. 77, no. 2, page 021903, 2008.

[Kaoui 2009a] B. Kaoui. *Modelling vesicle dynamics in extended geometries and in microfluidic devices*. PhD thesis, Université Joseph Fourier, Grenoble & Université Hassan II, Casablanca (Morocco), 2009.

[Kaoui 2009b] B. Kaoui, G. Biros and C. Misbah. *Why do red blood cells have asymmetric shapes even in a symmetric flow?* Physical review letters, vol. 103, no. 18, page 188101, 2009.

[Kaoui 2009c] B. Kaoui, A. Farutin and C. Misbah. *Vesicles under simple shear flow: Elucidating the role of relevant control parameters*. Physical Review E, vol. 80, no. 6, page 061905, 2009.

[Kaoui 2011a] B. Kaoui, J. Harting and C. Misbah. *Two-dimensional vesicle dynamics under shear flow: Effect of confinement*. Physical Review E, vol. 83, no. 6, page 066319, 2011.

[Kaoui 2011b] B. Kaoui, N. Tahiri, T. Biben, H. Ez-Zahraouy, A. Benyoussef, G. Biros and C. Misbah. *Complexity of vesicle microcirculation*. Physical Review E, vol. 84, no. 4, page 041906, 2011.

[Khodadad 1983] J.K. Khodadad and R.S. Weinstein. *The band 3-rich membrane of llama erythrocytes: studies on cell shape and the organization of membrane proteins*. The Journal of membrane biology, vol. 72, no. 3, pages 161–171, 1983.

[Kim 2013] S. Kim and S.J. Karrila. Microhydrodynamics: Principles and selected applications. Dover Civil and Mechanical Engineering. Dover Publications, 2013.

[Klitzman 1979] B. Klitzman and B.R. Duling. *Microvascular hematocrit and red cell flow in resting and contracting striated muscle*. American Journal of Physiology-Heart and Circulatory Physiology, vol. 237, no. 4, pages H481–H490, 1979.

[Ladyzhenskaya 1969] O.A. Ladyzhenskaya and R.A. Silverman. The mathematical theory of viscous incompressible flow, volume 76. Gordon and Breach New York, 1969.

[Lamb 1945] H. Lamb. Hydrodynamics. Dover Books on Physics. Dover Publications, 1945.

[Lanotte 2013] L. Lanotte. *Deformation and aggregation of red blood cells and vesicles flowing in microchannels*. PhD thesis, Università degli Studi Federico II di Napoli & Université Joseph Fourier, Grenoble (France), 2013.

[Lanotte 2014] Luca Lanotte, Giovanna Tomaiuolo, Chaouqi Misbah, Lionel Bureau and Stefano Guido. *Red blood cell dynamics in polymer brush-coated microcapillaries: A model of endothelial glycocalyx in vitro*. Biomicrofluidics, vol. 8, no. 1, page 014104, 2014.

[Lee 1993] A.J. Lee, G.D. Lowe, M. Woodward and H. Tunstall-Pedoe. *Fibrinogen in relation to personal history of prevalent hypertension, diabetes, stroke, intermittent claudication, coronary heart disease, and family history: the Scottish Heart Health Study.* British Heart Journal, vol. 69, no. 4, pages 338–342, 1993.

[Leichtberg 1976] S. Leichtberg, R. Pfeffer and S. Weinbaum. *Stokes flow past finite coaxial clusters of spheres in a circular cylinder*. International Journal of Multiphase Flow, vol. 3, no. 2, pages 147–169, 1976.

[Lew 1972] Hyok Sang Lew. *Electro-tension and torque in biological membranes modeled as a dipole sheet in fluid conductors*. Journal of Biomechanics, vol. 5, no. 4, pages 399 – 408, 1972.

[Li 1975] T.-Y. Li and J.A. Yorke. *Period three implies chaos*. American mathematical monthly, pages 985–992, 1975.

[Linderkamp 1982] O. Linderkamp and H. J. Meiselman. *Geometric, osmotic, and membrane mechanical properties of density- separated human red cells*. Blood, vol. 59, no. 6, pages 1121–1127, 1982.

[Lipowsky 1980] H.H. Lipowsky, S. Usami and S. Chien. *In vivo measurements of apparent viscosity and microvessel hematocrit in the mesentery of the cat*. Microvascular research, vol. 19, no. 3, pages 297–319, 1980.

[Lipowsky 1995] R. Lipowsky and E. Sackmann. Structure and dynamics of membranes: I. from cells to vesicles/ii. generic and specific interactions. Elsevier, 1995.

[Liron 1976] N. Liron and S. Mochon. *Stokes flow for a stokeslet between two parallel flat plates*. Journal of Engineering Mathematics, vol. 10, no. 4, pages 287–303, 1976.

[Liu 2006] Y. Liu and W.K. Liu. *Rheology of red blood cell aggregation by computer simulation*. Journal of Computational Physics, vol. 220, no. 1, pages 139–154, 2006.

[Lui 2013] S.H. Lui. *On Period-tripling and Quadrupling Bifurcations*. Journal of Modern Mathematics Frontier, vol. 2, no. 2, pages 74–77, 2013.

[Mader 2001] S. Mader. Human biology. McGraw-Hill Education, 2001.

[Madl 1993] C Madl, R Koppensteiner, B Wendelin, K Lenz, L Kramer, G Grimm, A Kranz, B Schneeweiss and H Ehringer. *Effect of immunoglobulin administration on blood rheology in patients with septic shock.* Circulatory shock, vol. 40, no. 4, pages 264–267, 1993.

[Maeda 1985] N. Maeda and T. Shiga. *Inhibition and acceleration of erythrocyte aggregation induced by small macromolecules*. Biochimica et Biophysica Acta (BBA) - General Subjects, vol. 843, no. 1-2, pages 128 – 136, 1985.

[Maeda 1986a] N. Maeda, M. Sekiya, K. Kameda and T. Shiga. *Effect of immunoglobulin preparations on the aggregation of human erythrocytes*. European Journal of Clinical Investigation, vol. 16, no. 2, pages 184–191, 1986.

[Maeda 1986b] N. Maeda and T. Shiga. *Opposite effect of albumin on the erythrocyte aggregation induced by immunoglobulin G and fibrinogen*. Biochimica et Biophysica Acta (BBA)-Biomembranes, vol. 855, no. 1, pages 127–135, 1986.

[McWhirter 2011] J.L. McWhirter, H. Noguchi and G. Gompper. *Deformation and clustering of red blood cells in microcapillary flows*. Soft Matter, vol. 7, no. 22, pages 10967–10977, 2011.

[Mohandas 2008] N. Mohandas and P. G. Gallagher. *Red cell membrane: past, present, and future*. Blood, vol. 112, no. 10, pages 3939–3948, 2008.

[Morrison 2001] F.A. Morrison. Understanding rheology. Topics chemical engineering : A series of textbooks and monographs. Oxford University Press, 2001.

[Nash 1993] G.B. Nash and S. Egginton. *Comparative rheology of human and trout red blood cells*. The Journal of Experimental Biology, vol. 174, no. 1, pages 109–22, 1993.

[Neu 2002] B. Neu and H.J. Meiselman. *Depletion-mediated red blood cell aggregation in polymer solutions*. Biophysical journal, vol. 83, no. 5, pages 2482–2490, 2002.

[Nguyen 2011] D.B. Nguyen, L. Wagner-Britz, S. Maia, P. Steffen, C. Wagner, L. Kaestner and I. Bernhardt. *Regulation of phosphatidylserine exposure in red blood cells*. Cellular Physiology and Biochemistry, vol. 28, no. 5, pages 847–856, 2011.

[Olbricht 1987] W.L. Olbricht and D.M. Kung. *The interaction and coalescence of liquid drops in flow through a capillary tube*. Journal of Colloid and Interface Science, vol. 120, no. 1, pages 229 – 244, 1987.

[Ott 2002] E. Ott. Chaos in dynamical systems. Cambridge university press, 2002.

[Popel 2005] A.S. Popel and P.C. Johnson. *Microcirculation and hemorheology*. Annual review of fluid mechanics, vol. 37, page 43, 2005.

[Pozrikidis 1992] C. Pozrikidis. Boundary integral and singularity methods for linearized viscous flow. Cambridge Texts in Applied Mathematics. Cambridge University Press, 1992.

[Pozrikidis 2002] C. Pozrikidis. A practical guide to boundary element methods with the software library bemlib. Taylor & Francis, 2002.

[Pozrikidis 2003] C. Pozrikidis. *Numerical Simulation of the Flow-Induced Deformation of Red Blood Cells*. Annals of Biomedical Engineering, vol. 31, no. 10, pages 1194–1205, 2003.

[Pozrikidis 2005a] C. Pozrikidis. *Axisymmetric motion of a file of red blood cells through capillaries*. Physics of Fluids (1994-present), vol. 17, no. 3, page 031503, 2005.

[Pozrikidis 2005b] C. Pozrikidis. *Numerical simulation of cell motion in tube flow*. Ann. Biomed. Eng., vol. 33, pages 165–178, 2005.

[Pozrikidis 2010] C. Pozrikidis. Computational hydrodynamics of capsules and biological cells. CRC Press, 2010.

[Reynafarje 1975] C. Reynafarje, J. Faura, D. Villavicencio, A. Curaca, B. Reynafarje, L. Oyola, L. Contreras, E. Vallenas and A. Faura. *Oxygen transport of hemoglobin in high-altitude animals (Camelidae)*. Journal of Applied Physiology, vol. 38, no. 5, pages 806–810, 1975.

[Sabeti 2005] S. Sabeti, M. Exner, W. Mlekusch, J. Amighi, P. Quehenberger, H. Rumpold, G. Maurer, E. Minar, O. Wagner and M. Schillinger. *Prognostic impact of fibrinogen in carotid atherosclerosis nonspecific indicator of inflammation or independent predictor of disease progression?* Stroke, vol. 36, no. 7, pages 1400–1404, 2005.

[Schmid-Schönbein 1981] H. Schmid-Schönbein and P. Gaehtgens. *What is red cell deformability?* Scandinavian Journal of Clinical & Laboratory Investigation, vol. 41, no. S156, pages 13–26, 1981.

[Schroeder 2012] M.R. Schroeder. Fractals, chaos, power laws: Minutes from an infinite paradise. Dover Publications, Incorporated, 2012.

[Secomb 1982] T.W. Secomb and R. Skalak. *A two-dimensional model for capillary flow of an asymmetric cell*. Microvascular Research, vol. 24, no. 2, pages 194 – 203, 1982.

[Secomb 1988] T.W. Secomb. *Interaction between bending and tension forces in bilayer membranes*. Biophysical journal, vol. 54, no. 4, page 743, 1988.

[Selmi 2011] H. Selmi, L. Elasmi, G. Ghigliotti and C. Misbah. *Boundary integral and fast multipole method for two dimensional vesicle sets in poiseuille flow*. Discrete and Continuous Dynamical Systems-Series B (DCDS-B), vol. 15, no. 4, pages 1065–1076, 2011.

[Shani 2014] I. Shani, T. Beatus, R. H Bar-Ziv and T. Tlusty. *Long-range orientational order in two-dimensional microfluidic dipoles*. Nature Physics, vol. 10, no. 2, pages 140–144, 2014.

[Skalak 1969] R. Skalak and P. I. Branemark. *Deformation of Red Blood Cells in Capillaries*. Science, vol. 164, no. 3880, pages 717–719, 1969.

[Skalak 1973] R. Skalak, A. Tozeren, R.P. Zarda and S. Chien. *Strain energy function of red blood cell membranes*. Biophysical Journal, vol. 13, no. 3, pages 245–264, 1973.

[Smith 1979] J.E. Smith, N. Mohandas and S.B. Shohet. *Variability in erythrocyte deformability among various mammals*. American Journal of Physiology - Heart and Circulatory Physiology, vol. 236, no. 5, pages H725–H730, 1979.

[Steffen 2011] P. Steffen, A. Jung, D.B. Nguyen, T. Müller, I. Bernhardt, L. Kaestner and C. Wagner. *Stimulation of human red blood cells leads to Ca 2+-mediated intercellular adhesion*. Cell calcium, vol. 50, no. 1, pages 54–61, 2011.

[Steffen 2012] P. Steffen. *Quantification of Red Blood Cell Adhesion using Holographic Optical Tweezers and Single Cell Force Spectroscopy*. PhD thesis, Universität des Saarlandes (Germany), 2012.

[Steffen 2013] P. Steffen, C. Verdier and C. Wagner. *Quantification of depletion-induced adhesion of red blood cells*. Physical review letters, vol. 110, no. 1, page 018102, 2013.

[Surgenor 1974] D.M.N. Surgenor. The red blood cell. Numeéro Bd. 1. Elsevier Science, 1974.

[Surgenor 1975] D.M.N. Surgenor. The red blood cell. Numeéro Bd. 2. Elsevier Science, 1975.

[Svetina 2008] S. Svetina and P. Ziherl. *Morphology of small aggregates of red blood cells*. Bioelectrochemistry, vol. 73, pages 84–91, 2008.

[Tahiri 2013a] N. Tahiri. *Simulation de Globules Rouges modèles, et analyse analytique de modèles de suspensions très concentrées*. PhD thesis, Université Joseph Fourier, Grenoble (France) & Université Mohammed V-agdal, Rabat (Morocco), 2013.

[Tahiri 2013b] N. Tahiri, T. Biben, H. Ez-Zahraouy, A. Benyoussef and C. Misbah. *On the problem of slipper shapes of red blood cells in the microvasculature*. Microvascular research, vol. 85, pages 40–45, 2013.

[Thiébaud 2013] M. Thiébaud and C. Misbah. *Rheology of a vesicle suspension with finite concentration: A numerical study*. Phys. Rev. E, vol. 88, page 062707, Dec 2013.

[Thiébaud 2014] Marine Thiébaud, Zaiyi Shen, Jens Harting and Chaouqi Misbah. *Prediction of anomalous blood viscosity in confined shear flow*. Physical review letters, vol. 112, no. 23, page 238304, 2014.

[Tomaiuolo 2009] G. Tomaiuolo, M. Simeone, V. Martinelli, B. Rotoli and S. Guido. *Red blood cell deformation in microconfined flow*. Soft Matter, vol. 5, pages 3736–3740, 2009.

[Tomaiuolo 2012] G. Tomaiuolo, L. Lanotte, G. Ghigliotti, C. Misbah and S. Guido. *Red blood cell clustering in Poiseuille microcapillary flow*. Physics of Fluids (1994-present), vol. 24, no. 5, page 051903, 2012.

[Vlahovska 2009] P. M. Vlahovska, T. Podgorski and C. Misbah. *Vesicles and red blood cells: from individual dynamics to rheology*. C.R. Physique, vol. 10, no. 1, page 775, 2009.

[Vlahovska 2013] P.M. Vlahovska, D. Barthes-Biesel and C. Misbah. *Flow dynamics of red blood cells and their biomimetic counterparts*. Comptes Rendus Physique, vol. 14, no. 6, pages 451 – 458, 2013. Living fluids / Fluides vivants.

[Wang 1969] H. Wang and R. Skalak. *Viscous flow in a cylindrical tube containing a line of spherical particles*. Journal of Fluid Mechanics, vol. 38, pages 75–96, 8 1969.

[Waugh 1976] R. Waugh and E.A. Evans. *Viscoelastic properties of erythrocyte membranes of different vertebrate animals*. Microvascular research, vol. 12, no. 3, pages 291–304, 1976.

[Welles 1997] E.G. Welles, D.G. Pugh, J.G.W. Wenzel, B. Waldridge and R. Hanson. *Liver biopsy in llamas*. Equine Practice, vol. 19, pages 24–29, 1997.

[Windberger 2003] U. Windberger, A. Bartholovitsch, R. Plasenzotti, K.J. Korak and G. Heinze. *Whole Blood Viscosity, Plasma Viscosity and Erythrocyte Aggregation in Nine Mammalian Species: Reference Values and Comparison of Data*. Experimental Physiology, vol. 88, no. 3, pages 431–440, 2003.

[Yagil 1974] R. Yagil, U.A. Sod-Moriah and N. Meyerstein. *Dehydration and camel blood. II. Shape, size, and concentration of red blood cells*. American Journal of Physiology – Legacy Content, vol. 226, no. 2, pages 301–304, 1974.

[Ze-Hui 2006] J. Ze-Hui, W. Yun-Ying and W. Jing. *Subharmonic motion of granular particles under vertical vibrations*. EPL (Europhysics Letters), vol. 74, no. 3, page 417, 2006.

[Zhang 2008] J. Zhang, P.C. Johnson and A.S. Popel. *Red blood cell aggregation and dissociation in shear flows simulated by lattice Boltzmann method*. Journal of Biomechanics, vol. 41, pages 47–55, 2008.

[Zhao 2010] H. Zhao, A.H.G. Isfahani, Luke N. Olson and Jonathan B. Freund. *A spectral boundary integral method for flowing blood cells*. Journal of Computational Physics, vol. 229, no. 10, pages 3726 – 3744, 2010.

[Zhusubaliyev 2003] Z.T. Zhusubaliyev and E. Mosekilde. Bifurcations and chaos in piecewise-smooth dynamical systems. World Scientific series on nonlinear science: Monographs and treatises. World Scientific, 2003.